

Programmable Dirac masses in hybrid moiré–1D superlattices

Hanzhou Tan¹ and Pilkyung Moon^{1,2,3*}

¹Arts and Sciences, NYU Shanghai, Shanghai, 200124, China.

²NYU-ECNU Institute of Physics at NYU Shanghai, Shanghai, 200062, China.

³Department of Physics, Hanyang University, Seoul, 04763, Korea.

*Corresponding author(s). E-mail(s): pilkyung.moon@nyu.edu;

Abstract

Twisted moiré Dirac systems enable powerful miniband engineering but are largely fixed once the twist angle is set, whereas unidirectional (1D) electrostatic superlattices offer continuous control of Dirac anisotropy; yet robust single-particle gaps at charge neutrality are generally difficult to obtain in either setting. Here we show that combining the two into a hybrid moiré–1D superlattice provides a gate-defined configuration space that hosts both gap-opening resonances and strongly anisotropic gapless regimes. Using full-wave continuum miniband calculations for twisted bilayer graphene, we map the charge-neutrality-point (CNP) gap versus the 1D wavevector \mathbf{G}_{1D} and identify a Dirac–Dirac resonance condition. At resonance, a single-particle CNP gap emerges from a parity–chirality selection rule for the resonant inter-cone coupling, which can be electrically reprogrammed by layer-asymmetric modulation that switches the relative chirality and the active mass channel. The insulating phase persists within a finite near-resonant window, providing quantitative fabrication tolerances, while off-resonant settings remain gapless but enable strong suppression of the transverse Dirac velocity and continuous anisotropic band renormalization. Hybrid moiré–1D superlattices thus provide a practical route to programmable Dirac minibands and electrically selectable mass channels in coupled Dirac systems.

Keywords: hybrid moiré–1D superlattice, Dirac mass engineering, coupled Dirac cones, chirality switching

Twisted moiré Dirac systems have established a powerful framework for band engineering, including the emergence of flat bands and correlated phenomena near the magic angle^[1–4]. Their low-energy reconstruction is, however, largely fixed once the twist angle is set, motivating an external knob for post-fabrication control. By contrast, unidirectional (one-dimensional) electrostatic superlattices provide a gate-defined handle on Dirac anisotropy: in monolayer graphene, a scalar 1D modulation can continuously renormalize Dirac velocities and generate strongly anisotropic dispersions^[5–7]. Nevertheless, without additional symmetry breaking, a robust single-particle gap at the charge-neutrality point (CNP) is generally impossible to obtain in either pristine moiré Dirac minibands^[8–10] or scalar 1D superlattices^[5,6]. Even when two Dirac cones in a moiré superlattice hybridize without momentum mismatch (for example in strongly coupled double-walled nanotubes), the spectrum can remain gapless because the dominant interlayer coupling lacks a σ_z mass channel.^[11]

Here we combine these two ingredients into a hybrid moiré–1D superlattice (Fig. 1a), and show that moiré–1D defines a configuration space in which resonant settings can open a CNP gap, whereas off-resonant settings enable anisotropic Dirac-band engineering within the same twist-angle system (Fig. 1b). The key mechanism is that the unidirectional modulation dresses the Dirac eigenstates and thereby reshapes the inter-Dirac-cone interaction, reshuffling its Pauli-channel content so that a gap-opening mass component can be activated at resonance. When applied asymmetrically to the two layers, this dressing also provides electrical control over the relative chirality of the resonant cones, allowing the CNP gap to be switched on and off and reassigning which resonances become gapped.

Moiré Dirac platforms provide a particularly natural setting for this mechanism, as they host hybridized Dirac cones with a fixed momentum mismatch and well-defined inter-cone couplings, while the 1D gate offers an independent and continuously tunable control knob. At the same time, the state-dressing viewpoint is not specific to moiré and the same idea applies broadly to coupled Dirac systems: whenever two two-component Dirac cones are hybridized, a unidirectional scalar modulation can reshape the effective coupling matrices and tune the relative chirality, thereby selecting whether a gap-opening mass channel is activated. Hybrid Dirac systems that combine a fixed Dirac-cone mismatch with an independently patternable 1D modulation therefore offer a general route to programmable Dirac masses and tunable Dirac anisotropy.

Using twisted bilayer graphene (TBG) as a representative platform, we perform full-wave continuum miniband calculations and map a two-dimensional configuration-space phase diagram controlled by the gate wavevector \mathbf{G}_{1D} . We uncover three regimes: (i) a resonance-enabled CNP gap governed by a parity–chirality selection rule—set by the even/odd resonant harmonic order and the same/opposite Dirac cone chirality—, (ii) a near-resonant gapped regime that quantifies finite tolerance around resonance, and (iii) a distinct off-resonant regime in which the Dirac spectrum remains gapless but becomes strongly and continuously anisotropic, enabling gate-controlled one-directional band renormalization.

A gate-defined moiré–1D design space

We consider TBG at twist angle θ subject to a layer-dependent unidirectional scalar potential $V_l(\mathbf{r}) = (|v_l|/2) \cos(\mathbf{G}_{1D} \cdot \mathbf{r} + \phi_l)$ ($l = 1, 2$) (Fig. 1a). In the layer–sublattice basis $(\psi_{1A}, \psi_{1B}, \psi_{2A}, \psi_{2B})^T$, the single-valley ($\xi = \pm 1$) Hamiltonian reads

$$H_\xi(\mathbf{r}) = \begin{pmatrix} h_\xi^{(1)}(-i\nabla) & T_\xi^\dagger(\mathbf{r}) \\ T_\xi(\mathbf{r}) & h_\xi^{(2)}(-i\nabla) \end{pmatrix} + \begin{pmatrix} V_1(\mathbf{r})\mathbb{I} & 0 \\ 0 & V_2(\mathbf{r})\mathbb{I} \end{pmatrix}. \quad (1)$$

The first block-matrix term is the standard TBG moiré continuum Hamiltonian, comprising the intralayer Dirac blocks $h_\xi^{(l)}(-i\nabla)$ and the moiré interlayer tunnelling $T_\xi(\mathbf{r})$ [1,2,12,13]; the second term adds the layer-dependent 1D scalar potential in block-diagonal form. Unless stated otherwise, the main text focuses on a layer-symmetric modulation, $|v_1| \approx |v_2|$ and $\phi_1 \approx \phi_2$, which is both natural for single-sided electrostatic patterning and favorable for maximizing the intended resonant gap.

We characterize the moiré and 1D strengths by the dimensionless parameters $u_0 = t_0/(\hbar v_F k_\theta)$ and $u_l = |v_l|e^{i\phi_l}/(\hbar v_F G_{1D})$, where t_0 is the moiré tunnelling scale, v_F is the graphene Dirac velocity, $k_\theta = |\Delta\mathbf{K}_\xi(\theta)|$ is the Dirac-point mismatch magnitude, and $G_{1D} = |\mathbf{G}_{1D}|$. We compute minibands using a full-wave plane-wave expansion of Eq. (1) with lattice-relaxed tunnelling parameters [14]; details of the theoretical models are given in Methods and Supplementary Notes S1 and S2.

For a fixed twist angle θ , varying the direction and magnitude of \mathbf{G}_{1D} defines a natural configuration space. The key geometric quantity controlling the low-energy physics is the relation between the Dirac-point mismatch $\Delta\mathbf{K}_\xi(\theta) = \mathbf{K}_\xi^{(1)} - \mathbf{K}_\xi^{(2)}$ and the gate wavevector \mathbf{G}_{1D} . A central outcome of this work is that this relation organizes the CNP spectrum into distinct regimes that can be read off from a configuration-space map.

Configuration-space phase diagram at charge neutrality

Figure 1b shows the direct gap at CNP extracted from full-wave calculations as a function of \mathbf{G}_{1D} at $\theta = 2^\circ$ for a layer-symmetric (in-phase) modulation ($|u_1| = |u_2| = 0.6$ and $\phi_1 = \phi_2 = 0$), and Fig. S8 shows a similar plot for $\theta = 3^\circ$ and 5° . These maps immediately reveal three regimes.

First, pronounced gapped regions appear in the vicinity of discrete Dirac–Dirac resonance points (see also the DOS in Fig. 1c), where an integer multiple of the 1D modulation bridges the moiré Dirac-point mismatch,

$$\Delta\mathbf{K}_\xi(\theta) = \xi n_{1D} \mathbf{G}_{1D}, \quad n_{1D} \in \mathbb{Z}. \quad (2)$$

In real space, Eq. (2) corresponds to a commensurate alignment between the period vector of the 1D modulation \mathbf{L}_{1D} and the moiré superlattice vector \mathbf{L}_1^M , $\mathbf{L}_{1D} = -3n_{1D}\mathbf{L}_1^M/2$ (see Figs. 1a, S1, and Supplementary Note S1).

As shown in Fig. 1b for a layer-symmetric (in-phase) modulation, the resonant response exhibits a clear odd/even selectivity: a robust gap appears for odd n_{1D} ($= 1, 3$) whereas the even resonance $n_{1D} = 2$ remains effectively gapless. Figure 2—the band structures (left) and DOS (right) calculated by a full-wave continuum model—clearly illustrates this odd/even selectivity. As we show below, however, the even resonances are not forbidden in general: they become gapped once a layer-asymmetric modulation switches the relative chirality and thereby selects a different gap-opening channel.

Figure S1c and Table S1 show $L_{1D} \equiv |\mathbf{L}_{1D}|$ as a function of θ : The leading odd resonance $n_{1D} = 1$ maximizes the gap-opening channel but requires the shortest modulation period L_{1D} (for example, $L_{1D}^{(1)} \approx 21.1, 10.6, 7.05$ nm at $\theta = 1, 2, 3^\circ$, respectively), whereas targeting higher odd resonances relaxes the period (e.g., $L_{1D} \approx 63.4, 31.7, 21.1$ nm when $n_{1D} = 3$ at $\theta = 1, 2, 3^\circ$, respectively) at the price of a higher-harmonic suppression of the effective mass channel (Supplementary Notes S4.8 and S8).

Second, the gapped region is not confined to the measure-zero resonance point: it extends into a finite near-resonant domain that appears as a thick arc in configuration space (Fig. 1b). A convenient geometric descriptor of the near-resonant arc is its ridge (centre line), which forms an off-centred circle in the \mathbf{G}_{1D} plane (overlay in Fig. 1b). This ridge reflects the fact that the near-resonant criterion is controlled not only by the resonance condition but also by the competition between momentum mismatch and the magnitude of the emergent gap-opening-channel; a minimal detuned two-cone theory reproduces the arc morphology and its finite width (Supplementary Notes S5 and S8).

Third, away from this near-resonant arc, the spectrum remains gapless at CNP but can become strongly anisotropic, defining an off-resonant regime in which the 1D modulation continuously reshapes the Dirac velocities (see also Fig. 1d). These two outcomes—gap opening versus anisotropic Dirac engineering—arise from distinct mechanisms, as we now demonstrate.

Parity–chirality selection rule for resonant gap opening and chirality switching

The resonance condition Eq. (2) defines a family of candidate hybridizations indexed by n_{1D} . A central finding of the full-wave spectra in Figs. 1b and 2 is that resonant hybridization is highly selective: in the same twist-angle device, the $n_{1D} = 1, 3$ resonant configurations open a robust CNP gap whereas the $n_{1D} = 2$ remains gapless.

At Dirac–Dirac resonance, Eq. (2) fixes the geometry of the hybridization, but a CNP gap opens only if the resonant inter-cone coupling contains the appropriate mass (gap-opening) channel. In moiré–1D, this required mass channel is selected by the parity of the resonant harmonic order n_{1D} together with the relative chirality χ_{rel} of the two cones. Crucially, χ_{rel} can itself be switched by a layer-asymmetric modulation that inverts the sign of one dressed transverse velocity, thereby reassigning the gap-opening Pauli channel. We define the relative chirality χ_{rel} and list the parity–chirality

rule for gap-opening,

$$\chi_{\text{rel}} \equiv \xi_1 \xi_2 \text{sgn}(v_{\perp}^{(1)} v_{\perp}^{(2)}), \quad \text{CNP gap} \iff \begin{cases} n_{1\text{D}} \text{ odd}, & \chi_{\text{rel}} = +1, \\ n_{1\text{D}} \text{ even}, & \chi_{\text{rel}} = -1. \end{cases} \quad (3)$$

schematically shown in Fig. 3a. Here $\xi_{1,2}$ label the valleys of the two cones involved in the resonance, where $\xi_1 = \xi_2 = \xi$ in the valley-conserving resonances relevant for our main configurations. $v_{\perp}^{(l)} = v_{\text{F}}(J_0(|u_l|) - 3u_0^2)/(1 + 6u_0^2)$ denotes the Dirac velocity perpendicular to $\mathbf{G}_{1\text{D}}$, renormalized by both the moiré coupling^[1,2] and the unidirectional modulation^[5-7], where J_n is the Bessel function of the first kind (see Supplementary Note S4.5). As Fig. S2 shows, $v_{\perp}^{(l)}$ changes sign as $|u_l|$ increases.

Default class: $\chi_{\text{rel}} = +1$ and gap opens when $n_{1\text{D}}$ is odd

In the generic case where the unidirectional potentials on the two layers are similar or not strong enough to invert the sign of either transverse velocity (so that $v_{\perp}^{(1)}$ and $v_{\perp}^{(2)}$ remain of the same sign), the dominant resonant pair lies in the same-chirality class $\chi_{\text{rel}} = +1$. The systems in Figs. 1b and 2 all belong to a $\chi_{\text{rel}} = +1$ class, thus only odd $n_{1\text{D}}$ can open a gap.

Chirality switching and gap-opening-channel control.

By contrast, a strongly layer-asymmetric modulation can invert the sign of one transverse velocity (i.e., $v_{\perp}^{(1)} v_{\perp}^{(2)} < 0$), realizing $\chi_{\text{rel}} = -1$ and switching the resonant gap opening from odd to even $n_{1\text{D}}$. Figure 3b shows the band structures near the CNP of the TBG-1D with even ($n_{1\text{D}} = 2$) resonant configuration: In the weak- $|u_1|$ case (left) the transverse velocities retain the same sign ($v_{\perp}^{(1)} v_{\perp}^{(2)} > 0$), corresponding to $\chi_{\text{rel}} = +1$ and a gapless spectrum, whereas in the strong- $|u_1|$ case the velocity inversion $v_{\perp}^{(1)} v_{\perp}^{(2)} < 0$ realizes $\chi_{\text{rel}} = -1$ and opens a CNP gap at the even resonance. This demonstrates that the relative chirality class, and hence the gap-opening Pauli channel, is an electrically programmable knob in the coupled-Dirac regime. In TBG-1D at $\theta = 1^\circ$ ($\theta = 2^\circ$) with $n_{1\text{D}} = 2$, we find that χ_{rel} reverses sign at $v_1 \approx 0.05$ eV ($v_1 \approx 0.39$ eV) (see Fig. S4), where the latter is moderately larger than, yet comparable to, modulation amplitudes inferred in existing gate-defined graphene 1D superlattices (~ 0.26 eV^[7]).

Note that for an isolated, non-interacting Dirac cone, the sign of $v_{\perp}^{(l)}$ is not physical, as it can be flipped by a constant sublattice rotation. In a coupled-Dirac system, however, the sign of $v_{\perp}^{(l)}$ becomes meaningful: a rotation applied to only one cone also transforms the intercone coupling, thereby reshuffling the Pauli components of the interaction matrix (see Supplementary Note S4.5).

Microscopic origin: parity of dressed tunnelling harmonics.

Equation (3) is not merely a classification: it reflects a concrete microscopic mechanism. In moiré-1D, the 1D modulation dresses the moiré interlayer tunnelling, i.e., the modulation is absorbed into the tunnelling by a layer-dependent unitary transformation, yielding an effective tunnelling with modified Pauli structure. Unlike rigid-lattice

TBG where the rank-one structure of T_j^ξ obstructs a full gap at Dirac–Dirac resonance, moiré–1D dressing generically produces a full-rank resonant harmonic and thus opens a route to a Dirac gap (Supplementary Note S4.6).

The n_{1D} -th harmonic of this dressed tunnelling then plays a dual role: it supplies the momentum transfer needed to bring two Dirac cones into resonance, and its Pauli-channel content is fixed by the parity of the harmonic order n_{1D} . In particular, odd harmonics generate the mass channel needed for the same-chirality class ($\chi_{\text{rel}} = +1, \sigma_z$), whereas even harmonics generate the mass channel needed for the opposite-chirality class ($\chi_{\text{rel}} = -1, \sigma_x$). Thus, for a given χ_{rel} , the parity of the resonant harmonic order n_{1D} determines whether the resonance opens a CNP gap or remains effectively gapless. The analytical derivation of the parity structure and its dependence on chirality is provided in Supplementary Notes S3 and S4.

Figure 3c shows a decomposition of the effective resonant inter-cone coupling into its Pauli components, revealing that the gap-opening mass-channel amplitude is selectively generated according to the parity of n_{1D} : The gap-opening channel for $\chi_{\text{rel}} = +1, \sigma_z$, is substantial only in TBG–1D with an odd n_{1D} , while that for $\chi_{\text{rel}} = -1, \sigma_x$, is sizable only in TBG–1D with an even n_{1D} . This establishes the resonant gap as a single-particle hybridization effect controlled by a symmetry-organized channel selection, rather than by fine-tuned symmetry breaking at the lattice scale.

The resonant gap size (for either chirality class $\chi_{\text{rel}} = \pm 1$) is controlled by the layer-symmetric component of the 1D modulation, $u_+ \equiv u_1 + u_2$ with $u_l \equiv |u_l|e^{i\phi_l}$, as the magnitude of the gap-opening channel scales as $|t_0 J_{|n_{1D}|}(|u_+|)|$. Consequently, in-phase modulation ($\phi_1 \approx \phi_2$) maximizes the gap, whereas opposite-phase modulation suppresses it (Fig. S6), and higher-order resonances are rapidly weakened unless $|u_+|$ is extremely large (Fig. S5), consistent with the small $n_{1D} = 3$ gap in Figs. 1b and 2 (Supplementary Notes S4.7 and S4.8). In a layer-symmetric 1D modulation, the node-shifting channels (σ_0 and σ_y) are much smaller than the gap-opening channel.

Although our analytical derivation in Supplementary Notes S3 and S4 is presented in a rigid-lattice form for transparency, the central parity–chirality mechanism is expected to be insensitive to lattice relaxation in the standard sense that it only renormalizes the existing tunnelling amplitudes u_{AA} and u_{AB} without introducing new Pauli-channel structures. Consistent with this expectation, the full-wave mini-band calculations reported here incorporate lattice relaxation through the widely used two-parameter tunnelling model with $u_{AA} \neq u_{AB}$ ^[14], and the observed odd/even resonance selectivity persists (Figs. 1b, 2, 3b).

Near-resonant gapped arcs and fabrication tolerances

The resonance condition Eq. (2) is a measure-zero constraint in the two-dimensional \mathbf{G}_{1D} design space. In realistic devices, \mathbf{G}_{1D} will typically approach but not exactly satisfy it. A key practical outcome of Fig. 1b is therefore the existence of a finite near-resonant gapped neighborhood; a robust CNP gap persists as long as the residual momentum mismatch remains smaller than the emergent hybridization (mass) scale. Because the arc width is controlled by the same emergent mass scale selected in the resonant channel analysis above, the knobs that tune the gap-opening channel and

its magnitude (the layer-symmetric component u_+) directly translate into a tolerance window in configuration space. A minimal detuned two-cone model (Supplementary Note S5) makes this intuition quantitative and explains both the arc morphology and its finite width: for example, the exact-resonant point $\mathbf{G}_{1D} = \Delta\mathbf{K}_\xi(\theta)/\xi$ (for $n_{1D} = 1$) lies on the circle of near-resonance but is not its center, explaining why the gapped region in a fixed- $\Delta\mathbf{K}_\xi$ map is generically off-centered (Fig. S7).

The near-resonant arc also provides a direct route for translating spectral robustness into fabrication tolerances. For a mass channel of 10 meV, we estimate that the gap remains open for twist-angle detunings $|\delta\theta| \lesssim 0.10^\circ$, modulation-period errors $|\delta L_{1D}/L_{1D}| \lesssim 4.9\%$, and axis misalignments $|\delta\varphi_{1D}| \lesssim 2.8^\circ$ in TBG-1D at $\theta = 2^\circ$; the corresponding tolerances at $\theta = 3^\circ$ are $|\delta\theta| \lesssim 0.069^\circ$, $|\delta L_{1D}/L_{1D}| \lesssim 2.3\%$, and $|\delta\varphi_{1D}| \lesssim 1.3^\circ$ (see Supplementary Notes S8.2 and S8.4 for details and feasibility considerations). We do not quote a single set of tolerances at $\theta = 1^\circ$, where the velocity renormalization becomes sufficiently strong that a simple analytic baseline is not quantitatively reliable for defining a sharp tolerance window; qualitatively, however, the reduced velocity is expected to relax the geometric tolerances.

Berry curvature and Chern number.

In the scalar moiré-1D setting considered here, all charge-neutrality gaps obtained in our parameter scans are Chern-trivial: for each gapped configuration we find $C_\xi = 0$ for the occupied minibands in each valley (Supplementary Note S6). This outcome is symmetry guided: Fixing the moiré origin at an AA region, a cosine-type modulation registered about this origin ($V_l(\mathbf{r}) = V_l(-\mathbf{r})$, equivalently $v_l \in \mathbb{R}$) preserves the antiunitary symmetry $C_{2z}T$ in the single-valley continuum model. Because $C_{2z}T$ leaves the reduced-Brillouin-zone momentum invariant, it forces the Berry curvature of each miniband to vanish pointwise and therefore guarantees $C_\xi = 0$ ^[8,9,15]. Shifting the registry phases ϕ_l away from the cosine point breaks $C_{2z}T$ and can generate finite Berry curvature; however, as long as the charge-neutrality gap remains open, the Chern number cannot change from the $C_{2z}T$ -symmetric limit and remains zero.

Off-resonant anisotropic Dirac engineering

Away from the near-resonant arc, the 1D modulation cannot bridge the moiré Dirac mismatch at low energy. Consequently, the CNP remains gapless, but the low-energy Dirac sector is strongly reshaped by Bragg scattering of the unidirectional potential. Figure 4a shows that, near the charge-neutrality Dirac point, the dispersion becomes increasingly anisotropic as the modulation strength is increased, with the velocity perpendicular to the modulation strongly suppressed while the longitudinal velocity can remain comparatively large. The suppression of the velocity happens in the Dirac-point neighborhood, within a momentum window on the scale $|\mathbf{q}| \lesssim \mathcal{O}(G_{1D})$ before stronger miniband mixing becomes important. This off-resonant regime provides a clean route to directional Dirac-cone engineering because it is decoupled from the resonant mass-opening channel and does not rely on commensurability with $\Delta\mathbf{K}_\xi$. Such a low-energy reshaping of the Dirac cone should manifest as strong transport anisotropy and collimation^[16,17], providing an experimentally accessible signature even without

opening a mass gap. Notably, the same modulation-induced transverse-velocity renormalization that underlies this off-resonant anisotropic Dirac engineering is also what enables chirality switching in the coupled-resonant regime when one dressed cone is tuned through $v_{\perp}^{(l)} = 0$ (Fig. 3b).

A compact analytical design formula captures this behavior; controlled downfolding yields an effective anisotropic Dirac Hamiltonian with renormalized velocities

$$v_{\perp}^* = \left(\frac{1 - 3u_0^2 - |u_l|^2/8}{1 + 6u_0^2 + |u_l|^2/8} \right) v_F, \quad v_{\parallel}^* = \left(\frac{1 - 3u_0^2 + |u_l|^2/8}{1 + 6u_0^2 + |u_l|^2/8} \right) v_F \quad (4)$$

(see Supplementary Note S7). Compared to the renormalized Dirac velocity of pristine TBG, $v_{\text{TBG}}^* = v_F(1 - 3u_0^2)/(1 + 6u_0^2)$, Eq. (4) makes explicit that the 1D modulation provides an additional gate-tunable renormalization of the Dirac velocities. Increasing $|u_l|$ strongly suppresses the transverse velocity v_{\perp}^* —which can be driven to zero along a “magic line” in the $(\theta, |u_l|)$ plane, enabling controllable one-directional Dirac flattening in the low-energy sector. Figure 4b visualizes the renormalized transverse velocity and highlights the band flattening line extracted from Eq. (4).

Outlook

Hybrid moiré–1D superlattices provide a gate-defined configuration space that unifies two complementary routes to Dirac miniband control within a single platform: resonance-enabled CNP gap opening and off-resonant anisotropic Dirac engineering. In particular, the near-resonant gapped arc promotes a measure-zero resonance condition into a finite design window that can be translated into experimentally meaningful tolerances, while the off-resonant regime offers a robust route to unidirectional Dirac-cone reshaping that is not tied to exact commensurability. Moreover, a potential-modulation-induced sign reversal of the Dirac velocity in a coupled-Dirac system offers an additional chirality-control knob, thereby reassigning which intercone coupling channel serves as the gap-opening mass.

While we focused here on a long-wavelength scalar 1D potential and valley-conserving miniband reconstruction, the moiré–1D design principle is not limited to this setting: Sublattice-selective modulations or vector-type perturbations, e.g., provided by another moiré interaction with layers surrounding the target moiré superlattice, could access a richer set of inter-cone Pauli channels and enable new response functions beyond the scalar case, including nontrivial Chern bands^[18,19]. Moreover, extending the gate pattern toward shorter length scales or sharper harmonic content may activate intervalley processes, opening a route to engineer inter-valley transitions and chirality selection beyond the valley-decoupled regime considered in this work.

Finally, the moiré–1D setting studied here provides a concrete realization of a general strategy for coupled Dirac systems: a unidirectional modulation dresses the Dirac eigenstates, reshaping the effective coupling matrices and enabling electrical control of the relative chirality, thereby selecting the gap-opening mass channel (Supplementary Notes S3–S5). Hybrid Dirac platforms that combine a fixed Dirac-cone mismatch with an independently patternable 1D modulation should therefore provide a broadly applicable route to programmable Dirac masses and tunable Dirac anisotropy.

Methods

Continuum model. We model twisted bilayer graphene using a valley-resolved moiré continuum Hamiltonian with intralayer Dirac blocks and first-star interlayer tunnelling, as summarized in Eq. (1) and detailed in Supplementary Notes S1–S2. For numerical calculations we use the two-parameter first-star tunnelling model with amplitudes u_{AA} and u_{AB} obtained by lattice relaxation. Spin degeneracy is included as a factor of two. We neglect intervalley scattering assuming that the applied electrostatic modulation is smooth on the graphene lattice scale.

Layer-dependent 1D scalar potential. A layer-dependent one-dimensional scalar potential is applied as $V_l(\mathbf{r}) = (|v_l|/2)\cos(\mathbf{G}_{1D} \cdot \mathbf{r} + \phi_l)$ with $\mathbf{G}_{1D} = G_{1D}(\cos\varphi_{1D}, \sin\varphi_{1D})$ in the laboratory frame ($l = 1, 2$). The configuration space is scanned by varying G_{1D} and φ_{1D} at a fixed twist angle θ .

Plane-wave basis and truncation. For each seed momentum \mathbf{k}_0 we generate the coupled momentum set $\mathbf{k} = \mathbf{k}_0 + \mathbf{G}$ with $\mathbf{G} = m_1\mathbf{G}_1^M + m_2\mathbf{G}_2^M + m_3\mathbf{G}_{1D}$, $m_{1,2,3} \in \mathbb{Z}$, and construct the Hamiltonian matrix in the sublattice-layer basis. We retain basis states satisfying the energy cutoff $\hbar v_F|\mathbf{q}| \leq E_{\max}$, where convergence was verified by increasing E_{\max} until the reported spectra and gap diagnostics are stable.

Periodic geometries: rBZ sampling and direct-gap diagnostics. For globally periodic (rank-2) configurations we sample the reduced Brillouin zone using a uniform mesh. At each crystal momentum \mathbf{q} we obtain the lowest conduction and highest valence energies in each valley, $E_{c,\xi}(\mathbf{q})$ and $E_{v,\xi}(\mathbf{q})$, and compute the direct-gap function $g_\xi(\mathbf{q}) = E_{c,\xi}(\mathbf{q}) - E_{v,\xi}(\mathbf{q})$. The direct gap is defined as $\Delta_{\text{dir}} = \min_{\xi=\pm 1} \min_{\mathbf{q} \in \text{rBZ}} g_\xi(\mathbf{q})$.

Quasiperiodic geometries: unfolded spectral function and DOS diagnostics. For rank-3 configurations without an exact reduced Brillouin zone, we compute the unfolded spectral function $A_l(\mathbf{k}_0, \varepsilon)$ and the normalized density of states as defined in Supplementary Note S2. Seed momenta are sampled within a reference window \mathcal{W} —the smallest polygon formed by \mathbf{G} —and convergence was checked by enlarging \mathcal{W} to the next smallest polygons.

Effective model for resonant/near-resonant configurations. We derive a 4×4 effective Hamiltonian for resonant and near-resonant configurations to elucidate the parity–chirality selection rule, using a layer-dependent unitary transformation that dresses both the intralayer Dirac terms and the interlayer tunnelling (Supplementary Notes S3–S5).

Effective model for off-resonant configurations. We derive an effective Hamiltonian for off-resonant configurations by applying Löwdin partitioning, which yields the velocity-renormalization formula in Eq. (4) (Supplementary Note S7).

Parameter scans and tolerance estimates. Configuration-space maps and tolerance windows are obtained by scanning (G_{1D}, φ_{1D}) at fixed θ and extracting the gapped region based on Δ_{dir} (periodic cases) or spectral/DOS depletion (quasiperiodic cases), following Supplementary Notes S2 and S8.

Acknowledgements

This work was supported by the Brain Pool Program through the National Research Foundation of Korea (NRF) funded by the Ministry of Science and ICT (MSIT) (Grant No. RS-2025-25446099), and by the NYU-ECNU Institute of Physics at NYU Shanghai. This work was conducted at Hanyang University and NYU Shanghai. This research was carried out on the High Performance Computing resources at NYU Shanghai. P.M. used ChatGPT (OpenAI) for proofreading and language editing to improve readability. The scientific content, analysis and conclusions are solely those of the authors.

References

- [1] Santos, J.M.B., Peres, N.M.R., Castro Neto, A.H.: Graphene bilayer with a twist: Electronic structure. *Phys. Rev. Lett.* **99**, 256802 (2007)
- [2] Bistritzer, R., MacDonald, A.H.: Moiré bands in twisted double-layer graphene. *Proc. Natl Acad. Sci. USA* **108**, 12233–12237 (2011)
- [3] Cao, Y., Fatemi, V., Demir, A., Fang, S., Tomarken, S.L., Luo, J.Y., Sanchez-Yamagishi, J.D., Watanabe, K., Taniguchi, T., Kaxiras, E., Ashoori, R.C., Jarillo-Herrero, P.: Correlated insulator behaviour at half-filling in magic-angle graphene superlattices. *Nature* **556**, 80–84 (2018)
- [4] Cao, Y., Fatemi, V., Fang, S., Watanabe, K., Taniguchi, T., Kaxiras, E., Jarillo-Herrero, P.: Unconventional superconductivity in magic-angle graphene superlattices. *Nature* **556**, 43–50 (2018)
- [5] Park, C.-H., Yang, L., Son, Y.-W., Cohen, M.L., Louie, S.G.: Anisotropic behaviours of massless dirac fermions in graphene under periodic potentials. *Nat. Phys.* **4**, 213–217 (2008)
- [6] Brey, L., Fertig, H.A.: Emerging zero modes for graphene in a periodic potential. *Phys. Rev. Lett.* **103**, 046809 (2009)
- [7] Li, Y., Dietrich, S., Forsythe, C., Taniguchi, T., Watanabe, K., Moon, P., Dean, C.R.: Anisotropic band flattening in graphene with one-dimensional superlattices. *Nat. Nanotechnol.* **16**, 525–530 (2021)
- [8] Po, H.C., Zou, L., Vishwanath, A., Senthil, T.: Origin of mott insulating behavior and superconductivity in twisted bilayer graphene. *Phys. Rev. X* **8**(3), 031089 (2018)
- [9] Zou, L., Po, H.C., Vishwanath, A., Senthil, T.: Band structure of twisted bilayer graphene: Emergent symmetries, commensurate approximants, and wannier obstructions. *Phys. Rev. B* **98**, 085435 (2018)

- [10] Song, Z., Wang, Z., Shi, W., Li, G., Fang, C., Bernevig, B.A.: All magic angles in twisted bilayer graphene are topological. *Phys. Rev. Lett.* **123**, 036401 (2019)
- [11] Koshino, M., Moon, P., Son, Y.-W.: Incommensurate double-walled carbon nanotubes as one-dimensional moiré crystals. *Phys. Rev. B* **91**, 035405 (2015)
- [12] Moon, P., Koshino, M.: Optical absorption in twisted bilayer graphene. *Phys. Rev. B* **87**, 205404 (2013)
- [13] Koshino, M.: Interlayer interaction in general incommensurate atomic layers. *New J. Phys.* **87**, 205404 (2013)
- [14] Nam, N.N.T., Koshino, M.: Lattice relaxation and energy band modulation in twisted bilayer graphene. *Phys. Rev. B* **96**, 075311 (2017)
- [15] Zhang, Y.-H., Senthil, T.: Bridging hubbard model physics and quantum hall physics in trilayer graphene/h-bn moiré superlattice. *Phys. Rev. B* **99**, 205150 (2019)
- [16] Park, C.-H., Son, Y.-W., Yang, L., Cohen, M.L., Louie, S.G.: Electron beam supercollimation in graphene superlattices. *Nano Lett.* **8**, 2920–2924 (2008)
- [17] Li, T., Chen, H., Wang, K., Hao, Y., Zhang, L., Watanabe, K., Taniguchi, T., Hong, X.: Transport anisotropy in one-dimensional graphene superlattice in the high kronig-penney potential limit. *Phys. Rev. Lett.* **132**, 056204 (2024)
- [18] Sharpe, A.L., Fox, E.J., Barnard, A.W., Finney, J., Watanabe, K., Taniguchi, T., Kastner, M., Goldhaber-Gordon, D.: Emergent ferromagnetism near three-quarters filling in twisted bilayer graphene. *Science* **365**, 605–608 (2019)
- [19] Serlin, M., Tschirhart, C., Polshyn, H., Zhang, Y., Zhu, J., Watanabe, K., Taniguchi, T., Balents, L., Young, A.: Intrinsic quantized anomalous hall effect in a moiré heterostructure. *Science* **367**, 900–903 (2020)

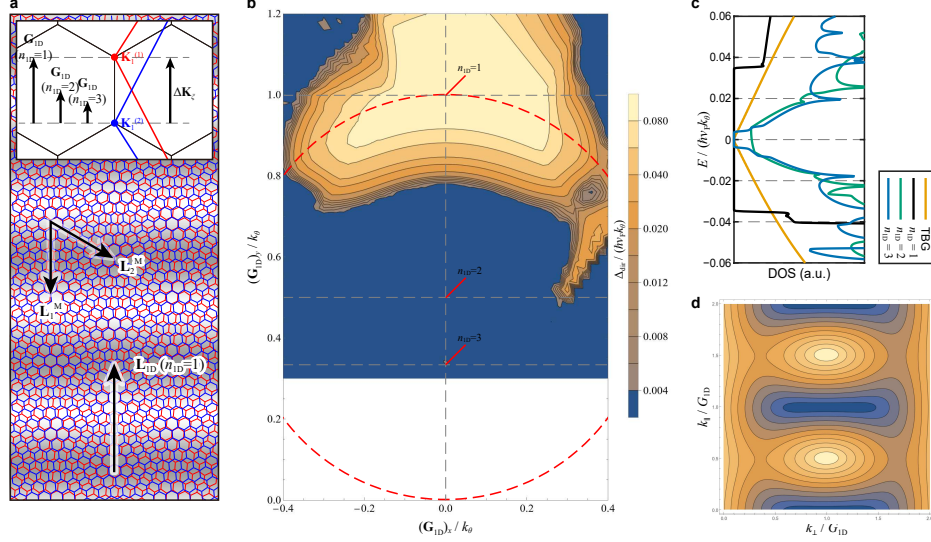


Fig. 1 Gate-defined configuration-space phase diagram. **a** Schematic of a moiré-1D hybrid superlattice: twisted bilayer graphene (red and blue hexagons) under a unidirectional scalar potential (shade) with wavevector $\mathbf{G}_{1D} = 2\pi\mathbf{L}_{1D}/|\mathbf{L}_{1D}|^2$. Inset illustrates \mathbf{G}_{1D} for several resonant configurations (Eq. (2)) $n_{1D} = 1, 2, 3$ in a reciprocal-space. Red and blue hexagons show the BZ of each graphene layer, black hexagons show the rBZ of TBG, and $\Delta\mathbf{K}_\xi(\theta)$ represents the moiré Dirac-point mismatch. See Fig. S2 for the rBZ of TBG-1D. **b** Full-wave continuum map of the direct gap at CNP, Δ_{dir} (in units of $\hbar v_F k_\theta$, log-scale), versus \mathbf{G}_{1D} at twist angle $\theta = 2^\circ$ for a layer-symmetric (in-phase) modulation ($|u_1| = |u_2| = 0.6$ and $\phi_1 = \phi_2 = 0$; see Fig. S8 for $\theta = 3^\circ$ and 5° , and numerical details in Methods and Supplementary Note S2). Resonance markers indicate \mathbf{G}_{1D} for $n_{1D} = 1, 2, 3$, which makes Dirac-Dirac matching, while the red-dashed circle highlights the near-resonant gapped arc around the $n_{1D} = 1$ resonance. This map corresponds to the default relative chirality class ($\chi_{\text{rel}} = +1$) of the layer-symmetric slice; chirality switching under layer-asymmetric modulation can reassign which resonances become gapped (Eq. (3), Figs. 3a and 3b). **c** DOS at a resonant configuration $n_{1D} = 1, 2, 3$ in **b** and that of a pristine TBG as a reference, illustrating the opening of a gap at CNP when n_{1D} is odd. **d** Band dispersion at an off-resonant configuration ($|\mathbf{G}_{1D}| = 50$ nm) in **b**, illustrating the anisotropic band flattening analogous to monolayer graphene under unidirectional scalar potential^[5-7] but at a weaker potential magnitude by the contribution from the moiré tunnelling (Eq. (4), Fig. 4, Supplementary Note S7)

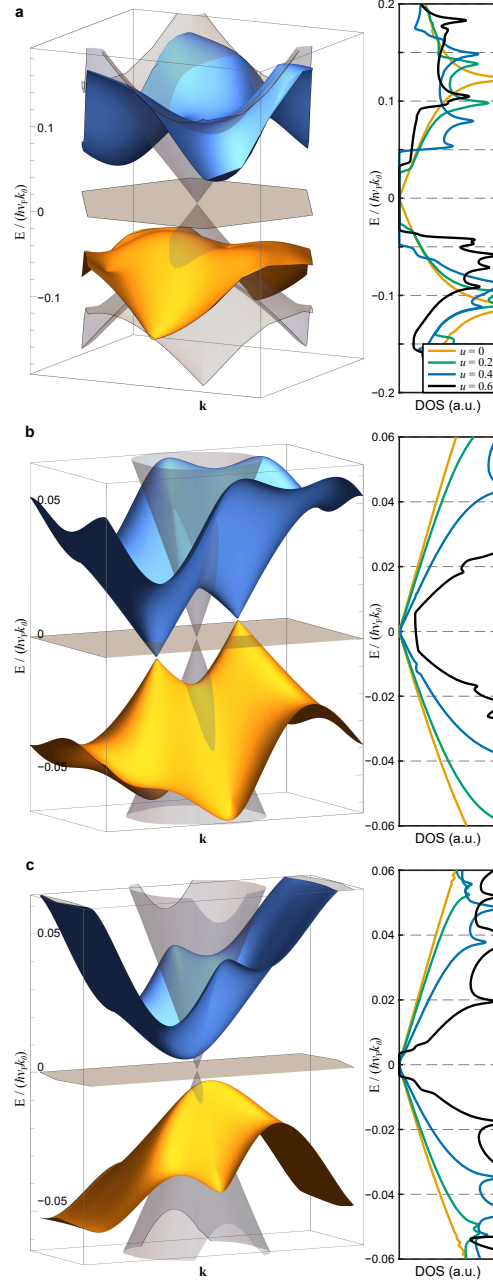


Fig. 2 Resonant spectra: n_{1D} parity selectivity in the default chirality class. (Left) Full-wave continuum minibands near the CNP of three resonant configurations (Eq. (2)) **a** $n_{1D} = 1$, **b** $n_{1D} = 2$, **c** $n_{1D} = 3$, at twist angle $\theta = 2^\circ$ under a layer-symmetric 1D modulation ($|u_1| = |u_2| = u$ and $\phi_1 = \phi_2 = 0$) with $u = 0.6$. Gray polygon at $E = 0$ represents the rBZ of each configuration (see Fig. S2). Gray cone shows the Dirac cone of pristine TBG in the absence of the unidirectional scalar potential for reference. (Right) DOS of each configuration with $u = 0, 0.2, 0.4, 0.6$. A robust CNP gap appears for the odd resonance $n_{1D} = 1, 3$, while the even resonance $n_{1D} = 2$ remains gapless in this default chirality class ($\chi_{\text{rel}} = +1$).

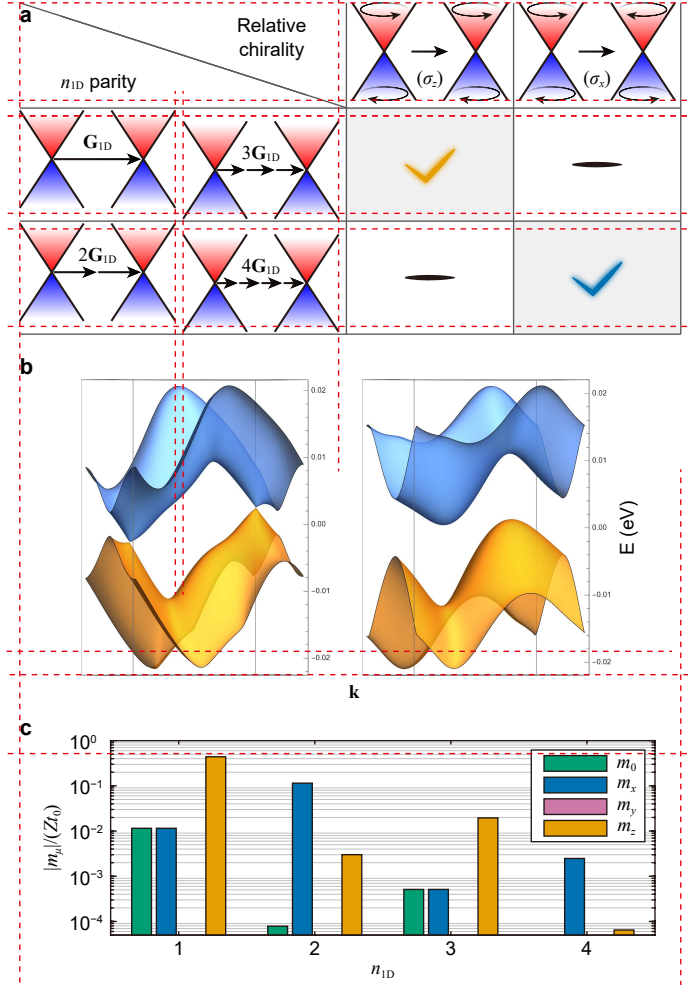


Fig. 3 Parity–chirality selection rule, chirality switching, and gap-opening channel control at Dirac–Dirac resonance. (a) Summary of the resonant gap-opening rule, organized by resonance parity (odd/even n_{1D}) and relative chirality class χ_{rel} (same/opposite pseudospin winding of the two resonant Dirac cones). The Pauli matrix shown in each chirality column indicates the mass channel that anticommutes with the corresponding effective two-cone Dirac Hamiltonian. See Supplementary Notes S3–S4. (b) Chirality inversion switches the resonance parity for gap opening and reassigns the mass channel: band structures at the even resonance $n_{1D} = 2$ for a strongly layer-asymmetric modulation in which u_2 is kept weak-to-moderate while $|u_1|$ is tuned from weak (left, $\chi_{\text{rel}} = +1$) to strong (right, $\chi_{\text{rel}} = -1$). Upon chirality switching, the gap-opening channel switches from σ_z to σ_x , enabling an even- n_{1D} CNP gap. The critical $|u_1|$ for chirality inversion in the full-wave spectrum can deviate slightly from simplified two-wave estimates due to additional dressing by remote states. (c) Pauli-channel decomposition of the effective resonant inter-cone coupling $Z\mathcal{M}^{(n_{1D})}$ for a layer-symmetric modulation (example shown for TBG–1D at $\theta = 3^\circ$ with $u_1 = u_2 = 1$ and $\phi_1 = \phi_2$). Writing $Z\mathcal{M}^{(n_{1D})} = m_0\mathbb{I} + m_x\sigma_x + m_y\sigma_y + m_z\sigma_z$, we plot the normalized magnitudes $|m_\mu|/(Zt_0)$ ($\mu = 0, x, y, z$) for $n_{1D} = 1$ to 4. The resonant coupling exhibits a parity-structured Pauli content: odd n_{1D} produces a prominent σ_z component, while even n_{1D} favors σ_x -type coupling, which becomes the mass channel only after chirality switching, consistent with the parity–chirality selection rule.

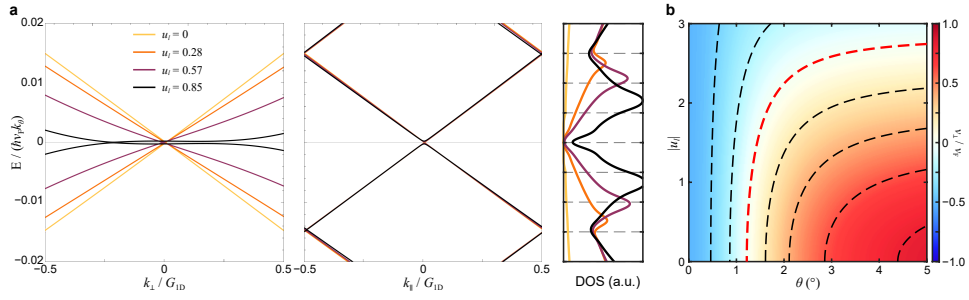


Fig. 4 Anisotropic band renormalization at off-resonance. **a** Off-resonant band structures ($|\mathbf{G}_{1D}| = 50$ nm, $\theta = 2^\circ$), along the direction perpendicular (left) and parallel (middle) to \mathbf{G}_{1D} , and DOS (right) near the CNP as a function of modulation strength u_l , illustrating continuously tunable anisotropy and progressive suppression of the transverse Dirac velocity in the Dirac-point neighborhood without opening a gap. **(b)** Map of the renormalized transverse velocity v_{\perp}^* versus twist angle θ and modulation strength $|u_l|$, highlighting the flattening line (red dashed line) where the low-energy transverse velocity approaches zero (Eq. (4)). The $|u_l|$ required for band flattening in TBG-1D is weaker than monolayer graphene under unidirectional potential ($|u_l| \sim 2.83$) due to the contribution from the moiré tunnelling (Eq. (4)).

Supplementary Information

for “Programmable Dirac masses in hybrid moiré–1D superlattices”

Hanzhou Tan¹ and Pilkyung Moon^{1,2,3*}

¹Arts and Sciences, NYU Shanghai, Shanghai, 200124, China.

²NYU-ECNU Institute of Physics at NYU Shanghai, Shanghai, 200062, China.

³Department of Physics, Hanyang University, Seoul, 04763, Korea.

*Corresponding author. E-mail: pilkyung.moon@nyu.edu

Contents

S1 Model setup and conventions	2
S1.1 Reference graphene lattice and twisted bilayer geometry	2
S1.2 Reciprocal-space geometry: Dirac points and moiré momenta	3
S1.3 Layer-dependent 1D scalar potential	4
S1.4 Configuration space: resonance, periodicity and momentum mismatch	4
S1.5 Choice of basis and representations	5
S1.6 Energy scales and dimensionless couplings	5
S2 Full-wave miniband calculations and spectral diagnostics	6
S2.1 Continuum Hamiltonian and assumptions	6
S2.2 Plane-wave basis and truncation	7
S2.3 Momentum-space matrix elements and numerical diagonalization	7
S2.4 Periodic superlattice geometries: rBZ sampling and direct-gap diagnostics	8
S2.5 Unfolded spectral function, DOS normalization, and band opening in quasiperiodic geometries	8
S2.6 Convergence and numerical settings	9
S3 Dressed representation: unitary rotation of the 1D potential	9
S3.1 Coordinate convention for the 1D modulation	9
S3.2 Layer-dependent unitary rotation and dressed Hamiltonian	9
S3.3 Dressed intralayer Dirac Hamiltonian, harmonic structure, and intralayer parity	10
S3.4 Dressed interlayer tunnelling and strategy for later truncations	11
S3.5 Explicit form of $\tilde{T}_0^\xi(y)$ and its harmonic building blocks	11
S4 Exact resonance: minimal-wave theory and parity–chirality selection rule	12
S4.1 1D periodicity and the reduced-zone (strip) basis	12
S4.2 Dressed intralayer blocks in reduced-zone basis and the central-harmonic projection	13
S4.3 Dressed interlayer tunnelling in reduced-zone basis, single resonant harmonic \tilde{T}_{0,p_0}^ξ , and leading-order parity rule	13
S4.4 Self-energy correction from remote channels	14
S4.5 Minimal two-cone model and the parity–chirality selection rule on gap-opening channel	15
S4.6 Rank structure of rigid interlayer tunneling and why Moiré–1D can open a Dirac gap	19
S4.7 Layer-symmetric component of the 1D modulation and the resonant gap scale	21
S4.8 Scaling of the resonant coupling with $ n_{1D} $	21
S4.9 Weak-1D limit ($ u_l \ll 1$): expansions for velocities and \mathcal{M}	22
S4.10 Validity and limitations	22

S5 Near resonance: gapped arcs from a detuned two-cone model	22
S5.1 Momentum mismatch and momentum-mismatched two-cone Hamiltonian	23
S5.2 Gapped region in momentum-mismatch space $\delta\mathbf{q}_\xi$: filled ellipse	24
S5.3 Gapped region in (fixed- $\Delta\mathbf{K}_\xi$) \mathbf{G}_{1D} space: arc	25
S5.4 Complementary representation: gapped region in (fixed \mathbf{G}_{1D}) $\Delta\mathbf{K}_\xi$ space: filled ellipse	26
S5.5 Beyond the near-resonant, gapped region	26
S5.6 Practical notes	26
S6 Berry-curvature diagnostics and Chern-triviality	27
S6.1 $C_{2z}T$ symmetry and Chern-triviality in scalar TBG–1D	27
S6.2 Non-Abelian Fukui curvature and valley Chern number	27
S7 Off resonance: perturbative anisotropic Dirac velocities	28
S7.1 Coordinate convention and minimal low-energy subspace	28
S7.2 Minimal momentum-space Hamiltonian and P/Q partition	28
S7.3 Löwdin downfolding and controlled linearization	29
S7.4 Renormalized Dirac Hamiltonian and anisotropic velocities	29
S7.5 Limiting cases, flattening line, and interpretation	30
S7.6 Neglected terms and validity	30
S8 Feasibility estimates	31
S8.1 Experimental knobs	32
S8.2 Resonant and near-resonant geometric design and mass channel magnitude	32
S8.3 Electrostatics: finite-distance attenuation of a periodic gate potential and parity leakage from higher (even) harmonics	34
S8.4 Geometric errors and tolerances	35
S8.5 Off-resonant feasibility and one-directional velocity renormalization	36

Supplementary Note S1 Model setup and conventions

This note fixes the geometric and notational conventions for the hybrid moiré–1D superlattice realized by twisted bilayer graphene (TBG) under an additional unidirectional (1D) periodic scalar potential (“TBG–1D”).

The key geometric quantity controlling the low-energy physics is the relation between the Dirac-point mismatch $\Delta\mathbf{K}_\xi(\theta)$ and the 1D reciprocal vector \mathbf{G}_{1D} , which defines resonant points and momentum-mismatch. Complementary to this geometric knob, the low-energy spectrum is also controlled by the layer-resolved 1D modulation parameters u_l ($l = 1, 2$) defined in Sec. S1.6. In particular, tuning the modulation strength and layer asymmetry can switch the relative chirality χ_{rel} of the two interacting Dirac cones and thereby control which Pauli channel opens the gap in the resonant and near-resonant regimes (see Sec. S4.5).

Supplementary Note S1.1 Reference graphene lattice and twisted bilayer geometry

We start from a reference monolayer graphene with lattice constant $a \approx 0.246$ nm and primitive vectors $\mathbf{a}_1 = a(1, 0)$, $\mathbf{a}_2 = a(1/2, \sqrt{3}/2)$, with reciprocal vectors \mathbf{b}_i defined by $\mathbf{a}_i \cdot \mathbf{b}_j = 2\pi\delta_{ij}$, and sublattice coordinates $\boldsymbol{\tau}_A = (0, 0)$, $\boldsymbol{\tau}_B = (\mathbf{a}_1 - 2\mathbf{a}_2)/3$. We define the graphene layer l ($l = 1, 2$, where $l = 1$ is the bottom layer) by rotating the reference lattice in the fixed laboratory frame

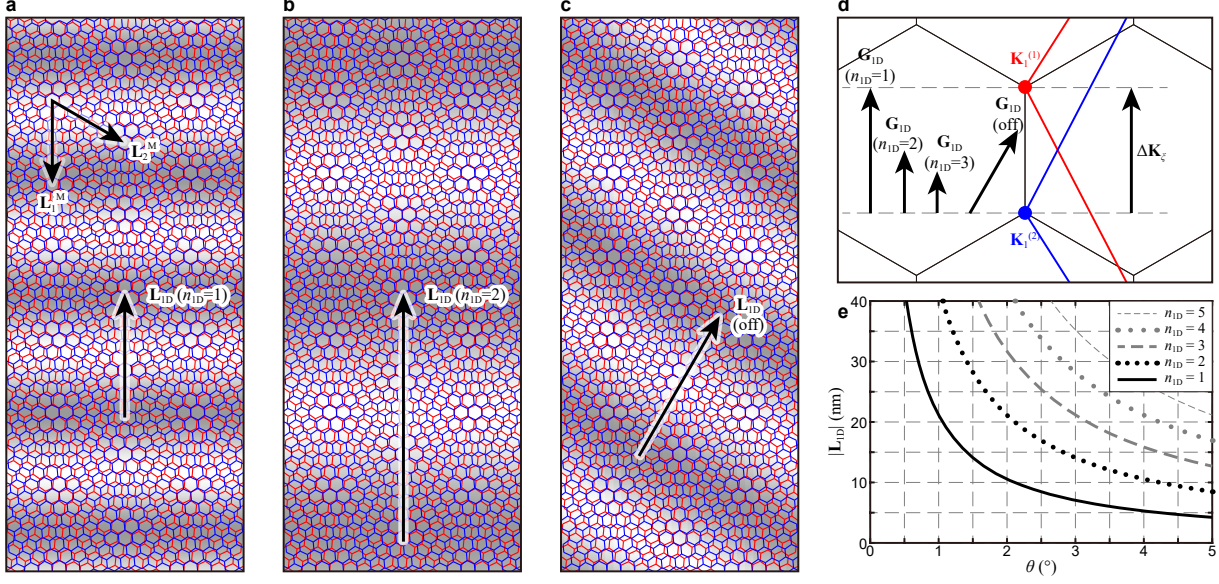


Figure S1: **a-c**. Lattice structures and unidirectional potential profiles of TBG-1D ($\theta = 10^\circ$). Red and blue lines represent the lattices of layers 1 and 2, respectively, and the unidirectional shade exhibits the 1D scalar potential (Eq. (S3)). **a** and **b** show the resonant configuration with n_{1D} of 1 and 2, respectively, while **c** shows an off-resonant configuration (Sec. S1.4). **d**. Reduced Brillouin zone of TBG (black lines) near $\mathbf{K}_1^{(l)}$, monolayer Brillouin zone of layer 1 (red lines) and 2 (blue lines), and \mathbf{G}_{1D} (black arrows) for $n_{1D} = 1$ (**a**), $n_{1D} = 2$ (**b**), $n_{1D} = 3$, and off-resonant configuration (**c**). **e**. Real-space period of the unidirectional potential ($|\mathbf{L}_{1D}|$) for $n_{1D} = 1$ to 5 plotted against θ .

by θ_l ($\theta_1 = -\theta/2$, $\theta_2 = \theta/2$), i.e., $\mathbf{a}_i^{(l)} = R(\theta_l)\mathbf{a}_i$, $\mathbf{b}_i^{(l)} = R(\theta_l)\mathbf{b}_i$, $\boldsymbol{\tau}_X^{(l)} = R(\theta_l)\boldsymbol{\tau}_X$, where $i = 1, 2$, $X = A, B$, with the rotation matrix $R(\phi) = \begin{pmatrix} \cos \phi & -\sin \phi \\ \sin \phi & \cos \phi \end{pmatrix}$.

Supplementary Note S1.2 Reciprocal-space geometry: Dirac points and moiré momenta

We label valleys by $\xi = \pm 1$ and define the Dirac point of layer l as $\mathbf{K}_\xi^{(l)} = -\xi(2\mathbf{b}_1^{(l)} + \mathbf{b}_2^{(l)})/3$. The Dirac-point mismatch between the two layers is

$$\Delta\mathbf{K}_\xi(\theta) \equiv \mathbf{K}_\xi^{(1)} - \mathbf{K}_\xi^{(2)}. \quad (\text{S1})$$

For the symmetric layer rotation defined above, $\Delta\mathbf{K}_\xi = k_\theta(0, \xi) \parallel \hat{\mathbf{y}}$, where $k_\theta \equiv |\Delta\mathbf{K}_\xi| = (8\pi/3a)\sin(\theta/2)$. The moiré reciprocal lattice vectors are $\mathbf{G}_i^M = \mathbf{b}_i^{(1)} - \mathbf{b}_i^{(2)}$ ($i = 1, 2$), and the corresponding real-space moiré superlattice vectors \mathbf{L}_i^M are defined by duality, $\mathbf{L}_i^M \cdot \mathbf{G}_j^M = 2\pi\delta_{ij}$, $|\mathbf{L}_i^M| = a/(2\sin(\theta/2))$ (Fig. S1a).

Finally, we define the three first-star moiré interlayer tunnelling momentum shifts¹⁻⁴

$$\mathbf{q}_0^\xi = \mathbf{K}_\xi^{(1)} - \mathbf{K}_\xi^{(2)}, \quad \mathbf{q}_j^\xi = (C_3)^j \mathbf{q}_0^\xi \quad (j = 0, 1, 2), \quad (\text{S2})$$

where C_3 denotes a counterclockwise rotation by $2\pi/3$ acting on momentum vectors. By definition, $\mathbf{q}_0^\xi = \Delta\mathbf{K}_\xi$.

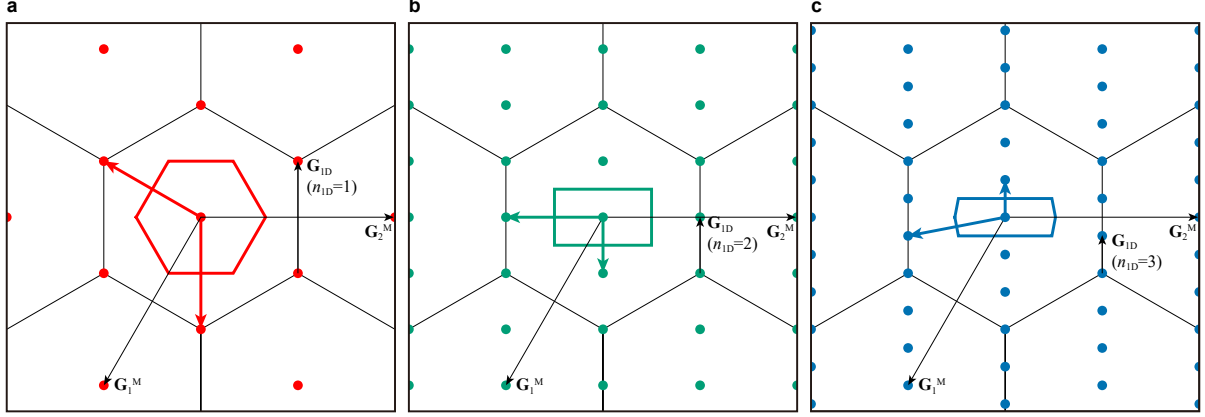


Figure S2: Periodicity in the reciprocal space of resonant configurations **a** $n_{1D} = 1$, **b** $n_{1D} = 2$, **c** $n_{1D} = 3$. \mathbf{G}_i^M ($i = 1, 2$) represent the reciprocal lattice vectors of TBG, and \mathbf{G}_{1D} show the reciprocal vector of the unidirectional potential. Hexagons in **a** and **c** and rectangle in **b** show the rBZ in each configuration.

Supplementary Note S1.3 Layer-dependent 1D scalar potential

We apply to each layer l a unidirectional periodic scalar potential with a common reciprocal vector \mathbf{G}_{1D} ,

$$V_l(\mathbf{r}) = \frac{|v_l|}{2} \cos(\mathbf{G}_{1D} \cdot \mathbf{r} + \phi_l) = \frac{v_l}{4} e^{i\mathbf{G}_{1D} \cdot \mathbf{r}} + \frac{v_l^*}{4} e^{-i\mathbf{G}_{1D} \cdot \mathbf{r}}, \quad (\text{S3})$$

where $|v_l|$ and ϕ_l are the amplitude and phase, and we define the complex parameter $v_l \equiv |v_l|e^{i\phi_l}$. The corresponding real-space period vector can be chosen as $\mathbf{L}_{1D} = 2\pi\mathbf{G}_{1D}/G_{1D}^2$ ($G_{1D} \equiv |\mathbf{G}_{1D}|$).

The direction of \mathbf{G}_{1D} is a geometric design parameter. For analytic work (Supplementary Notes S3–S5 and S7) we will often adopt a coordinate convention in which $\mathbf{G}_{1D} \parallel \hat{y}$, so that the 1D modulation depends only on y . All physical statements are then naturally interpreted in terms of components parallel/perpendicular to \mathbf{G}_{1D} .

Supplementary Note S1.4 Configuration space: resonance, periodicity and momentum mismatch

The effect of the 1D modulation on the low-energy spectrum is governed by the geometric relation between $\Delta\mathbf{K}_\xi(\theta)$ and \mathbf{G}_{1D} . For fixed twist angle θ , $\Delta\mathbf{K}_\xi$ is fixed; varying the direction and magnitude of \mathbf{G}_{1D} therefore defines a natural configuration map in the two-dimensional \mathbf{G}_{1D} design space.

We distinguish two independent notions of (in)commensurability in the combined moiré–1D problem: momentum resonance vs. global periodicity. These two notions are logically independent; for example, a system can be resonant yet quasiperiodic.

Momentum resonance. Momentum (Dirac) resonance refers to whether an integer harmonic of the 1D modulation can bridge the Dirac-point mismatch,

$$\Delta\mathbf{K}_\xi = \xi n_{1D}\mathbf{G}_{1D}, \quad n_{1D} \in \mathbb{Z}, \quad (\text{S4})$$

in which case we call the configuration resonant. Otherwise we call it off-resonant. In real space, Eq. (S4) is equivalent to the commensurability relation

$$\mathbf{L}_{1D} = -\frac{3}{2}n_{1D}\mathbf{L}_1^M = \frac{3a}{4\sin(\theta/2)} \begin{pmatrix} 0 \\ n_{1D} \end{pmatrix}, \quad (\text{S5})$$

meaning that the period vector of the unidirectional potential is collinear with a moiré superlattice vector \mathbf{L}_1^M (Figs. S1a and S1b). Figure S2 show the rBZ in the resonant configurations with $n_{1D} = 1, 2, 3$. See Sec. S4 for the effective Hamiltonian and the origin of the parity–chirality selection rule for gap-opening.

The exact resonant condition Eq. (S4) constrains both the direction and the magnitude of \mathbf{G}_{1D} ; hence resonant configurations form discrete points (measure zero) in the configuration map (Fig. 1b). To quantify deviations from a resonant point labelled by n_{1D} , we define the momentum-mismatch vector

$$\delta\mathbf{q}_\xi^{(n_{1D})} \equiv \Delta\mathbf{K}_\xi - \xi n_{1D}\mathbf{G}_{1D}. \quad (\text{S6})$$

Generic configurations are off-resonant ($\delta\mathbf{q}_\xi^{(n_{1D})} \neq \mathbf{0}$ for all integers n_{1D}), in which case there is no direct Dirac–Dirac resonance and the spectrum near charge neutrality remains gapless, albeit with a strongly anisotropic velocity renormalization (Sec. S7). Nevertheless, resonance-like features persist within a finite near-resonant neighborhood of the points when $|\delta\mathbf{q}_\xi^{(n_{1D})}|$ is sufficiently small. A systematic treatment of this near-resonant regime is presented in Sec. S5.

Global periodicity. Global periodicity refers to whether the combined reciprocal vectors generate a rank-2 lattice, i.e.,

$$\exists (m_1, m_2, m_3) \in \mathbb{Z}^3 \setminus \{\mathbf{0}\} : m_1\mathbf{G}_1^M + m_2\mathbf{G}_2^M + m_3\mathbf{G}_{1D} = \mathbf{0}. \quad (\text{S7})$$

When Eq. (S7) holds, the geometry is periodic and a reduced Brillouin zone (rBZ) exists. In practice, we construct a Wigner–Seitz cell for the combined reciprocal lattice $\mathcal{L}^* \equiv \{m_1\mathbf{G}_1^M + m_2\mathbf{G}_2^M + m_3\mathbf{G}_{1D} \mid m_{1,2,3} \in \mathbb{Z}\}$. If Eq. (S7) is not satisfied, the geometry is quasiperiodic (rank-3) and no globally defined rBZ exists.

Supplementary Note S1.5 Choice of basis and representations

In the remainder of this Supplementary Note, we adopt two complementary representations. For numerical electronic-structure calculations and global spectral diagnostics (Sec. S2), as well as for the perturbative analysis of the off-resonant regime (Sec. S7), we use the explicit-potential (non-dressed) representation in a momentum-space Bloch basis. This representation preserves the full lattice structure and is well suited for unbiased full-wave calculations and Brillouin-zone-wide analyses. By contrast, the unitary-rotated (dressed) representation is introduced specifically to isolate the resonant channels of the resonant regime and to enable transparent analytical derivations of the even–odd n_{1D} parity rule and the associated chirality dependence (Secs. S3–S5).

Supplementary Note S1.6 Energy scales and dimensionless couplings

We define the moiré and 1D kinetic energy scales $\mathcal{E}_\theta \equiv \hbar v_F k_\theta$ and $\mathcal{E}_{1D} \equiv \hbar v_F G_{1D}$ and the normalized moiré and 1D potential strength

$$u_0 \equiv \frac{t_0}{\mathcal{E}_\theta}, \quad u_l \equiv \frac{v_l}{\mathcal{E}_{1D}} = |u_l|e^{i\phi_l} \quad (l = 1, 2), \quad (\text{S8})$$

where $t_0 \approx 0.110$ eV is the moiré tunnelling strength. These dimensionless couplings control not only the strength of Bragg scattering but also how each Dirac cone is dressed by the 1D modulation. In the dressed representation, this dressing can renormalize and even reverse the sign of the effective Dirac velocity transverse to the modulation, providing a practical knob to switch the relative chirality χ_{rel} and thereby control the resonant gap-opening channel (Secs. S3–S4).

Supplementary Note S2 Full-wave miniband calculations and spectral diagnostics

This note provides a compact, reproducible summary of the full-wave numerical workflow used to generate the configuration maps (Fig. 1b) and electronic band structures (Fig. 2) in the main text. We neglect spin–orbit coupling and intervalley scattering. We treat valleys $\xi = \pm 1$ independently and include spin/valley degeneracies ($g_s = 2$, $g_v = 2$) when forming observables such as the DOS. The neglect of intervalley scattering is justified because the momentum transfers generated by the moiré tunnelling and by the long-wavelength 1D modulation are parametrically small compared to the K – K' separation for $\theta \ll 1$ and $|\mathbf{L}_{1D}| \gg a$.

Supplementary Note S2.1 Continuum Hamiltonian and assumptions

Continuum Hamiltonian. In the layer–sublattice basis $\Psi(\mathbf{r}) = (\psi_{1A}, \psi_{1B}, \psi_{2A}, \psi_{2B})^T$, the single-valley Hamiltonian $H_\xi(\mathbf{r})$ takes the block form

$$H_\xi(\mathbf{r}) = \begin{pmatrix} h_\xi^{(1)}(-i\nabla) + V_1(\mathbf{r})\mathbb{I} & T_\xi^\dagger(\mathbf{r}) \\ T_\xi(\mathbf{r}) & h_\xi^{(2)}(-i\nabla) + V_2(\mathbf{r})\mathbb{I} \end{pmatrix}. \quad (\text{S9})$$

Here $h_\xi^{(l)}(-i\nabla) = -\hbar v_F(\xi(-i\nabla_x)\sigma_x^{(l)} + (-i\nabla_y)\sigma_y^{(l)})$ is the intralayer Dirac Hamiltonian, where $\sigma_x^{(l)} \equiv (\cos \theta_l)\sigma_x + (\sin \theta_l)\sigma_y$ and $\sigma_y^{(l)} \equiv -(\sin \theta_l)\sigma_x + (\cos \theta_l)\sigma_y$ are the layer-rotated Pauli matrices, and

$$T_\xi(\mathbf{r}) = \sum_{j=0}^2 T_j^\xi e^{i\mathbf{q}_j^\xi \cdot \mathbf{r}} \quad (\text{S10})$$

is the moiré first-star tunnelling. For the effective analytic models in Secs. S3–S5, we use the rigid (non-relaxed) tunnelling matrices^{1–4}

$$T_j^\xi = t_0 \begin{pmatrix} 1 & \omega^{-\xi j} \\ \omega^{\xi j} & 1 \end{pmatrix}, \quad \omega = e^{2\pi i/3}, \quad t_0 \approx 0.110 \text{ eV}, \quad (\text{S11})$$

for transparency, while in the numerical calculations we incorporate lattice-relaxation effects using the standard two-parameter first-star tunnelling model with distinct AA and AB/BA amplitudes

$$T_j^\xi = \begin{pmatrix} u_{AA} & u_{AB} \omega^{-\xi j} \\ u_{AB} \omega^{\xi j} & u_{AA} \end{pmatrix}, \quad (u_{AA} \leq u_{AB}). \quad (\text{S12})$$

Importantly, the even/odd harmonic structure derived from the $\omega^{\pm \xi j}$ phases is unchanged by this replacement. Therefore, the parity–chirality selection rule derived in Sec. S4 applies to both models.

Lattice relaxation. In low-angle TBG the lattice spontaneously relaxes to enlarge AB/BA domains and shrink AA regions, because the interlayer adhesion energy depends strongly on the local stacking configuration. We use the lattice relaxation model developed by Nam and Koshino⁵. The in-plane deformation is represented by layer displacement fields $\mathbf{u}^{(l)}(\mathbf{r})$ ($l = 1, 2$), which modify the local interlayer registry as $\boldsymbol{\delta}(\mathbf{r}) = \boldsymbol{\delta}_0(\mathbf{r}) + \mathbf{u}^-(\mathbf{r})$, $\mathbf{u}^-(\mathbf{r}) \equiv \mathbf{u}^{(2)}(\mathbf{r}) - \mathbf{u}^{(1)}(\mathbf{r})$, where $\boldsymbol{\delta}_0(\mathbf{r})$ is the registry field of the rigidly twisted bilayer. The relaxed configuration minimizes the total energy $U[\mathbf{u}^{(1)}, \mathbf{u}^{(2)}] = U_E + U_B$, given by an elastic term $U_E = \sum_{l=1}^2 \int d^2r [(\lambda/2)(\nabla \cdot \mathbf{u}^{(l)})^2 + \mu \sum_{i,j} u_{ij}^{(l)} u_{ij}^{(l)}]$, where $u_{ij}^{(l)} = (\partial_i u_j^{(l)} + \partial_j u_i^{(l)})/2$, λ, μ are Lamé coefficients, and an adhesion term $U_B = \int d^2r V[\boldsymbol{\delta}(\mathbf{r})]$, where $V[\boldsymbol{\delta}] = \sum_{j=1}^3 2V_0 \cos(\mathbf{b}_j \cdot \boldsymbol{\delta})$ and $\mathbf{b}_3 = -\mathbf{b}_1 - \mathbf{b}_2$. Using the identity $\mathbf{b}_j \cdot \boldsymbol{\delta}_0(\mathbf{r}) = \mathbf{G}_j^M \cdot \mathbf{r}$ (with $\mathbf{G}_3^M = -\mathbf{G}_1^M - \mathbf{G}_2^M$), the adhesion energy density becomes explicitly moiré periodic, $V[\boldsymbol{\delta}(\mathbf{r})] = \sum_{j=1}^3 2V_0 \cos(\mathbf{G}_j^M \cdot \mathbf{r} + \mathbf{b}_j \cdot \mathbf{u}^-(\mathbf{r}))$. The optimized solution yields a pronounced AB/BA domain pattern and suppresses the spatial weight of AA stacking in the moiré unit cell.

In the electronic continuum Hamiltonian, the dominant consequence of this relaxation is a reduction of the AA-type Fourier component of the moiré interlayer tunnelling relative to AB/BA. At the first-star level this is captured by the two-parameter tunnelling matrices in Eq. (S12) with $|u_{AA}| < |u_{AB}|$, which we use throughout the full-wave numerical calculations. (Out-of-plane corrugation primarily renormalizes the overall interlayer coupling scale and can be absorbed into the effective parameters u_{AA}, u_{AB} ; see Ref.⁵.)

Supplementary Note S2.2 Plane-wave basis and truncation

We choose a seed Bloch momentum \mathbf{k}_0 (measured from Γ in the laboratory frame) and generate the set of coupled momenta $\mathbf{k} = \mathbf{k}_0 + \mathbf{G}$ with $\mathbf{G} = m_1 \mathbf{G}_1^M + m_2 \mathbf{G}_2^M + m_3 \mathbf{G}_{1D}$, $m_{1,2,3} \in \mathbb{Z}$. We retain all basis states satisfying the cutoff $\hbar v_F |\mathbf{q}| \leq E_{\max}$ and verify convergence of all reported spectra and gap diagnostics by increasing E_{\max} .

Supplementary Note S2.3 Momentum-space matrix elements and numerical diagonalization

We work in the valley-resolved Bloch basis $|\mathbf{q}, X, l\rangle$ (with $X = A, B$ and $l = 1, 2$), where \mathbf{q} is measured from the valley point $\mathbf{K}_\xi^{(l)}$ in each layer, i.e., $\mathbf{q} \equiv \mathbf{k} - \mathbf{K}_\xi^{(l)}$, and define the Bloch states as^{3;4}

$$|\mathbf{q}, X, l\rangle = \frac{1}{\sqrt{N}} \sum_{\mathbf{R}^{(l)}} e^{i(\mathbf{q} + \mathbf{K}_\xi^{(l)}) \cdot (\mathbf{R}^{(l)} + \boldsymbol{\tau}_X^{(l)})} |\mathbf{R}^{(l)} + \boldsymbol{\tau}_X^{(l)}\rangle. \quad (\text{S13})$$

Here $\mathbf{R}^{(l)}$ runs over the Bravais lattice of layer l and $\boldsymbol{\tau}_X^{(l)}$ denotes the sublattice coordinate. In this basis the intralayer matrix element is

$$\langle \mathbf{q}', l' | h_\xi^{(l)}(-i\nabla) | \mathbf{q}, l \rangle = h_\xi^{(l)}(\mathbf{q}) \delta_{\mathbf{q}', \mathbf{q}} \delta_{l', l}, \quad (\text{S14})$$

where

$$h_\xi^{(l)}(\mathbf{q}) = -\hbar v_F (\xi q_x \sigma_x^{(l)} + q_y \sigma_y^{(l)}), \quad (\text{S15})$$

while the moiré tunnelling couples momenta differing by \mathbf{q}_j^ξ :

$$\langle \mathbf{q}', 2 | T_\xi(\mathbf{r}) | \mathbf{q}, 1 \rangle = \sum_{j=0}^2 T_j^\xi \delta_{\mathbf{q}', \mathbf{q} + \mathbf{q}_j^\xi}, \quad (\text{S16})$$

$$\langle \mathbf{q}, 1 | T_\xi^\dagger(\mathbf{r}) | \mathbf{q}', 2 \rangle = \langle \mathbf{q}', 2 | T_\xi(\mathbf{r}) | \mathbf{q}, 1 \rangle^\dagger.$$

Finally, the 1D scalar potential in layer l couples momenta shifted by $\pm\mathbf{G}_{1D}$ without mixing sublattices:

$$\langle \mathbf{q}', l' | V_l(\mathbf{r}) | \mathbf{q}, l \rangle = \left[\frac{v_l}{4} \delta_{\mathbf{q}', \mathbf{q} + \mathbf{G}_{1D}} + \frac{v_l^*}{4} \delta_{\mathbf{q}', \mathbf{q} - \mathbf{G}_{1D}} \right] \mathbb{I} \delta_{l', l}. \quad (\text{S17})$$

For each rBZ momentum \mathbf{q} , we construct the truncated Hamiltonian matrix $H_\xi^{(\text{full})}(\mathbf{q})$ for the Hilbert space defined in Sec. S2.2 using the matrix elements in Eqs. (S14)–(S17), and solve

$$H_\xi^{(\text{full})}(\mathbf{q}) \Psi_{n\xi}(\mathbf{q}) = E_{n\xi}(\mathbf{q}) \Psi_{n\xi}(\mathbf{q}), \quad (\text{S18})$$

where n labels the minibands in ascending energy order.

Supplementary Note S2.4 Periodic superlattice geometries: rBZ sampling and direct-gap diagnostics

Direct gap throughout the Brillouin zone. Globally periodic (rank-2) configurations have a periodic rBZ (Sec. S1.4). To determine whether the charge-neutral spectrum is insulating or gapless, we evaluate the band-edge gap function $g_\xi(\mathbf{q}) \equiv E_{c,\xi}(\mathbf{q}) - E_{v,\xi}(\mathbf{q})$, where $E_{c,\xi}(\mathbf{q})$ and $E_{v,\xi}(\mathbf{q})$ are, respectively, the lowest conduction and highest valence energies at crystal momentum \mathbf{q} in valley ξ . We then define the direct gap as

$$\Delta_{\text{dir}} \equiv \min_{\xi=\pm 1} \min_{\mathbf{q} \in \text{rBZ}} g_\xi(\mathbf{q}), \quad (\text{S19})$$

which provides a conservative criterion for a band touching anywhere in the rBZ ($\Delta_{\text{dir}} = 0$).

Supplementary Note S2.5 Unfolded spectral function, DOS normalization, and band opening in quasiperiodic geometries

In rank-3 (quasiperiodic) geometries (no exact rBZ), reciprocal-space coupling generates band replicas at quasiperiodically spaced momenta, in contrast to the strictly periodic copies in a globally periodic structure. To extract an unfolded dispersion at a chosen momentum \mathbf{k}_0 we compute the momentum-resolved spectral function

$$A_l(\mathbf{k}_0, \varepsilon) = \sum_{\alpha} \sum_{X=A,B} |\langle \alpha | \mathbf{k}_0, X, l \rangle|^2 \delta_\eta(\varepsilon - \varepsilon_\alpha), \quad (\text{S20})$$

where $|\alpha\rangle$ and ε_α are eigenstates and eigenenergies of the truncated Hamiltonian at seed momentum \mathbf{k}_0 , and δ_η is a normalized broadened delta function of width η (we use a smooth, normalized broadening; results are insensitive to the specific choice when η is smaller than the spectral features of interest). The layer-summed spectral function is $A(\mathbf{k}_0, \varepsilon) = \sum_l A_l(\mathbf{k}_0, \varepsilon)$.

In the converged plane-wave limit, shifting the seed momentum \mathbf{k}_0 by any reciprocal-module vector $m_1\mathbf{G}_1^M + m_2\mathbf{G}_2^M + m_3\mathbf{G}_{1D}$ only relabels basis states, so physical spectra become independent of such shifts. For rank-3 geometries we therefore sample \mathbf{k}_0 uniformly over a chosen compact reference window \mathcal{W} and normalize by its area, verifying convergence with respect to \mathcal{W} , the \mathbf{k}_0 mesh, and the plane-wave cutoff⁶. The DOS per real-space area is then defined as

$$D(\varepsilon) = g_s g_v \int_{\mathcal{W}} \frac{d^2 k_0}{(2\pi)^2} \sum_{\alpha} \delta_\eta(\varepsilon - \varepsilon_\alpha(\mathbf{k}_0)), \quad (\text{S21})$$

where $g_s = 2$ and $g_v = 2$ are the spin and valley degeneracies. For globally periodic configurations we set $\mathcal{W} = \text{rBZ}$ so that Eq. (S21) gives the total DOS per unit area; for rank-3 geometries we use a fixed finite \mathcal{W} and explicitly verify independence of \mathcal{W} upon convergence.

To diagnose a neutrality band opening in rank-3 geometries, we use the conservative estimator $\Delta_{\alpha\beta} \equiv \min_{\mathbf{k}_0 \in \mathcal{W}} [E_\alpha(\mathbf{k}_0) - E_\beta(\mathbf{k}_0)]$. Here (α, β) are chosen as the lowest conduction and highest valence bands around the CNP within the truncated spectrum.

Supplementary Note S2.6 Convergence and numerical settings

We verify the convergence and numerical robustness by the following checks: (i) increase E_{\max} until the relevant band dispersions and the CNP gap diagnostics are stable within the plotted resolution; (ii) refine the rBZ mesh (for periodic geometries) or the seed-momentum sampling mesh (for rank-3 geometries); (iii) for rank-3 geometries, enlarge the reference window \mathcal{W} to the next smallest polygonal reference window and verify that $D(\varepsilon)$ and $\Delta_{\alpha\beta}$ do not change; (iv) decrease the broadening η in δ_η to confirm that spectral features are not artificially smeared.

Supplementary Note S3 Dressed representation: unitary rotation of the 1D potential

Here we introduce an exact layer-dependent, position-dependent unitary transformation in sublattice space. The transformation leaves the spectrum invariant, but reorganizes the Hamiltonian such that the 1D scalar potentials $V_l(\mathbf{r})$ are absorbed into (i) a harmonic dressing of the intralayer kinetic terms and (ii) a harmonic dressing of the interlayer tunnelling. The parity structure of this unitary-rotated (dressed) representation provides a natural starting point for the resonant analysis in Secs. S4 and S5, where the Dirac–Dirac coupling is governed by a single resonant harmonic.

Supplementary Note S3.1 Coordinate convention for the 1D modulation

For the analytic development we choose the 1D reciprocal vector to be parallel to the y axis,

$$\mathbf{G}_{1D} = G_{1D}\hat{\mathbf{y}} = \begin{pmatrix} 0 \\ G_{1D} \end{pmatrix}, \quad (\text{S22})$$

anticipating its alignment with the Dirac-point mismatch $\Delta\mathbf{K}_\xi$ in the resonant configuration discussed later (Secs. S4 and S5). Importantly, apart from this directional choice, the formulation developed here remains general and applies equally to off-resonant configurations as long as $\mathbf{G}_{1D} \parallel \hat{\mathbf{y}}$. With Eq. (S22), the layer-dependent scalar potential becomes

$$V_l(\mathbf{r}) = V_l(y) = \frac{|v_l|}{2} \cos(G_{1D}y + \phi_l), \quad v_l = |v_l|e^{i\phi_l}. \quad (\text{S23})$$

Supplementary Note S3.2 Layer-dependent unitary rotation and dressed Hamiltonian

We define a layer-dependent unitary rotation in sublattice space,

$$U_l(y) \equiv \exp\left[\frac{i}{2}\alpha_l(y)\sigma_y^{(l)}\right], \quad l = 1, 2, \quad (\text{S24})$$

with the phase field $\alpha_l(y)$ chosen to satisfy

$$\alpha'_l(y) \equiv \frac{2}{\hbar v_F} V_l(y). \quad (\text{S25})$$

For the $V_l(y)$ defined in Eq. (S23), $\alpha'_l(y)$ integrates to

$$\alpha_l(y) = |u_l| \sin(G_{1D}y + \phi_l), \quad (\text{S26})$$

where we fix the additive constant such that $\langle \alpha_l(y) \rangle_y = 0$. Since $\alpha_l(y + 2\pi/G_{1D}) = \alpha_l(y)$, $U_l(y)$ is periodic in y with period $2\pi/G_{1D}$.

A related sublattice-dependent unitary transformation has previously been employed to incorporate a unidirectional scalar potential into the intralayer Dirac Hamiltonian of monolayer graphene^{7;8}. Here we extend this transformation to a bilayer moiré system and show that, in addition to dressing the intralayer kinetics, it generates a harmonic dressing of the interlayer tunnelling, which plays a central role in the Dirac–Dirac resonance discussed below.

We apply the block-diagonal unitary transformation $U(y) = \text{diag}(U_1(y), U_2(y))$ to the full real-space Hamiltonian $H_\xi(\mathbf{r})$ and define the unitary-transformed Hamiltonian

$$\begin{aligned} \tilde{H}_\xi(\mathbf{r}) &\equiv U^\dagger(y) H_\xi(\mathbf{r}) U(y) \\ &= \begin{pmatrix} U_1^\dagger(y) [h_\xi^{(1)}(-i\nabla) + V_1(y)\mathbb{I}] U_1(y) & U_1^\dagger(y) T_\xi^\dagger(\mathbf{r}) U_2(y) \\ U_2^\dagger(y) T_\xi(\mathbf{r}) U_1(y) & U_2^\dagger(y) [h_\xi^{(2)}(-i\nabla) + V_2(y)\mathbb{I}] U_2(y) \end{pmatrix} \\ &\equiv \begin{pmatrix} \tilde{h}_\xi^{(1)}(-i\nabla) & \tilde{T}_\xi^\dagger(\mathbf{r}) \\ \tilde{T}_\xi(\mathbf{r}) & \tilde{h}_\xi^{(2)}(-i\nabla) \end{pmatrix}, \end{aligned} \quad (\text{S27})$$

where we used $U_l^\dagger \sigma_y^{(l)} (-i\partial_y) U_l = \sigma_y^{(l)} (-i\partial_y) + (\alpha'_l(y)/2)\mathbb{I}$. Because $U(y)$ is unitary, \tilde{H}_ξ is isospectral to H_ξ and remains Hermitian.

Supplementary Note S3.3 Dressed intralayer Dirac Hamiltonian, harmonic structure, and intralayer parity

A key feature of the choice Eq. (S25) is that the scalar potential is absorbed into the dressed intralayer kinetic terms,

$$\tilde{h}_\xi^{(l)}(-i\nabla) = -\hbar v_F \left[\xi (\cos \alpha_l(y) \sigma_x^{(l)} - \sin \alpha_l(y) \sigma_z) (-i\partial_x) + \sigma_y^{(l)} (-i\partial_y) \right], \quad l = 1, 2. \quad (\text{S28})$$

Since $\alpha_l(y)$ is periodic, we expand $\cos \alpha_l(y) = \sum_{p \in \mathbb{Z}} C_{l,p} e^{ipG_{1D}y}$ and $\sin \alpha_l(y) = \sum_{p \in \mathbb{Z}} S_{l,p} e^{ipG_{1D}y}$. Using the Jacobi–Anger expansion $e^{iz \sin t} = \sum_{p \in \mathbb{Z}} J_p(z) e^{ipt}$ with $t = G_{1D}y + \phi_l$, the coefficients take the closed form

$$C_{l,p} = \begin{cases} J_p(|u_l|) e^{ip\phi_l}, & p \text{ even,} \\ 0, & p \text{ odd,} \end{cases} \quad S_{l,p} = \begin{cases} 0, & p \text{ even,} \\ -i J_p(|u_l|) e^{ip\phi_l}, & p \text{ odd,} \end{cases} \quad (\text{S29})$$

with J_p the Bessel function of the first kind. Thus, $\cos \alpha_l$ contains only even harmonics and $\sin \alpha_l$ contains only odd harmonics. Moreover, $C_{l,-p} = C_{l,p}^*$ and $S_{l,-p} = S_{l,p}^*$, ensuring that $\cos \alpha_l$ and $\sin \alpha_l$ are real as required.

Equation (S28) makes explicit that, in the unitary-rotated basis, all y -harmonic mixing in the intralayer problem enters through the $-i\partial_x$ term (i.e., q_x), whereas the $-i\partial_y$ term remains diagonal in the harmonic index. This structural fact will be central to the minimal-wave model and the parity selection rule in Sec. S4.

Supplementary Note S3.4 Dressed interlayer tunnelling and strategy for later truncations

The dressed interlayer tunnelling inherits the same y -periodicity:

$$\tilde{T}_\xi(\mathbf{r}) = \sum_{j=0}^2 \tilde{T}_j^\xi(y) e^{i\mathbf{q}_j^\xi \cdot \mathbf{r}}, \quad \tilde{T}_j^\xi(y) \equiv U_2^\dagger(y) T_j^\xi U_1(y), \quad j = 0, 1, 2. \quad (\text{S30})$$

Because $U_{1,2}(y)$ are periodic in y , we expand $\tilde{T}_j^\xi(y) = \sum_{p \in \mathbb{Z}} \tilde{T}_{j,p}^\xi e^{ipG_{1D}y}$. In the resonant analysis (Secs. S4 and S5) we will adopt a central-harmonic (minimal-wave) truncation tailored to the low-energy Dirac–Dirac interaction. Within that construction, the resonant coupling is controlled by a single Fourier component of the $j = 0$ channel, while $j = 1, 2$ enter only through remote processes that renormalize velocities and produce subleading corrections. Accordingly, we provide below the explicit y -dependence of $\tilde{T}_0^\xi(y)$, and we parameterize its harmonics in a form suited for extracting the resonant component in Sec. S4.

Supplementary Note S3.5 Explicit form of $\tilde{T}_0^\xi(y)$ and its harmonic building blocks

We introduce the layer-symmetric and layer-antisymmetric combinations

$$\begin{aligned} u_\pm &\equiv u_1 \pm u_2 \equiv |u_\pm| e^{i\phi_\pm}, \\ \alpha_\pm(y) &\equiv \alpha_1(y) \pm \alpha_2(y) = |u_\pm| \sin(G_{1D}y + \phi_\pm), \\ \mathcal{J}_{\pm,p} &\equiv J_p(|u_\pm|/2) e^{ip\phi_\pm}. \end{aligned} \quad (\text{S31})$$

Then,

$$\tilde{T}_0^\xi(y) = t_0 [A_I(y) \mathbb{I} + A_x(y) \sigma_x + A_y(y) \sigma_y + A_z(y) \sigma_z], \quad (\text{S32})$$

in the common (A, B) sublattice basis with

$$\begin{aligned} A_I(y) &= c^2 \cos \frac{\alpha_-(y)}{2} + s^2 \cos \frac{\alpha_+(y)}{2} + i s \sin \frac{\alpha_+(y)}{2}, \\ A_x(y) &= \cos \frac{\alpha_+(y)}{2} + i s \sin \frac{\alpha_+(y)}{2}, \\ A_y(y) &= i c \sin \frac{\alpha_-(y)}{2}, \\ A_z(y) &= -c \sin \frac{\alpha_+(y)}{2} - i s c \left(\cos \frac{\alpha_-(y)}{2} - \cos \frac{\alpha_+(y)}{2} \right), \end{aligned} \quad (\text{S33})$$

where we defined $c \equiv \cos(\theta/2)$ and $s \equiv \sin(\theta/2)$. All y dependence of $\tilde{T}_0^\xi(y)$ is therefore controlled by $\cos(\alpha_\pm/2)$ and $\sin(\alpha_\pm/2)$, which we expand as $\cos(\alpha_\pm(y)/2) = \sum_{p \in \mathbb{Z}} C_{\pm,p} e^{ipG_{1D}y}$ and $\sin(\alpha_\pm(y)/2) = \sum_{p \in \mathbb{Z}} S_{\pm,p} e^{ipG_{1D}y}$, with coefficients

$$C_{\pm,p} = \begin{cases} \mathcal{J}_{\pm,p}, & p \text{ even}, \\ 0, & p \text{ odd}, \end{cases} \quad S_{\pm,p} = \begin{cases} 0, & p \text{ even}, \\ -i\mathcal{J}_{\pm,p}, & p \text{ odd}. \end{cases} \quad (\text{S34})$$

Equation (S34) is the interlayer analogue of Eq. (S29) and encodes the same even/odd harmonic parity. In Sec. S4, we show that this parity structure enforces the parity rule responsible for the gap opening in the resonant configuration through the Pauli component of a single resonant Fourier harmonic of $\tilde{T}_0^\xi(y)$.

Supplementary Note S4 Exact resonance: minimal-wave theory and parity–chirality selection rule

We develop a compact few-wave description of the low-energy electronic structure of resonant TBG–1D, defined by the Dirac-resonance condition Eq. (S4). Starting from the unitary-rotated Hamiltonian $\tilde{H}_\xi(\mathbf{r})$, we derive a minimal two-cone model that captures the direct intercone resonance responsible for the resonant-gap physics. This framework makes the parity–chirality selection rule—even/odd resonant harmonic n_{1D} and same/opposite Dirac-cone chirality χ_{rel} —transparent, to leading order in small θ : depending on the relative chirality between the Dirac cones renormalized by the 1D potential, only one of even or odd n_{1D} can host a Pauli component that opens a gap at the Dirac point.

Approximation scheme. Throughout this note we work to linear order in the reduced momentum \mathbf{q} about each Dirac point. The intralayer dressing by the 1D potential is kept nonperturbatively through the central-harmonic factor $\eta_l = J_0(|u_l|)$. For the interlayer sector, we retain only the two central cones (the $m = 0$ sectors in each layer) and the single resonant harmonic $\mathcal{M}_\xi^{(n_{1D})}$, corresponding to the $-\xi n_{1D}$ th harmonic of the dressed $j = 0$ tunnelling \tilde{T}_0^ξ , with its amplitude kept exact in u_l through the Bessel coefficients.

Supplementary Note S4.1 1D periodicity and the reduced-zone (strip) basis

For the symmetric layer rotation $\theta_1 = -\theta/2$ and $\theta_2 = \theta/2$ in this work, the \mathbf{G}_{1D} for a commensurate configuration is always parallel to \hat{y} . In the resonant analysis, after retaining the $j = 0$ channel explicitly (and treating $j = 1, 2$ as remote self-energy contributions, Sec. S4.4), the effective low-energy Hamiltonian is periodic in y with period $2\pi/G_{1D}$; hence we introduce the one-dimensional rBZ associated with \mathbf{G}_{1D} ,

$$-\frac{G_{1D}}{2} \leq q_y < \frac{G_{1D}}{2}. \quad (\text{S35})$$

For a given layer l and valley ξ , any valley-centered momentum relative to the Dirac point, $\mathbf{k} - \mathbf{K}_\xi^{(l)}$, can be uniquely decomposed as

$$\mathbf{k} - \mathbf{K}_\xi^{(l)} \equiv \tilde{\mathbf{q}}_m = \mathbf{q} + m\mathbf{G}_{1D} = (q_x, q_y + mG_{1D}), \quad (\text{S36})$$

where $\mathbf{q} = (q_x, q_y)$ lies in the rBZ and $m \in \mathbb{Z}$ labels the corresponding harmonic (sector) index. We therefore introduce two-component sublattice spinors

$$|\mathbf{q}, m, l\rangle \equiv (|\mathbf{q}, m, A, l\rangle, |\mathbf{q}, m, B, l\rangle)^T, \quad (\text{S37})$$

with $|\mathbf{q}, m, X, l\rangle \equiv |\tilde{\mathbf{q}}_m, X, l\rangle = |\mathbf{q} + m\mathbf{G}_{1D}, X, l\rangle$ for $X = A, B$ and $l = 1, 2$, as sector basis states.

Layer-dependent folding. The mapping between (\mathbf{q}, m) and the Bloch momentum \mathbf{k} is layer dependent because $\mathbf{K}_\xi^{(1)} \neq \mathbf{K}_\xi^{(2)}$. In particular, the same reduced momentum \mathbf{q} corresponds to Bloch momenta shifted by $\Delta\mathbf{K}_\xi = \mathbf{K}_\xi^{(1)} - \mathbf{K}_\xi^{(2)}$ between the two layers. In a resonant configuration, the Dirac point of one layer is folded into a definite sector of the other with the same \mathbf{q} , and this folding enables a unique low-energy Dirac–Dirac resonance via a single Fourier component of the dressed tunnelling.

Supplementary Note S4.2 Dressed intralayer blocks in reduced-zone basis and the central-harmonic projection

A Fourier component of the y -periodic dressed Hamiltonian with harmonic index p couples the momentum sectors m and $m + p$. Accordingly, the dressed intralayer Hamiltonian in the reduced-zone basis is

$$\begin{aligned} & \langle \mathbf{q}', m', l' | \tilde{h}_\xi^{(l)}(-i\nabla) | \mathbf{q}, m, l \rangle \\ &= -\hbar v_F \left[\xi q_x (C_{l, m' - m} \sigma_x^{(l)} - S_{l, m' - m} \sigma_z) + (q_y + m G_{1D}) \sigma_y^{(l)} \delta_{m', m} \right] \delta_{\mathbf{q}', \mathbf{q}} \delta_{l', l}. \end{aligned} \quad (\text{S38})$$

Equation (S38) makes two structural facts explicit: (i) the longitudinal q_y term is diagonal in m ; and (ii) all m -mixing arises from the transverse q_x term through the harmonic coefficients $C_{l,p}$ and $S_{l,p}$.

Central-harmonic projection. To obtain a compact low-energy model, we retain only the central sector $m = 0$ for the intralayer kinetics, i.e. we project Eq. (S38) onto $m = m' = 0$. Using $S_{l,0} = 0$ and $C_{l,0} = J_0(|u_l|)$, we obtain the central-harmonic intralayer Dirac Hamiltonian

$$\tilde{h}_{\xi, \text{CH}}^{(l)}(\mathbf{q}) = -\hbar v_F \left[\xi \eta_l q_x \sigma_x^{(l)} + q_y \sigma_y^{(l)} \right], \quad \eta_l \equiv J_0(|u_l|), \quad (\text{S39})$$

which is nonperturbative in the 1D modulation amplitude through η_l .

Control of the central-harmonic projection. The eliminated sectors $m \neq 0$ are separated in energy by $\sim \hbar v_F |m| G_{1D}$. They couple to $m = 0$ through the q_x term in Eq. (S38), with matrix elements $\sim \hbar v_F |q_x|$. Eliminating $m \neq 0$ therefore produces corrections scaling as $(\hbar v_F q_x)^2 / (\hbar v_F G_{1D}) \sim \hbar v_F (q_x^2 / G_{1D})$, i.e. quadratic in momentum. Hence, within a Dirac theory kept to linear order in \mathbf{q} , Eq. (S39) captures the exact $\mathcal{O}(q)$ intralayer kinetics in the unitary-rotated basis.

Supplementary Note S4.3 Dressed interlayer tunnelling in reduced-zone basis, single resonant harmonic \tilde{T}_{0,p_0}^ξ , and leading-order parity rule

The dressed interlayer tunnelling is

$$\tilde{T}_\xi(\mathbf{r}) = \sum_{j=0}^2 \tilde{T}_j^\xi(y) e^{i\mathbf{q}_j^\xi \cdot \mathbf{r}} \quad \left(\tilde{T}_j^\xi(y) = U_2^\dagger(y) T_j^\xi U_1(y) \right), \quad \tilde{T}_j^\xi(y) = \sum_{p \in \mathbb{Z}} \tilde{T}_{j,p}^\xi e^{ip G_{1D} y}. \quad (\text{S40})$$

In resonant configurations, the Dirac–Dirac resonance is governed by the $j = 0$ channel, because $\mathbf{q}_0^\xi = \Delta \mathbf{K}_\xi$ is parallel to \mathbf{G}_{1D} and can therefore be bridged by a single 1D harmonic.

Strip-basis selection rule (resonant $j = 0$ channel). Using $\mathbf{q}_0^\xi = \xi n_{1D} \mathbf{G}_{1D}$ in the resonant geometry, the matrix element of the $j = 0$ channel is

$$\langle \mathbf{q}', m', 2 | \tilde{T}_0^\xi(y) e^{i\mathbf{q}_0^\xi \cdot \mathbf{r}} | \mathbf{q}, m, 1 \rangle = \tilde{T}_{0,p}^\xi \delta_{\mathbf{q}', \mathbf{q}} \delta_{m', m + \xi n_{1D} + p}. \quad (\text{S41})$$

Thus, the two central Dirac cones (the $m = 0$ sectors of layers 1 and 2 at the same reduced momentum \mathbf{q}) are directly coupled only by the single resonant harmonic with $p = -\xi n_{1D} \equiv p_0$,

$$\mathcal{M}^{(n_{1D})} \equiv \tilde{T}_{0,p_0}^\xi = \tilde{T}_{0,p=-\xi n_{1D}}^\xi. \quad (\text{S42})$$

We suppress the valley index ξ in $\mathcal{M}^{(n_{1D})}$, because T_0^ξ and its unitary-transformed counterpart are independent of ξ . Since the parity of p_0 is the same as the parity of n_{1D} , the resonant index n_{1D} directly controls the Pauli content of the resonant coupling.

The Fourier component $\tilde{T}_{0,p}^\xi$ can be written in closed form as

$$\tilde{T}_{0,p}^\xi = \begin{cases} t_0 \left[(c^2 \mathcal{J}_{-,p} + s^2 \mathcal{J}_{+,p}) \mathbb{I} + \mathcal{J}_{+,p} \sigma_x - isc (\mathcal{J}_{-,p} - \mathcal{J}_{+,p}) \sigma_z \right], & p \text{ even,} \\ t_0 \left[s \mathcal{J}_{+,p} (\mathbb{I} + \sigma_x) + c \mathcal{J}_{-,p} \sigma_y + ic \mathcal{J}_{+,p} \sigma_z \right], & p \text{ odd.} \end{cases} \quad (\text{S43})$$

In the $\theta \rightarrow 0$ limit ($c \rightarrow 1, s \rightarrow 0$), Eq. (S43) reduces to the clean parity structure

$$\tilde{T}_{0,p}^\xi \in \begin{cases} \text{span}\{\mathbb{I}, \sigma_x\}, & p \text{ even,} \\ \text{span}\{\sigma_y, \sigma_z\}, & p \text{ odd.} \end{cases} \quad (\text{S44})$$

The terms neglected in Eq. (S44) are proportional to $s = \sin(\theta/2)$, which is parametrically small, $s = \mathcal{O}(\theta)$, for the twist angles of interest in TBG ($\theta \lesssim 5^\circ$), but can become non-negligible at larger twist angles. In the main text, we use Eq. (S44) as the leading organizing principle for the even/odd n_{1D} resonant criterion, and treat the s -dependent admixtures as subleading corrections.

Role of $j = 1, 2$ channels. The $j = 1, 2$ moiré channels carry momenta $\mathbf{q}_{1,2}^\xi$ rotated away from \mathbf{G}_{1D} and do not generate a direct strip-resonant coupling between the two central cones. Their leading effect is to renormalize velocities and dressing factors via remote processes, treated in Sec. S4.4 and validated against full-wave numerics (Sec. S2).

Supplementary Note S4.4 Self-energy correction from remote channels

We neglect intralayer couplings to the $m = \pm 1$ remote intermediate states because the $m \rightarrow m \pm 1$ vertices in the dressed strip Hamiltonian are proportional to q_x . Integrating out these sidebands therefore generates a self-energy $\Sigma_{1D} \sim (\hbar v_F q_x)^2 / (\hbar v_F G_{1D}) = \mathcal{O}(q_x^2)$, which lies beyond the linear Dirac theory considered here.

For the moiré remote channels, all remaining harmonics of \tilde{T}_0 , namely $\tilde{T}_{0,p \neq p_0}$, as well as the $j = 1, 2$ tunnelling \tilde{T}_j^ξ , couple the central cones only to remote intermediate states with a characteristic energy scale $\sim \hbar v_F k \theta$. In the unitary-transformed representation, the exact first-star remote self-energy for the central cones (before any p truncation) is

$$\begin{aligned} \Sigma_{1,M}^{\xi, \text{exact}}(E, \mathbf{q}) &= \sum_{j=0}^2 \sum'_{p \in \mathbb{Z}} (\tilde{T}_{j,p}^\xi)^\dagger \left[E - \tilde{h}_{\xi, \text{CH}}^{(2)}(\mathbf{q} + \mathbf{q}_j^\xi + p \mathbf{G}_{1D}) \right]^{-1} \tilde{T}_{j,p}^\xi, \\ \Sigma_{2,M}^{\xi, \text{exact}}(E, \mathbf{q}) &= \sum_{j=0}^2 \sum'_{p \in \mathbb{Z}} \tilde{T}_{j,p}^\xi \left[E - \tilde{h}_{\xi, \text{CH}}^{(1)}(\mathbf{q} - \mathbf{q}_j^\xi - p \mathbf{G}_{1D}) \right]^{-1} (\tilde{T}_{j,p}^\xi)^\dagger. \end{aligned} \quad (\text{S45})$$

where the prime on the p sum means that the direct resonant channel $p = p_0$ already kept explicitly (Eq. (S42)) is excluded from Σ_M to prevent double counting.

We now make controlled simplifications of Eq. (S45) appropriate for extracting the leading $\mathcal{O}(u_0^2)$ smooth renormalization. In a weak-modulation expansion $U_l(y) = e^{i\alpha_l(y)\sigma_y/2}$ with $\alpha_l = \mathcal{O}(u_l)$ and $\langle \alpha_l \rangle_y = 0$, one has $\tilde{T}_{j,0}^\xi = T_j^\xi + \mathcal{O}(|u_\pm|^2)$, where $T_j^\xi = \mathcal{O}(u_0)$, and $\tilde{T}_{j,p \neq 0}^\xi = \mathcal{O}(|u_\pm|^{|p|})$, while the intermediate-state energy denominators for nonresonant remote channels are always of order $\hbar v_F |\mathbf{q}_j^\xi + p \mathbf{G}_{1D}| \sim p \hbar v_F k \theta$. Therefore, the $p \neq 0$ contribution to Σ_M is suppressed as $\mathcal{O}(u_0^2 |u_\pm|^2)$.

Thus, to leading $\mathcal{O}(u_0^2)$ accuracy we keep only the unit-cell averaged vertex and further approximate it by the bare T_j^ξ .

$$\tilde{T}_j(y) \approx \tilde{T}_{j,0}^\xi = \langle \tilde{T}_j(y) \rangle_y, \quad \tilde{T}_{j,0}^\xi \approx T_j^\xi. \quad (\text{S46})$$

Similarly, we evaluate the remote propagators with the bare Dirac operator, $\tilde{h}_{\xi,\text{CH}}^{(l)} \approx h_\xi^{(l)}$, since $J_0(|u_l|) = 1 + \mathcal{O}(u_l^2)$ implies that the difference to Σ_M is $\mathcal{O}(u_0^2|u_l|^2)$. With these approximations, Eq. (S45) reduces to

$$\begin{aligned} \Sigma_{1,\text{M}}^\xi(E, \mathbf{q}) &= \sum_{j=0}^2 (T_j^\xi)^\dagger \left[E - h_\xi^{(2)}(\mathbf{q} + \mathbf{q}_j^\xi) \right]^{-1} T_j^\xi, \\ \Sigma_{2,\text{M}}^\xi(E, \mathbf{q}) &= \sum_{j=0}^2 T_j^\xi \left[E - h_\xi^{(1)}(\mathbf{q} - \mathbf{q}_j^\xi) \right]^{-1} (T_j^\xi)^\dagger. \end{aligned} \quad (\text{S47})$$

Linearizing Eq. (S47) to first order in (E, \mathbf{q}) gives

$$\Sigma_{l,\text{M}}^\xi(E, \mathbf{q}) \approx \Sigma^{(E)} E + \Sigma_l^{(\mathbf{q})}(\mathbf{q}), \quad \Sigma^{(E)} = -6u_0^2 \mathbb{I}, \quad \Sigma_l^{(\mathbf{q})}(\mathbf{q}) = -3u_0^2 h_\xi^{(l)}(\mathbf{q}). \quad (\text{S48})$$

To incorporate the remote-channel correction in the two-cone problem, one adds the diagonal self-energy blocks to the central-cone Hamiltonian. Keeping only terms linear in (E, \mathbf{q}) , Eq. (S48) implies the following energy-dependent eigenvalue equation:

$$\begin{pmatrix} \tilde{h}_{\xi,\text{CH}}^{(1)}(\mathbf{q}) + \Sigma_1^{(\mathbf{q})}(\mathbf{q}) & (\mathcal{M}^{(n_{1\text{D}})})^\dagger \\ \mathcal{M}^{(n_{1\text{D}})} & \tilde{h}_{\xi,\text{CH}}^{(2)}(\mathbf{q}) + \Sigma_2^{(\mathbf{q})}(\mathbf{q}) \end{pmatrix} \Psi = (1 + 6u_0^2)E \Psi + \mathcal{O}(|\mathbf{q}|^2, u_0^2 E |\mathbf{q}|, u_0^2 E^2). \quad (\text{S49})$$

Thus, the E dependence can be removed by multiplying Eq. (S49) by the quasiparticle weight

$$Z \equiv (\mathbb{I} - \Sigma^{(E)})^{-1} = \frac{1}{1 + 6u_0^2}. \quad (\text{S50})$$

(See Eq. (S51) for the final form.)

Supplementary Note S4.5 Minimal two-cone model and the parity–chirality selection rule on gap-opening channel

Key point. The commensurate $n_{1\text{D}}$ resonance selects a single harmonic of the dressed $j = 0$ moiré tunnelling, p_0 , that directly hybridizes the two central Dirac cones. This determines the Pauli structure of the resonant intercone coupling $Z\mathcal{M}^{(n_{1\text{D}})}$ (to leading order in θ) via the even–odd rule. Whether such a Pauli structure opens an insulating gap depends additionally on the relative chirality of the two interacting cones, which fixes the effective mass channel in the coupled two-cone problem. The minimal theory is used to identify symmetry-allowed gap channels and scaling; the existence of a direct gap throughout the BZ is verified by the fully periodic full-wave numerics (Sec. S2).

Minimal-wave (two-cone) Hamiltonian and the resonant harmonic. Combining the central-harmonic dressed intralayer kinetics Eq. (S39), the resonant harmonic Eq. (S42), and the remote-channel renormalization Eq. (S49), we obtain the renormalized minimal two-cone model

$$H_\xi^{(2\text{c})}(\mathbf{q}) = \begin{pmatrix} -\hbar(\xi v_x^{(1)} q_x \sigma_x^{(1)} + v_y^{(1)} q_y \sigma_y^{(1)}) & (Z\mathcal{M}^{(n_{1\text{D}})})^\dagger \\ Z\mathcal{M}^{(n_{1\text{D}})} & -\hbar(\xi v_x^{(2)} q_x \sigma_x^{(2)} + v_y^{(2)} q_y \sigma_y^{(2)}) \end{pmatrix}, \quad (\text{S51})$$

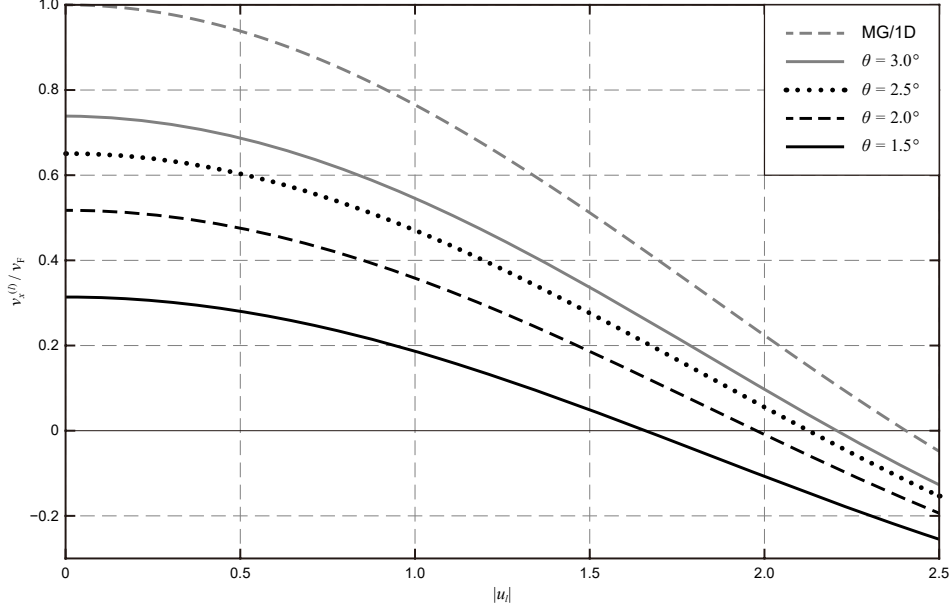


Figure S3: Renormalized band velocity along the direction perpendicular to \mathbf{G}_{1D} , $v_x^{(l)}$, of TBG-1D with θ from 1.5° to 3.0° plotted against $|u_l|$. Gray dashed line (MG/1D) shows the renormalized velocity of monolayer graphene under a unidirectional potential for reference. The unidirectional potential causes $v_x^{(l)}$ to change sign as $|u_l|$ increases. The value of $|u_l|$ at which $v_x^{(l)} = 0$ decreases as θ decreases, reflecting the intrinsic velocity renormalization of TBG.

with

$$v_x^{(l)} \equiv Z v_F (\eta_l - 3u_0^2), \quad v_y^{(l)} \equiv Z v_F (1 - 3u_0^2), \quad (\text{S52})$$

where $\eta_l = J_0(|u_l|)$. This 4×4 Hamiltonian is Hermitian by construction and captures the symmetry-dictated Pauli structure of the resonance.

Pauli decomposition and the parity (even-odd n_{1D}) resonant rule. We write the resonant coupling as

$$Z\mathcal{M}^{(n_{1D})} = m_0 \mathbb{I} + m_x \sigma_x + m_y \sigma_y + m_z \sigma_z, \quad (\text{S53})$$

with the coefficients m_μ determined by Eqs. (S42) and (S43). To leading order in θ , the parity rule implies that

$$\lim_{\theta \rightarrow 0} Z\mathcal{M}^{(n_{1D})} \approx \begin{cases} Zt_0 [\mathcal{J}_{-,p_0} \mathbb{I} + \mathcal{J}_{+,p_0} \sigma_x], & p_0 (= -\xi n_{1D}) \text{ even,} \\ Zt_0 [\mathcal{J}_{-,p_0} \sigma_y + i \mathcal{J}_{+,p_0} \sigma_z], & p_0 (= -\xi n_{1D}) \text{ odd,} \end{cases} \quad (\text{S54})$$

in the leading $\theta \rightarrow 0$ limit.

Relative chirality and the gap-opening channel. A gap in a Dirac system requires a mass term that anticommutes with the kinetic Dirac matrices (see, e.g., Ref.⁹). Gap opening in a coupled two-Dirac-cone problem depends on both the Pauli content in Eq. (S53) and the relative chirality of the two cones. Allowing the two cones to carry valley indices ξ_1 (layer 1) and ξ_2 (layer 2), and assuming $v_y^{(l)} > 0$, we define relative chirality as

$$\chi_{\text{rel}} \equiv \xi_1 \xi_2 \text{sgn}(v_x^{(1)} v_x^{(2)}). \quad (\text{S55})$$

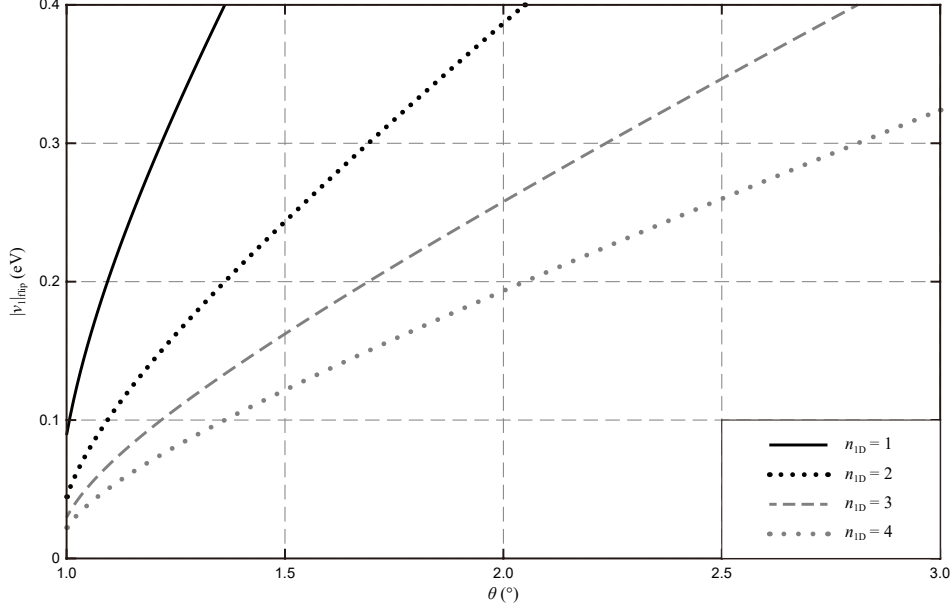


Figure S4: Modulation amplitude $|v_1|$ (in eV) at which the transverse velocity $v_x^{(1)}$ first changes sign, determined by $J_0(|u_1|) - 3u_0^2 = 0$, as a function of twist angle θ for four resonance orders $n_{1D} = 1, 2, 3, 4$. Exceeding this threshold at fixed $|v_2|$ (layer-asymmetric modulation) reverses χ_{rel} and switches the gap-opening channel (see Eq. (S57) and Fig. 3a).

For the valley-conserving resonant configurations treated in this work, $\xi_1 = \xi_2 = \xi$ and hence $\chi_{\text{rel}} = \text{sgn}(v_x^{(1)} v_x^{(2)})$. As Fig. S3 shows, $v_x^{(l)}$ (Eq. (S52)) of TBG-1D inverts its sign as $|u_l|$ increases and makes $J_0(|u_l|) - 3u_0^2$ negative. While monolayer graphene under a unidirectional potential also exhibits similar anisotropic band renormalization (gray dashed line in Fig. S3)^{7;8;10}, TBG-1D exhibits the sign inversion at much weaker $|u_l|$ because of the intrinsic band velocity renormalization by TBG (i.e., the $-3u_0^2$ term). Accordingly, the value of $|u_l|$ at which $v_x^{(l)}$ changes sign decreases as θ decreases, that is, as u_0 increases. Figure S4 shows the corresponding modulation amplitude $|v_1|$ (with $u_1 = v_1/(\hbar v_F G_{1D})$) that produces the first sign change of $v_x^{(1)}$ as a function of θ for $n_{1D} = 1-4$. Exceeding this threshold at fixed $|v_2|$ (layer-asymmetric modulation) reverses χ_{rel} and switches the gap-opening channel (see Eq. (S57) and Fig. 3a). For example, if $|v_2|$ is kept weak while $|v_1|$ exceeds this threshold, the dominant gap-opening channel switches from σ_z to σ_x . Accordingly, the even/odd parity rule is reversed: odd n_{1D} resonances become gapless, whereas even n_{1D} resonances open a gap, consistent with Eq. (S54).

In the weak-to-moderate modulation regime relevant to the main text, or in the layer-symmetric modulation ($|u_1| \approx |u_2|$), $v_x^{(1)} v_x^{(2)} > 0$ and therefore $\chi_{\text{rel}} = +1$. By contrast, a strongly layer-asymmetric modulation can invert the sign of one transverse velocity (i.e., $v_x^{(1)} v_x^{(2)} < 0$, Fig. 3b), realizing $\chi_{\text{rel}} = -1$.

For $\chi_{\text{rel}} = +1$ (same chirality), a σ_z component in $Z\mathcal{M}^{(n_{1D})}$ provides the distinguished mass channel, whereas $\sigma_{x,y}$ primarily shift/split Dirac nodes and can generate charge-neutral pockets. For $\chi_{\text{rel}} = -1$ (opposite chirality), the chiralities can be aligned by a constant sublattice rotation on one cone, e.g.

$$W = \sigma_y, \quad W^\dagger \sigma_x W = -\sigma_x, \quad W^\dagger \sigma_y W = \sigma_y. \quad (\text{S56})$$

However, the alignment reshuffles the Pauli components of $Z\mathcal{M}^{(n_{1D})} = m_0\mathbb{I} + m_x\sigma_x + m_y\sigma_y + m_z\sigma_z$

as

$$Z\mathcal{M}^{(n_{1D})} \rightarrow Z\mathcal{M}_{\text{align}}^{(n_{1D})} \equiv Z\mathcal{M}^{(n_{1D})}W = m_0\sigma_y + im_x\sigma_z + m_y\mathbb{I} - im_z\sigma_x. \quad (\text{S57})$$

Thus, in an opposite-chirality two-cone problem, the σ_x term in the original expression (Eq. (S51)) serves as an effective gap-opening mass (i.e., σ_z -like) channel in the chirality-aligned expression. Therefore, the relative chirality rule implies that

$$\text{gap-opening (mass) channel} = \begin{cases} \sigma_z, & \chi_{\text{rel}} = +1, \\ \sigma_x, & \chi_{\text{rel}} = -1. \end{cases} \quad (\text{S58})$$

Note that, for any general, isolated, non-interacting Dirac cone, the sign of $v_x^{(l)}$ is not physical: it can be flipped by a constant sublattice rotation, Eq. (S56). Only in a coupled Dirac cone system, the sign of $v_x^{(l)}$ has a physical meaning: applying such a rotation to only one cone also transforms the intercone coupling, $Z\mathcal{M}^{(n_{1D})} \rightarrow Z\mathcal{M}^{(n_{1D})}W$, and therefore reshuffles Pauli components (Eq. (S57)). But, if both $v_x^{(1)}$ and $v_x^{(2)}$ change their signs (which keeps $\chi_{\text{rel}} = +1$), the intercone coupling merely changes the sign of its Pauli components, $Z\mathcal{M}^{(n_{1D})} \rightarrow WZ\mathcal{M}^{(n_{1D})}W = m_0\mathbb{I} - m_x\sigma_x + m_y\sigma_y - m_z\sigma_z$, even in a coupled Dirac cone system. Consequently, the physically meaningful quantity in a coupled system is also the relative sign, $\text{sgn}(v_x^{(1)}v_x^{(2)})$, or equivalently the relative chirality χ_{rel} in Eq. (S55).

We plot the magnitudes of the normalized Pauli components $|m_\mu|/(Zt_0)$ ($\mu = 0, x, y, z$) of the inter-cone coupling $Z\mathcal{M}^{(n_{1D})}$ (Eq. (S53)) for TBG-1D with $\theta = 3^\circ$ in Fig. S5. Each line represents $n_{1D} = 1$ to 4, respectively. In this plot, we chose the layer-dependent 1D modulation with a slightly asymmetric amplitude between layers ($u_2 = 0.8u_1$), to show the contribution from $\mathcal{J}_{-,p}$ (m_0 for even p and m_y for odd p , Eq. (S43)), while keeping a common phase, $\phi_1 = \phi_2$. The gap-opening channel for $\chi_{\text{rel}} = +1$ (same chirality), m_z (Eq. (S58)), becomes substantial in TBG-1D when n_{1D} is odd, whereas the gap-opening channel for $\chi_{\text{rel}} = -1$ (opposite chirality), m_x , becomes sizable when n_{1D} is even, following the n_{1D} -parity rule Eq. (S54). By contrast, the node-shifting channels m_0 and m_y remain comparatively small.

(i) For $\chi_{\text{rel}} = +1$ (same chirality): For the same Dirac-cone chirality, σ_z is the gap-opening channel (Eq. (S58)).

In a TBG-1D with an odd n_{1D} , $Z\mathcal{M}^{(n_{1D})} \approx m_y\sigma_y + im_z\sigma_z$: as Fig. S5 shows, a gap-opening mass channel is generically present unless $m_z(\propto J_{p_0}(|u_+|/2)) = 0$ accidentally. Therefore, for $\chi_{\text{rel}} = +1$ the odd- n_{1D} resonant configurations can open a local direct gap $\Delta_{\mathbf{q}=\mathbf{0}} \approx 2|m_z|$ at $\mathbf{q} = \mathbf{0}$ when $|m_z| \gtrsim |m_y|$ (see Sec. S4.7 for the relative magnitude).

If n_{1D} is even, the coupling $Z\mathcal{M}^{(n_{1D})} \in \text{span}\{\mathbb{I}, \sigma_x\}$ contains no leading σ_z mass channel and generically produces Dirac-node splitting and/or charge-neutral pockets rather than a direct gap.

(ii) For $\chi_{\text{rel}} = -1$ (opposite chirality): For the opposite Dirac-cone chirality, σ_x is the gap-opening channel. TBG-1D with an even n_{1D} has a sizable σ_x channel (Fig. S5b), thus can open a direct gap, while that with an odd n_{1D} cannot (Eq. (S54)). In other words, the intercone coupling $Z\mathcal{M}^{(n_{1D})} = m_0\mathbb{I} + m_x\sigma_x$ for even n_{1D} acquires an effective σ_z component in the chirality-aligned basis, $m_0\sigma_y + m_x\sigma_z$, and can therefore open a gap.

An opposite-valley pair ($\xi_1 = -\xi_2$), by a short-wavelength unidirectional superlattice, also yields $\chi_{\text{rel}} = -1$ even when $v_x^{(1)}v_x^{(2)} > 0$, providing an alternative route to the opposite-chirality two-cone problem without tuning through a flattening point.

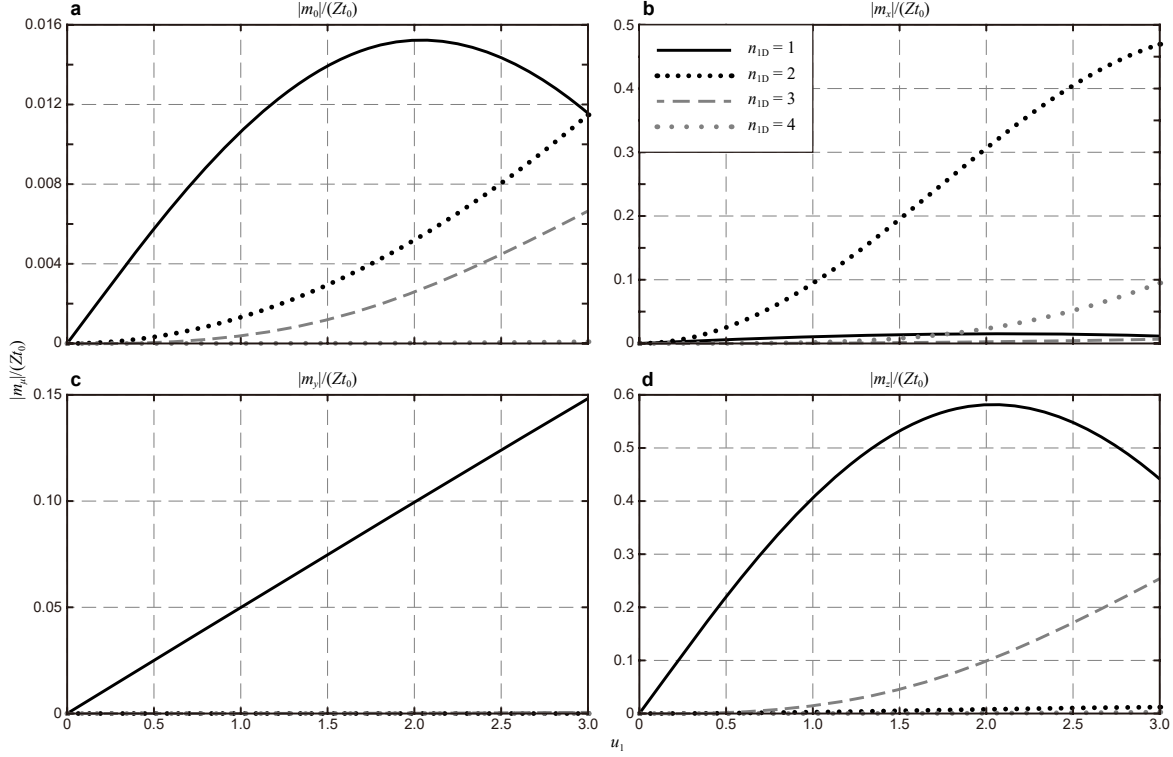


Figure S5: Pauli channels **a** $|m_0|$, **b** $|m_x|$, **c** $|m_y|$, **d** $|m_z|$ (normalized by Zt_0) of the effective resonant inter-cone coupling $Z\mathcal{M}^{(n_{1D})}$ (Eq. (S53)) in TBG–1D with $\theta = 3^\circ$ plotted against u_1 . Each line corresponds to $n_{1D} = 1, 2, 3, 4$. The layer-dependent 1D modulation is taken to have a slightly asymmetric amplitude between layers, with $u_2 = 0.8u_1$, while keeping a common phase, $\phi_1 = \phi_2$. The gap-opening channel for $\chi_{\text{rel}} = +1$ (same chirality), m_z (Eq. (S58)), becomes substantial in TBG–1D when n_{1D} is odd, whereas the gap-opening channel for $\chi_{\text{rel}} = -1$ (opposite chirality), m_x , becomes sizable when n_{1D} is even, resulting in the n_{1D} -parity rule Eq. (S54). By contrast, the node-shifting channels m_0 and m_y remain comparatively small.

Supplementary Note S4.6 Rank structure of rigid interlayer tunneling and why Moiré–1D can open a Dirac gap

In the rigid-lattice continuum model for pristine TBG, all the interlayer tunneling T_j^ξ ($j = 0, 1, 2$) is rank-one because

$$\det T_j^\xi = t_0^2 \left(1 - \omega^{-\xi j} \omega^{\xi j}\right) = 0, \quad (\text{S59})$$

and can be viewed as a projector in the sublattice space. Consequently, if a low-energy Dirac–Dirac resonance is governed by a single bare harmonic T_j^ξ —including the unique case where the Dirac-point mismatch is exactly compensated so that the two cones meet at the same reduced momentum, such as double-walled carbon nanotubes¹¹)—the 4×4 Hamiltonian at the Dirac point has the form

$$H(0) = \begin{pmatrix} 0 & (T_j^\xi)^\dagger \\ T_j^\xi & 0 \end{pmatrix}, \quad (\text{S60})$$

whose spectrum contains two zero modes whenever $\text{rank}(T_j^\xi) = 1$. Therefore, a rank-one intercone coupling cannot open a full gap at the Dirac crossing; the spectrum remains nodal (Dirac or semi-

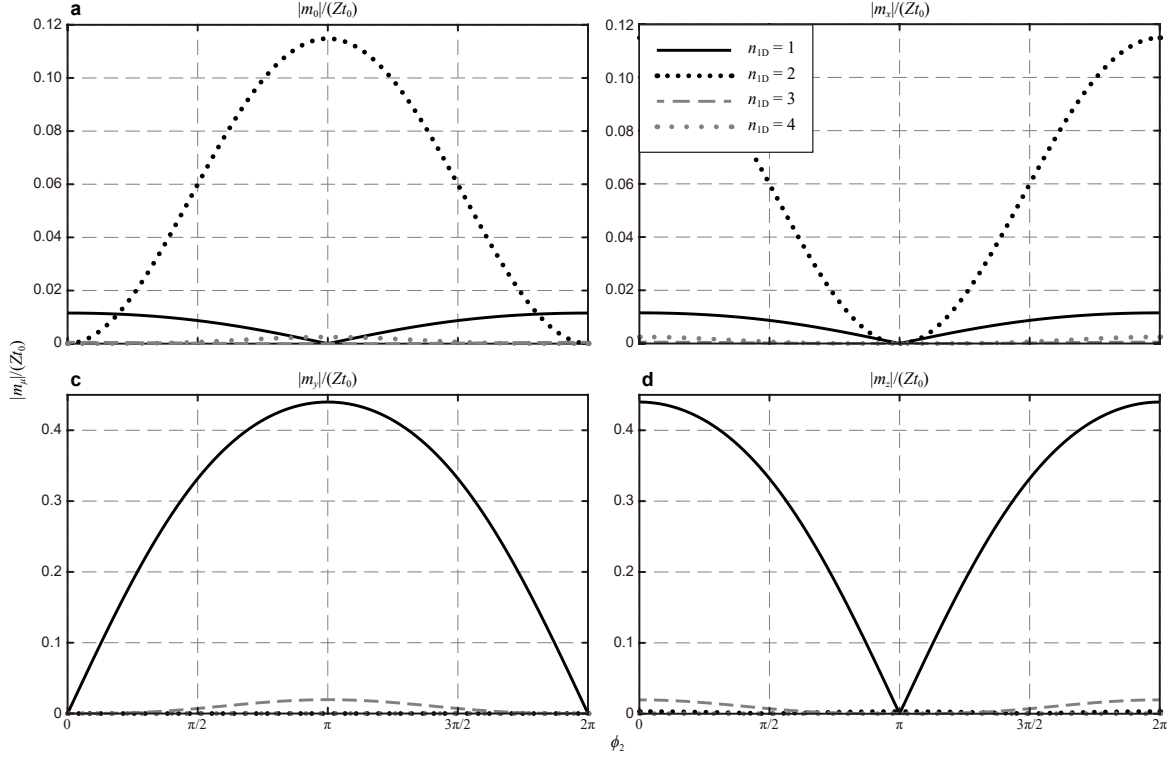


Figure S6: Plot similar to Fig. S5, but plotted against ϕ_2 , while using $|u_1| = |u_2| = 1$, $\phi_1 = 0$, $\theta = 3^\circ$, to show the effects of a layer-asymmetric phase of the 1D modulation. The gap-opening channel for either chirality χ_{rel} is maximized when the two modulations are in-phase ($\phi_2 - \phi_1 \equiv 0 \pmod{2\pi}$) and vanishes when they are out-of-phase ($\phi_2 - \phi_1 \equiv \pi \pmod{2\pi}$).

Dirac depending on the relative chirality and detuning).

Lattice relaxation modifies the tunneling by distinguishing AA and AB/BA amplitudes. In the simplest parametrization,

$$T_j^\xi = \begin{pmatrix} u_{AA} & u_{AB} \omega^{-\xi j} \\ u_{AB} \omega^{\xi j} & u_{AA} \end{pmatrix}, \quad \det T_j^\xi = u_{AA}^2 - u_{AB}^2. \quad (\text{S61})$$

Thus, the strict rank-one constraint is lifted when $u_{AA} \neq u_{AB}$. In pristine TBG, however, additional symmetries (notably $C_2\mathcal{T}$ in a single-valley description) can still protect gapless Dirac points at charge neutrality, so relaxation alone does not necessarily guarantee a Dirac gap.

In the moiré-1D problem studied in this work, a unidirectional scalar potential dresses the tunneling by a layer-dependent unitary transformation $U_l(y)$, as

$$\tilde{T}_j^\xi(y) = U_2^\dagger(y) T_j^\xi U_1(y), \quad \tilde{T}_{j,p}^\xi = \frac{G_{1D}}{2\pi} \int_0^{2\pi/G_{1D}} \tilde{T}_j^\xi(y) e^{-ipG_{1D}y} dy. \quad (\text{S62})$$

While $\tilde{T}_j^\xi(y)$ preserves the instantaneous rank of T_j^ξ at each real-space point, the Fourier component $\tilde{T}_{j,p}^\xi$ relevant for a Dirac-Dirac resonance is a coherent sum of inequivalent rank-one projectors whose orientation varies with y . As a result, $\tilde{T}_{j,p}^\xi$ is generically full rank. For example, for even p and small twist angle one typically obtains

$$\tilde{T}_{0,p}^\xi \approx t_0 (\mathcal{J}_{-,p} \mathbb{I} + \mathcal{J}_{+,p} \sigma_x), \quad \mathcal{J}_{\pm,p} = J_p (|u_{\pm}|/2) e^{ip\phi_{\pm}}, \quad (\text{S63})$$

so that

$$\det \tilde{T}_{0,p}^\xi \approx t_0^2 (\mathcal{J}_{-,p}^2 - \mathcal{J}_{+,p}^2), \quad (\text{S64})$$

which is nonzero unless $|\mathcal{J}_{-,p}| = |\mathcal{J}_{+,p}|$ accidentally. Therefore, moiré-1D dressing provides a natural route to generate a full-rank intercone coupling, and, together with the appropriate relative chirality, enables a Dirac gap even when the bare rigid-lattice T_j^ξ are rank-one.

Supplementary Note S4.7 Layer-symmetric component of the 1D modulation and the resonant gap scale

For both chirality classes ($\chi_{\text{rel}} = +1$, where the leading gapped resonances are odd $n_{1\text{D}}$ with the σ_z mass channel, and $\chi_{\text{rel}} = -1$, where the leading gapped resonances are even $n_{1\text{D}}$ with the σ_x mass channel), the magnitude of the gap-opening channel for the $n_{1\text{D}}$ Dirac-Dirac resonance scales as

$$|m_\mu| \propto |J_{|n_{1\text{D}}|}(|u_+|)|, \quad (\text{S65})$$

while the node-shifting term scales as $|J_{|n_{1\text{D}}|}(|u_-|)|$. Thus, the magnitude of the CNP direct gap is controlled by the layer-symmetric component of the 1D modulation,

$$u_+ \equiv \frac{1}{2}(|u_1|e^{i\phi_1} + |u_2|e^{i\phi_2}), \quad |u_+| = \frac{1}{2}\sqrt{|u_1|^2 + |u_2|^2 + 2|u_1||u_2|\cos(\phi_1 - \phi_2)}, \quad (\text{S66})$$

while the node-shifting effect is controlled by the out-of-phase component $u_- \equiv (|u_1|e^{i\phi_1} - |u_2|e^{i\phi_2})/2$. Figure S6 shows that the gap is maximized and the node-shifting term is minimized when the two layer modulations are in phase ($\phi_1 = \phi_2$), for which $|u_+| = (u_1 + u_2)/2$. Conversely, the gap-opening channel is suppressed when the modulations are out of phase ($\phi_1 - \phi_2 = \pi$), for which $|u_+| = |u_1 - u_2|/2$; in particular, for the layer-symmetric case $u_1 = u_2$ the cancellation is exact and the gap-opening channel vanishes at leading order.

An equivalent viewpoint is that the resonant dressed tunnelling component \tilde{T}_{0,p_0}^ξ collects coherent contributions where the required momentum transfer $p_0\mathbf{G}_{1\text{D}}$ is generated before or after interlayer tunnelling, or even by their convolution, through the dressing factors U_1 and U_2^\dagger . As a result, the relative gate phase $\phi_1 - \phi_2$ controls constructive/destructive interference in the effective resonant coupling.

For the modulation strengths used in most of this work, $|u_+|$ lies on the first rising lobe of the Bessel function (i.e., below the first maximum of $|J_{|n_{1\text{D}}|}(x)|$), so increasing $|u_+|$ monotonically enhances the gap-opening channel and hence the achievable Δ_{dir} in the near-resonant gapped regime.

Supplementary Note S4.8 Scaling of the resonant coupling with $|n_{1\text{D}}|$

For a general resonant index $n_{1\text{D}}$, the direct intercone coupling is controlled by the single harmonic $p_0 = -\xi n_{1\text{D}}$ of Eq. (S43). For both even and odd $n_{1\text{D}}$, the magnitude of $\mathcal{M}^{(n_{1\text{D}})}$ varies with the order $|p_0| (= |n_{1\text{D}}|)$ Bessel functions. This implies the rapid suppression of the potential gap-opening term in $\mathcal{M}^{(n_{1\text{D}})}$, $t_0|J_{|n_{1\text{D}}|}(|u_+/2|)|$ in both (i) odd $n_{1\text{D}}$ with $\chi_{\text{rel}} = +1$ and (ii) even $n_{1\text{D}}$ with $\chi_{\text{rel}} = -1$, as $n_{1\text{D}}$ increases, $t_0|J_{|n_{1\text{D}}|}(|u_+/2|)| \approx t_0(|u_+/4|)^{|n_{1\text{D}}|}/(|n_{1\text{D}}|!)$ for weak modulation $|u_+| \ll 1$ (Fig. S5).

Supplementary Note S4.9 Weak-1D limit ($|u_l| \ll 1$): expansions for velocities and \mathcal{M}

In the weak-modulation regime $|u_l| \ll 1$, Bessel functions satisfy

$$J_0(|u_l|) \approx 1 - \frac{|u_l|^2}{4} + \mathcal{O}(|u_l|^4), \quad J_1\left(\frac{|u_{\pm}|}{2}\right) \approx \frac{|u_{\pm}|}{4} + \mathcal{O}(|u_{\pm}|^3). \quad (\text{S67})$$

Using $\eta_l = J_0(|u_l|)$ and $Z = 1/(1 + 6u_0^2)$, the renormalized velocities in Eq. (S52) become

$$v_x^{(l)} \approx \frac{v_F}{1 + 6u_0^2} \left(1 - 3u_0^2 - \frac{|u_l|^2}{4}\right), \quad v_y^{(l)} \approx \frac{v_F}{1 + 6u_0^2} (1 - 3u_0^2), \quad (\text{S68})$$

up to $\mathcal{O}(|u_l|^4)$ corrections. For $n_{1D} = 1$ (hence $p_0 = -\xi$), Eq. (S54) yields

$$Z\mathcal{M}^{(n_{1D})} \approx -\xi \frac{Zt_0}{4} \left[|u_-| e^{-i\xi\phi_-} \sigma_y + i |u_+| e^{-i\xi\phi_+} \sigma_z \right] \quad (|u_l| \ll 1). \quad (\text{S69})$$

Equations (S68)–(S69) provide compact checkable limits: $v_x^{(l)}$ is reduced at $\mathcal{O}(|u_l|^2)$ through $J_0(|u_l|)$ (Fig. S3), while the direct resonant hybridization scales linearly in $|u_{\pm}|$ through $J_1(|u_{\pm}|/2)$ (Figs. S5b and S5d).

Supplementary Note S4.10 Validity and limitations

We summarize the controlled approximations used in Sec. S4.5 and their validity windows:

Linearization in reduced momentum. We expand near CNP to first order in \mathbf{q} and neglect $\mathcal{O}(|\mathbf{q}|^2)$.

Central-harmonic projection (intralayer). Eliminating $m \neq 0$ sectors in Eq. (S38) produces corrections of order $\mathcal{O}(\hbar v_F q_x^2 / G_{1D})$, beyond the linear Dirac theory. Within the $m = 0$ sector, the unidirectional scalar potential is incorporated nonperturbatively through $\eta_l = J_0(|u_l|)$ in Eq. (S39).

Minimal-wave truncation (interlayer). We retain only the two central cones and the single resonant harmonic $\mathcal{M}^{(n_{1D})} = \tilde{T}_{0,p_0}^{\xi}$ with $p_0 = -\xi n_{1D}$. All remaining moiré channels enter as a smooth $\mathcal{O}(u_0^2)$ self-energy, incorporated at leading order through Z and the velocity renormalization recipe in Eqs. (S47)–(S52).

Caveat near flattening. When $\eta_l \approx 3u_0^2$, the nominally subleading $\mathcal{O}(q_x^2 / G_{1D})$ correction can compete with the linear term; the strictly linear description then requires $|q_x| \ll Z|\eta_l - 3u_0^2| G_{1D}$.

Supplementary Note S5 Near resonance: gapped arcs from a de-tuned two-cone model

Exact Dirac–Dirac momentum resonance requires $\Delta\mathbf{K}_{\xi} = \xi n_{1D} \mathbf{G}_{1D}$ (Eq. (S4)), which is a measure-zero condition in the two-dimensional design space of \mathbf{G}_{1D} . In realistic devices, \mathbf{G}_{1D} typically lies in a near-resonant neighborhood of this point but does not coincide with it. Here we show that the renormalized two-cone theory developed for the resonant case (Eq. (S51)) naturally extends to this near-resonant regime upon introducing a small momentum-mismatch vector. The resulting analytic criterion explains why, in a fixed- $\Delta\mathbf{K}_{\xi}$ configuration map that scans \mathbf{G}_{1D} (Fig. S7b), the region which shows the gapped configuration appears as a thick arc whose ridge is not centered at the exact resonant point $\mathbf{G}_{1D} = \xi \Delta\mathbf{K}_{\xi} / n_{1D}$.

Throughout we focus on the same-chirality regime $\chi_{\text{rel}} = +1$ (Supplementary Note S4.6), where the σ_z component of the intercone coupling provides the leading mass (gap-opening) channel. All

parameters below include the leading remote-moiré self-energy through the quasiparticle weight Z and the renormalized velocities $v_{x/y}^{(l)}$ (Eq. (S52)).

Supplementary Note S5.1 Momentum mismatch and momentum-mismatched two-cone Hamiltonian

Momentum mismatch. For near-resonant configurations we use the momentum-mismatch vector defined in Eq. (S6),

$$\delta\mathbf{q}_\xi \equiv \Delta\mathbf{K}_\xi - \xi n_{1D}\mathbf{G}_{1D}. \quad (\text{S70})$$

Let $\hat{\mathbf{n}} \equiv \mathbf{G}_{1D}/G_{1D}$ be the 1D modulation direction and $\hat{\mathbf{n}}_\perp$ its perpendicular unit vector,

$$\hat{\mathbf{n}} = (n_x, n_y), \quad \hat{\mathbf{n}}_\perp \equiv (-n_y, n_x). \quad (\text{S71})$$

We decompose the mismatch as

$$\delta q_\parallel \equiv \delta\mathbf{q}_\xi \cdot \hat{\mathbf{n}}, \quad \delta q_\perp \equiv \delta\mathbf{q}_\xi \cdot \hat{\mathbf{n}}_\perp, \quad \delta\mathbf{q}_\xi = \delta q_\perp \hat{\mathbf{n}}_\perp + \delta q_\parallel \hat{\mathbf{n}}. \quad (\text{S72})$$

Coordinates adapted to the 1D modulation. To avoid mixing different coordinate conventions, in this section we express the two-cone model in the $(\hat{\mathbf{n}}_\perp, \hat{\mathbf{n}})$ -adapted components of momentum:

$$q_\perp \equiv \mathbf{q} \cdot \hat{\mathbf{n}}_\perp, \quad q_\parallel \equiv \mathbf{q} \cdot \hat{\mathbf{n}}. \quad (\text{S73})$$

Equivalently, if $\mathbf{q} = (q_x, q_y)$ in the fixed lab-frame $(\hat{\mathbf{x}}, \hat{\mathbf{y}})$, $q_\perp = -n_y q_x + n_x q_y$, $q_\parallel = n_x q_x + n_y q_y$, and the same relations hold for $\delta\mathbf{q}_\xi$.

Local Pauli matrices. We also define Pauli matrices associated with $(\hat{\mathbf{n}}, \hat{\mathbf{n}}_\perp)$ in each layer,

$$\sigma_\perp^{(l)} \equiv -n_y \sigma_x^{(l)} + n_x \sigma_y^{(l)}, \quad \sigma_\parallel^{(l)} \equiv n_x \sigma_x^{(l)} + n_y \sigma_y^{(l)}. \quad (\text{S74})$$

They satisfy the same Pauli algebra and reduce to the standard form used in Eq. (S51) at the commensurate resonance of the symmetric-rotation geometry, where $\hat{\mathbf{n}} = \hat{\mathbf{y}}$. (In that case $q_\parallel = q_y$, $\sigma_\parallel^{(l)} = \sigma_y^{(l)}$, and $q_\perp \sigma_\perp^{(l)} = q_x \sigma_x^{(l)}$.)

Momentum-mismatched two-cone Hamiltonian. At exact resonance ($\delta\mathbf{q}_\xi = \mathbf{0}$), the low-energy spectrum near charge neutrality is captured by the renormalized two-cone model $H_\xi^{(2c)}(\mathbf{q})$ in Eq. (S51). In the near-resonant regime, the same resonant harmonic still provides the dominant intercone hybridization, but it transfers the residual momentum $\delta\mathbf{q}_\xi$. It is therefore convenient to represent the two cones as displaced by $\pm\delta\mathbf{q}_\xi/2$, giving

$$H_\xi^{(2c)}(\mathbf{q}; \delta\mathbf{q}_\xi) = \begin{pmatrix} h_\xi^{(1)}(\mathbf{q}; -\delta\mathbf{q}_\xi/2) & (Z\mathcal{M}^{(n_{1D})})^\dagger \\ Z\mathcal{M}^{(n_{1D})} & h_\xi^{(2)}(\mathbf{q}; +\delta\mathbf{q}_\xi/2) \end{pmatrix}, \quad (\text{S75})$$

with the anisotropic Dirac blocks

$$h_\xi^{(l)}(\mathbf{q}; \delta\mathbf{q}_\xi) = -\hbar(\xi v_x^{(l)} (q_\perp + \delta q_\perp) \sigma_\perp^{(l)} + v_y^{(l)} (q_\parallel + \delta q_\parallel) \sigma_\parallel^{(l)}). \quad (\text{S76})$$

Here $(v_\perp^{(l)}, v_\parallel^{(l)})$ are given by Eq. (S52) (transverse/longitudinal velocities with respect to the 1D modulation direction), and $Z\mathcal{M}^{(n_{1D})}$ is decomposed into Pauli channels as in Eq. (S53). Equation (S75) shows that the momentum-mismatch $\delta\mathbf{q}_\xi$ works as an axial gauge-like vector potential which shifts the two interacting Dirac cones in the momentum-space. Equation (S75) reduces to the commensurate two-cone model when $\delta\mathbf{q}_\xi = \mathbf{0}$.

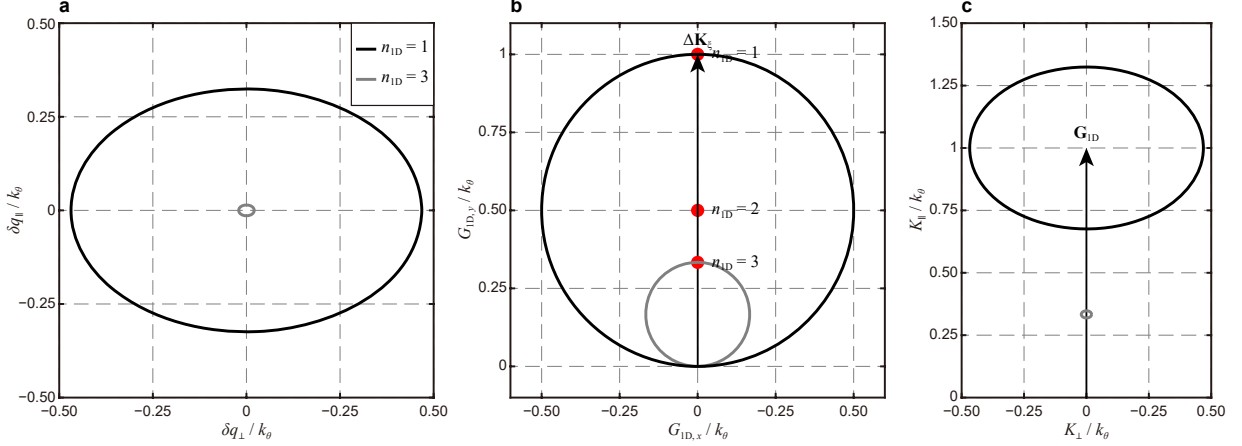


Figure S7: Tolerance in **a** the momentum-mismatch $\delta\mathbf{q}_\xi$ (Eq. (S80)), **b** \mathbf{G}_{1D} at fixed- $\Delta\mathbf{K}_\xi$ (Eq. (S84), Fig. 1b), **c** $\Delta\mathbf{K}_\xi$ at fixed- \mathbf{G}_{1D} (Eq. (S85)) for opening a CNP gap in near-resonant configurations of TBG-1D with $\theta = 3^\circ$ and $u_1 = u_2 = 1$, axes are plotted in units of $k_\theta = |\Delta\mathbf{K}_\xi|$. Black (gray) line shows the tolerance for the $n_{1D} = 1$ ($n_{1D} = 3$) configuration. Red dots in **b** indicate the points where \mathbf{G}_{1D} equals 1, 1/2, and 1/3; these correspond to the $n_{1D} = 1, 2, 3$ resonant configurations. A gap opens within the ellipse in **a** and **c**, while it opens along the circle (arc) in **b** due to the non-linear mapping between $\delta\mathbf{q}_\xi$ and \mathbf{G}_{1D} .

Supplementary Note S5.2 Gapped region in momentum-mismatch space $\delta\mathbf{q}_\xi$: filled ellipse

Mismatch energy scale. Define the effective velocities

$$v_\perp^{\text{eff}} \equiv \sqrt{v_\perp^{(1)} v_\perp^{(2)}}, \quad v_\parallel^{\text{eff}} \equiv \sqrt{v_\parallel^{(1)} v_\parallel^{(2)}}, \quad (\text{S77})$$

and the corresponding mismatch energy scale

$$\varepsilon_{\text{mm}}(\delta\mathbf{q}_\xi) \equiv \frac{\hbar}{2} \sqrt{(v_\perp^{\text{eff}} \delta q_\perp)^2 + (v_\parallel^{\text{eff}} \delta q_\parallel)^2}. \quad (\text{S78})$$

Gap estimate and ellipse inequality. When $\chi_{\text{rel}} = +1$ and $m_z \sigma_z$ is the leading mass channel, diagonalizing Eq. (S75) gives the estimate

$$\Delta_{\text{dir}}^{(2c)}(\delta\mathbf{q}_\xi) \approx 2 \max(|m_z| - \varepsilon_{\text{mm}}(\delta\mathbf{q}_\xi), 0), \quad (\text{S79})$$

which is exact when $v_\perp^{(1)} = v_\perp^{(2)}$ and $v_\parallel^{(1)} = v_\parallel^{(2)}$ and $m_x = m_y = 0$. A necessary condition for a finite gap in Eq. (S79) is

$$\frac{\delta q_\perp^2}{Q_\perp^2} + \frac{\delta q_\parallel^2}{Q_\parallel^2} < 1, \quad Q_\perp \equiv \frac{2|m_z|}{\hbar v_\perp^{\text{eff}}}, \quad Q_\parallel \equiv \frac{2|m_z|}{\hbar v_\parallel^{\text{eff}}}. \quad (\text{S80})$$

i.e., the gapped region in the mismatch coordinates $(\delta q_\perp, \delta q_\parallel)$ is a filled ellipse centered at $\delta\mathbf{q}_\xi = \mathbf{0}$, as Fig. S7a shows.

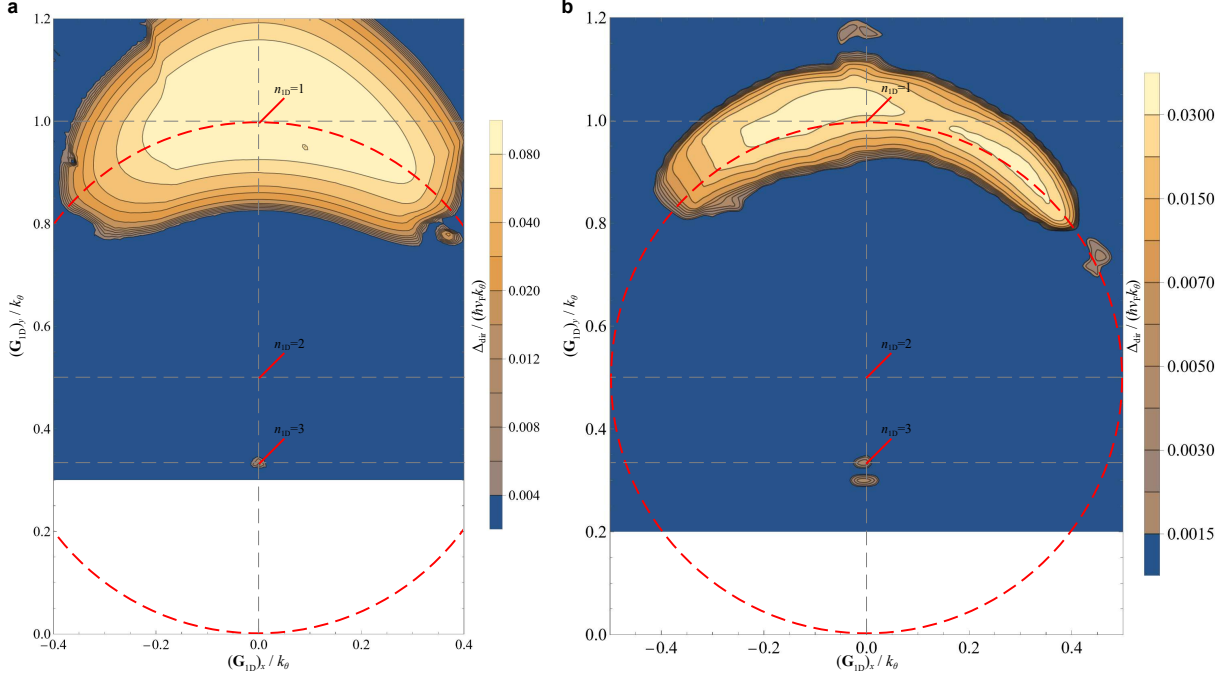


Figure S8: Plot similar to Fig. 1b (full-wave continuum map of the charge-neutrality direct gap Δ_{dir} (in units of $\hbar v_F k_\theta$, log-scale) versus \mathbf{G}_{1D} for a layer-symmetric (in-phase) modulation ($|u_1| = |u_2| = 1$ and $\phi_1 = \phi_2 = 0$)), for **a** $\theta = 3^\circ$ and **b** 5° . Resonance markers indicate Dirac–Dirac matching for $n_{1D} = 1, 2, 3$, while the red-dashed ridge circle highlights the near-resonant gapped arc around the $n_{1D} = 1$ resonance. This map corresponds to the default chirality class ($\chi_{\text{rel}} = +1$) of the layer-symmetric slice.

Supplementary Note S5.3 Gapped region in (fixed- $\Delta\mathbf{K}_\xi$) \mathbf{G}_{1D} space: arc

The ellipse criterion (S80) exhibits an arc morphology when scanning \mathbf{G}_{1D} at fixed $\Delta\mathbf{K}_\xi$, because the mapping from \mathbf{G}_{1D} to $(\delta q_\perp, \delta q_\parallel)$ is nonlinear. For the symmetric layer rotation used throughout (Sec. S1.1), $\Delta\mathbf{K}_\xi = k_\theta(0, \xi)^T$ with $k_\theta \equiv |\Delta\mathbf{K}_\xi|$. We introduce the dimensionless scan variable $\mathbf{g} \equiv n_{1D}\mathbf{G}_{1D}/k_\theta = (g_x, g_y)$ and $g \equiv |\mathbf{g}| = \sqrt{g_x^2 + g_y^2}$. Using Eqs. (S70)–(S72) one finds

$$\delta q_\perp = \xi k_\theta \left(\frac{g_x}{g} \right), \quad \delta q_\parallel = \xi k_\theta \left(\frac{g_y}{g} - g \right). \quad (\text{S81})$$

Substituting Eq. (S81) into the ellipse inequality (S80) gives the compact arc criterion

$$\left(\frac{g_x/g}{Q_\perp} \right)^2 + \left(\frac{g_y/g - g}{Q_\parallel} \right)^2 < \frac{1}{k_\theta^2}. \quad (\text{S82})$$

Ridge and “off-centered” arc. For a fixed direction $\hat{\mathbf{n}}$, changing the magnitude G_{1D} tunes only the parallel mismatch δq_\parallel while $\delta q_\perp = \Delta\mathbf{K}_\xi \cdot \hat{\mathbf{n}}_\perp$ is independent of G_{1D} . Equivalently, at fixed $\hat{\mathbf{n}}$ the mismatch scale (S78) is minimized with respect to G_{1D} at $\delta q_\parallel = 0$. This defines the ridge (centerline) of the gapped region, along $\hat{\mathbf{n}}$,

$$\frac{g_y}{g} - g = 0 \quad \iff \quad g_x^2 + \left(g_y - \frac{1}{2} \right)^2 = \left(\frac{1}{2} \right)^2, \quad (\text{S83})$$

a circle centered at $(0, 1/2)$ with radius $1/2$ in the \mathbf{g} coordinates. In the $\mathbf{G}_{1D} = ((\mathbf{G}_{1D})_x, (\mathbf{G}_{1D})_y)$ coordinates, this corresponds to

$$(\mathbf{G}_{1D})_x^2 + \left((\mathbf{G}_{1D})_y - \frac{k_\theta}{2n_{1D}} \right)^2 = \left(\frac{k_\theta}{2n_{1D}} \right)^2, \quad (\text{S84})$$

a circle centered at $(0, k_\theta/(2n_{1D}))$ with radius $k_\theta/(2n_{1D})$, as Fig. S7b shows. The exact-resonance point $((\mathbf{G}_{1D})_x, (\mathbf{G}_{1D})_y) = (0, k_\theta/n_{1D})$ lies on this circle but is not its center, explaining why the gapped region in a fixed- $\Delta\mathbf{K}_\xi$ map is generically off-centered. Equation (S84) for $n_{1D} = 1$ clearly reproduces the ridge of the near-resonant arc in Figs. 1b and S8: the circle passes through the $n_{1D} = 1$ resonant point and is centered at the $n_{1D} = 2$ point.

The finite width around the ridge is set by Eq. (S82); moreover, even on the ridge a gap requires the transverse condition $|v_x^{\text{eff}} \delta q_\perp| < 2|m_z|/\hbar$, so only a segment of the ridge circle appears as a bright arc.

Supplementary Note S5.4 Complementary representation: gapped region in (fixed \mathbf{G}_{1D}) $\Delta\mathbf{K}_\xi$ space: filled ellipse

If, instead, we scan $\Delta\mathbf{K}_\xi$ while holding \mathbf{G}_{1D} fixed, the mapping $\Delta\mathbf{K}_\xi \mapsto (\delta q_\parallel, \delta q_\perp)$ is linear. Writing $\Delta\mathbf{K}_\xi = K_\parallel \hat{\mathbf{n}} + K_\perp \hat{\mathbf{n}}_\perp$, Eq. (S72) gives $\delta q_\parallel = K_\parallel - \xi n_{1D} G_{1D}$ and $\delta q_\perp = K_\perp$. Then Eq. (S80) becomes the filled ellipse

$$\frac{K_\perp^2}{Q_\perp^2} + \frac{(K_\parallel - \xi G_{1D})^2}{Q_\parallel^2} < 1. \quad (\text{S85})$$

Thus the filled-ellipse picture is recovered when the scan variables are chosen to be the mismatch components themselves as Fig. S7c shows.

Supplementary Note S5.5 Beyond the near-resonant, gapped region

Solving Eq. (S75) at charge neutrality ($E = 0$) for a given momentum mismatch $\delta\mathbf{q}_\xi$ yields the locations of the band-touching (Dirac) nodes,

$$\mathbf{q}_\pm = \pm \frac{\delta\mathbf{q}_\xi}{2} \sqrt{1 - \left(\frac{|m_z|}{\varepsilon_{\text{mm}}(\delta\mathbf{q}_\xi)} \right)^2}, \quad (\text{S86})$$

provided that real solutions exist. When $|m_z| > \varepsilon_{\text{mm}}(\delta\mathbf{q}_\xi)$, no real \mathbf{q}_\pm exists, indicating that the two nodes annihilate and a gap opens. The critical case $|m_z| = \varepsilon_{\text{mm}}(\delta\mathbf{q}_\xi)$ corresponds to node merging at a single momentum point and therefore delineates the boundary of the gapped region in the configuration map. For $|m_z| < \varepsilon_{\text{mm}}(\delta\mathbf{q}_\xi)$, two distinct Dirac nodes survive; as $|m_z|/\varepsilon_{\text{mm}} \rightarrow 0$, they approach the uncoupled Dirac points at $\mathbf{q} = \pm\delta\mathbf{q}_\xi/2$, yielding two separated Dirac cones. This is the off-resonant regime (Sec. S7).

Supplementary Note S5.6 Practical notes

Fixing u_l vs. fixing v_l in a $|\mathbf{G}_{1D}|$ scan. Because $u_l = v_l/(\hbar v_F G_{1D})$ (Eq. (S8)), scanning $|\mathbf{G}_{1D}|$ changes $|u_l|$ if v_l is held fixed. To isolate the geometric momentum-mismatch effect in Eq. (S82), it is therefore natural to hold u_l fixed (so that m_z and $v_{x/y}^{(l)}$ are independent of $|\mathbf{G}_{1D}|$ at this level). Holding v_l fixed instead promotes Q_\parallel and Q_\perp to slowly varying functions of G_{1D} through the Bessel factors and η_l .

Closed-form estimates for arc widths. Using Eq. (S52), $v_{\perp}^{\text{eff}} = Zv_{\text{F}}\sqrt{(\eta_1 - 3u_0^2)(\eta_2 - 3u_0^2)}$, $v_{\parallel}^{\text{eff}} = Zv_{\text{F}}(1 - 3u_0^2)$, and $u_0 \equiv t_0/(\hbar v_{\text{F}}k_{\theta})$. For odd $n_{1\text{D}}$ in the same-chirality regime, Eq. (S54) implies $|m_z| \simeq Zt_0|\mathcal{J}_{+,-\xi n_{1\text{D}}}|$ with $\mathcal{J}_{+,p}$ defined in Eq. (S31).

A simple geometric readout of Eq. (S82) is obtained from cuts of the (g_x, g_y) map: for $g_x = 0$ and $g_y > 0$, one has $|1 - g_y| < 2u_0J_{n_{1\text{D}}}(|u_+|/2)/(1 - 3u_0^2)$ (vertical thickness $4u_0J_{n_{1\text{D}}}(|u_+|/2)/(1 - 3u_0^2)$ around the exact-resonance point), while near $g_y \approx 1$ and $|g_x| \ll 1$ the horizontal extent scales as $|g_x|_{\text{max}} \sim 2u_0J_{n_{1\text{D}}}(|u_+|/2)/\sqrt{(\eta_1 - 3u_0^2)(\eta_2 - 3u_0^2)}$.

Beyond the two-cone criterion. Equation (S80) describe the near-resonant gap mechanism within the renormalized two-cone truncation. In the full continuum model (Sec. S2), additional minibands and indirect overlaps can further reduce the global gap, and therefore an insulating phase is ultimately verified by the numerically evaluated Δ_{dir} in Eq. (S19).

Supplementary Note S6 Berry-curvature diagnostics and Chern-triviality

This note defines the Berry-curvature diagnostics used in this work and summarizes the symmetry reason why the charge-neutrality gaps reported here are Chern-trivial. All Berry-curvature maps and Chern numbers are obtained numerically from the fully periodic single-valley continuum Hamiltonian (Sec. S2) using a gauge-invariant discretization.

Supplementary Note S6.1 $C_{2z}T$ symmetry and Chern-triviality in scalar TBG–1D

We fix the real-space origin at an AA region of the moiré pattern, which is a C_{2z} center of the continuum model. For a scalar 1D potential of the form $V_l(\mathbf{r}) = (|v_l|/2)\cos(\mathbf{G}_{1\text{D}} \cdot \mathbf{r} + \phi_l)$, the potential preserves C_{2z} about the AA origin only when it is even under $\mathbf{r} \rightarrow -\mathbf{r}$, i.e., when $\phi_l = 0$ or π (equivalently, when v_l is real and the modulation is cosine-type about the chosen origin). In this cosine registry, the single-valley Hamiltonian inherits the antiunitary symmetry $C_{2z}T$ within each valley. Because $C_{2z}T$ leaves the rBZ momentum invariant, it forces the Berry curvature to vanish pointwise in the rBZ and therefore guarantees that the valley Chern number of any isolated set of minibands is zero^{12–14}.

Starting from this $C_{2z}T$ -symmetric limit, we continuously vary the parameters $(\theta, |u_l|, \phi_l)$ explored in this work. We find that whenever a direct charge-neutrality gap persists across the rBZ, the valley Chern number of the occupied subspace remains $C_{\xi} = 0$. This is consistent with adiabatic continuity: in the absence of a gap closing, C_{ξ} cannot change from its $C_{2z}T$ -symmetric value. When the registry phases ϕ_l break $C_{2z}T$, the Berry curvature can become finite; however, in the gapped configurations studied here it integrates to zero, so the gap remains Chern-trivial.

Supplementary Note S6.2 Non-Abelian Fukui curvature and valley Chern number

For a fixed valley $\xi = \pm 1$, we diagonalize the periodic continuum Hamiltonian on a uniform mesh $\{\mathbf{q}\}$ in the rBZ. Let $\{|u_a(\mathbf{q})\}_{a=1}^{N_{\text{occ}}}$ be an orthonormal basis of the occupied subspace at \mathbf{q} . Following Fukui–Hatsugai–Suzuki¹⁵, we define the overlap (link) matrices along the two mesh directions $i = 1, 2$,

$$[W_i(\mathbf{q})]_{ab} \equiv \langle u_a(\mathbf{q}) | u_b(\mathbf{q} + \Delta\mathbf{q}_i) \rangle, \quad U_i(\mathbf{q}) \equiv \frac{\det W_i(\mathbf{q})}{|\det W_i(\mathbf{q})|}. \quad (\text{S87})$$

The lattice field strength on each plaquette is

$$F_{12}(\mathbf{q}) \equiv \text{Arg}\left[U_1(\mathbf{q}) U_2(\mathbf{q} + \Delta\mathbf{q}_1) U_1(\mathbf{q} + \Delta\mathbf{q}_2)^{-1} U_2(\mathbf{q})^{-1}\right], \quad (\text{S88})$$

where Arg denotes the principal branch. The valley Chern number of the occupied subspace is then

$$C_\xi = \frac{1}{2\pi} \sum_{\mathbf{q} \in \text{mesh}} F_{12}(\mathbf{q}), \quad (\text{S89})$$

which is integer-valued when the occupied subspace is separated from the unoccupied subspace by a nonzero direct gap throughout the rBZ. For an isolated single band, the Abelian specialization is obtained by setting $N_{\text{occ}} = 1$ in Eqs. (S87)–(S88).

Supplementary Note S7 Off resonance: perturbative anisotropic Dirac velocities

In a generic (off-resonant) TBG–1D configuration, the Dirac-point mismatch $\Delta\mathbf{K}_\xi$ exceeds the magnitude of the mass channel (Sec. S5.5) and cannot be bridged by any integer harmonic of the 1D modulation. Consequently, there is no direct Dirac–Dirac resonance between the two layers, and the low-energy spectrum near charge neutrality remains gapless. The leading effect of the hybrid moiré–1D structure is instead an anisotropic renormalization of the Dirac velocities: in the regime $|E|, \hbar v_F |\mathbf{q}| \ll \mathcal{E}_\theta, \mathcal{E}_{1\text{D}}$ near the Dirac point, the velocity perpendicular to the modulation can be suppressed beyond the pristine TBG value and tuned to zero by an externally controllable potential.

Supplementary Note S7.1 Coordinate convention and minimal low-energy subspace

In an off-resonant configuration, the direction of $\mathbf{G}_{1\text{D}}$ is not locked to any crystallographic axis. Without loss of generality, we choose coordinates such that the 1D modulation is along the y direction,

$$\mathbf{G}_{1\text{D}} = G_{1\text{D}} \hat{\mathbf{y}} = \begin{pmatrix} 0 \\ G_{1\text{D}} \end{pmatrix}. \quad (\text{S90})$$

We focus on the low-energy Dirac cone of layer $l = 1$ in a fixed valley ξ and define the target (P) subspace as the two-component sublattice spinor at momentum \mathbf{q} measured from $\mathbf{K}_\xi^{(1)}$: $|P\rangle \equiv |\mathbf{q}, 1\rangle$. In the off-resonant regime, all states reached from $|P\rangle$ by a single moiré tunnelling event or a single 1D scattering event are remote, i.e., high-energy, and can be treated perturbatively.

Supplementary Note S7.2 Minimal momentum-space Hamiltonian and P/Q partition

We retain the minimal set of remote (Q) states coupled to $|P\rangle$ at first order: (i) three layer-2 states connected by the first-star moiré tunnelling $T_\xi(\mathbf{r})$, and (ii) two layer-1 sidebands connected by the 1D potential $V_1(\mathbf{r})$,

$$|Q_M\rangle \equiv \begin{pmatrix} |\mathbf{q} + \mathbf{q}_0^\xi, 2\rangle \\ |\mathbf{q} + \mathbf{q}_1^\xi, 2\rangle \\ |\mathbf{q} + \mathbf{q}_2^\xi, 2\rangle \end{pmatrix}, \quad |Q_{1\text{D}}\rangle \equiv \begin{pmatrix} |\mathbf{q} + \mathbf{G}_{1\text{D}}, 1\rangle \\ |\mathbf{q} - \mathbf{G}_{1\text{D}}, 1\rangle \end{pmatrix}. \quad (\text{S91})$$

In the composite basis $(|P\rangle^T, |Q_M\rangle^T, |Q_{1D}\rangle^T)^T$, the minimal Hamiltonian reads

$$H_\xi^{(\min)}(\mathbf{q}) = \begin{pmatrix} H_{PP}(\mathbf{q}) & H_{PQ_M} & H_{PQ_{1D}} \\ H_{Q_MP} & H_{Q_MQ_M}(\mathbf{q}) & 0 \\ H_{Q_{1D}P} & 0 & H_{Q_{1D}Q_{1D}}(\mathbf{q}) \end{pmatrix}. \quad (\text{S92})$$

Here

$$\begin{aligned} H_{PP}(\mathbf{q}) &= h_\xi^{(1)}(\mathbf{q}), \\ H_{PQ_M} &= ((T_0^\xi)^\dagger, (T_1^\xi)^\dagger, (T_2^\xi)^\dagger) = H_{Q_MP}^\dagger, \\ H_{PQ_{1D}} &= \left(\frac{v_1^*}{4}\mathbb{I}, \frac{v_1}{4}\mathbb{I}\right) = H_{Q_{1D}P}^\dagger, \\ H_{Q_MQ_M}(\mathbf{q}) &= \text{diag}(h_\xi^{(2)}(\mathbf{q} + \mathbf{q}_0^\xi), h_\xi^{(2)}(\mathbf{q} + \mathbf{q}_1^\xi), h_\xi^{(2)}(\mathbf{q} + \mathbf{q}_2^\xi)), \\ H_{Q_{1D}Q_{1D}}(\mathbf{q}) &= \text{diag}(h_\xi^{(1)}(\mathbf{q} + \mathbf{G}_{1D}), h_\xi^{(1)}(\mathbf{q} - \mathbf{G}_{1D})). \end{aligned} \quad (\text{S93})$$

In this minimal construction, $|Q_M\rangle$ and $|Q_{1D}\rangle$ do not couple directly.

Supplementary Note S7.3 Löwdin downfolding and controlled linearization

Applying momentum-resolved Löwdin partitioning to Eq. (S92) yields the projected eigenvalue problem

$$\left[H_{PP}(\mathbf{q}) + \Sigma_M(E, \mathbf{q}) + \Sigma_{1D}(E, \mathbf{q}) \right] \Psi = E\Psi, \quad (\text{S94})$$

with self-energies

$$\Sigma_M(E, \mathbf{q}) = H_{PQ_M} [E - H_{Q_MQ_M}(\mathbf{q})]^{-1} H_{Q_MP}, \quad (\text{S95})$$

and

$$\Sigma_{1D}(E, \mathbf{q}) = H_{PQ_{1D}} [E - H_{Q_{1D}Q_{1D}}(\mathbf{q})]^{-1} H_{Q_{1D}P}. \quad (\text{S96})$$

Because we are interested in $|E|, \hbar v_F |\mathbf{q}| \ll \mathcal{E}_\theta, \mathcal{E}_{1D}$, we use the controlled resolvent expansion to first order in (E, \mathbf{q}) :

$$[E - H_{QQ}^{(0)} - H_{QQ}^{(1)}(\mathbf{q})]^{-1} \approx (-H_{QQ}^{(0)})^{-1} - (-H_{QQ}^{(0)})^{-1} (E - H_{QQ}^{(1)}(\mathbf{q})) (-H_{QQ}^{(0)})^{-1} \quad (\text{S97})$$

for any remote block of the form $H_{QQ}(\mathbf{q}) = H_{QQ}^{(0)} + H_{QQ}^{(1)}(\mathbf{q})$, with $H_{QQ}^{(0)} \sim \mathcal{E}_\theta$ or \mathcal{E}_{1D} and $H_{QQ}^{(1)}(\mathbf{q}) = \mathcal{O}(\hbar v_F |\mathbf{q}|)$. The linearized moiré and 1D self-energies take the compact form

$$\begin{aligned} \Sigma_M(E, \mathbf{q}) &\approx -3u_0^2 h_\xi^{(1)}(\mathbf{q}) - 6u_0^2 E \mathbb{I}, \\ \Sigma_{1D}(E, \mathbf{q}) &\approx \frac{|u_1|^2}{8} \left[-h_\xi^{(1)}(q_x \hat{\mathbf{x}}) + h_\xi^{(1)}(q_y \hat{\mathbf{y}}) - E \mathbb{I} \right]. \end{aligned} \quad (\text{S98})$$

The moiré contribution is the standard second-order result of pristine rigid TBG and is isotropic by the C_3 symmetry of the first-star set $\{\mathbf{q}_j^\xi\}_{j=0,1,2}^{1;2}$. By contrast, the 1D contribution distinguishes the x and y directions, reflecting Bragg scattering by $\pm \mathbf{G}_{1D}$ ^{7;8}.

Supplementary Note S7.4 Renormalized Dirac Hamiltonian and anisotropic velocities

From Eq. (S94), we get the 2×2 effective Hamiltonian near the layer-1 Dirac point

$$h_{\xi, \text{eff}}^{(1)}(\mathbf{q}) = -\hbar \left(\xi v_x^* q_x \sigma_x^{(1)} + v_y^* q_y \sigma_y^{(1)} \right), \quad (\text{S99})$$

with the renormalized velocities

$$\begin{aligned} v_x^* &= \left(\frac{1 - 3u_0^2 - |u_1|^2/8}{1 + 6u_0^2 + |u_1|^2/8} \right) v_F, \\ v_y^* &= \left(\frac{1 - 3u_0^2 + |u_1|^2/8}{1 + 6u_0^2 + |u_1|^2/8} \right) v_F. \end{aligned} \quad (\text{S100})$$

Since $h_{\xi, \text{eff}}^{(1)}(\mathbf{q})$ contains only $\sigma_{x,y}$ terms and therefore cannot generate a mass term: the Dirac point remains protected, consistent with both pristine TBG and monolayer graphene under a scalar 1D potential.

Supplementary Note S7.5 Limiting cases, flattening line, and interpretation

Pristine-TBG limit. For $u_1 \rightarrow 0$ we recover the familiar isotropic second-order velocity renormalization of rigid TBG, $\lim_{u_1 \rightarrow 0} v_x^* = \lim_{u_1 \rightarrow 0} v_y^* = v_{\text{TBG}}^* = v_F(1 - 3u_0^2)/(1 + 6u_0^2)^{1/2}$.

Monolayer/1D limit. For $u_0 \rightarrow 0$ the 1D potential yields an anisotropic renormalization: $\lim_{u_0 \rightarrow 0} v_x^* = v_F(1 - |u_1|^2/8)/(1 + |u_1|^2/8)$ and $\lim_{u_0 \rightarrow 0} v_y^* = v_F$, in agreement with the known behavior of monolayer graphene under a scalar 1D potential^{7;8}.

Flattening condition (“magic line” in $(\theta, |u_1|)$). Equation (S100) shows that the 1D potential provides an independent tuning knob that suppresses the velocity perpendicular to the modulation. Complete flattening in the x direction, $v_x^* = 0$, occurs at

$$\begin{aligned} |u_1| &= \sqrt{8(1 - 3u_0^2)} \\ &\approx 2\sqrt{2} \left[1 - 3 \left(\frac{3t_0 a}{4\pi \hbar v_F \theta} \right)^2 \right]^{1/2}, \quad (\theta \ll 1). \end{aligned} \quad (\text{S101})$$

The red dashed line in Fig. 4b represents Eq. (S100) which provides a practical design relation between the twist angle and the required strength of the 1D modulation.

Supplementary Note S7.6 Neglected terms and validity

Leading neglected contributions. Within the minimal Q space of Eq. (S91) and the linearization Eq. (S97), we retain only (a) terms up to second order in the couplings and (b) terms up to linear order in (E, \mathbf{q}) in the projected Hamiltonian. Accordingly, we neglect: (i) higher-order virtual processes in the couplings, such as $\mathcal{O}(u_0^4)$ and $\mathcal{O}(|u_1|^4)$, as well as mixed moiré+1D processes that start at $\mathcal{O}(u_0^2|u_1|^2)$ and require intermediate states beyond the minimal Q space (e.g., states involving both \mathbf{q}_j^ξ and $\pm \mathbf{G}_{1D}$); (ii) quadratic-and-higher corrections in (E, \mathbf{q}) from the resolvent expansion, namely terms of order $\mathcal{O}((\hbar v_F |\mathbf{q}|)^2 / \mathcal{E}_\theta)$ and $\mathcal{O}((\hbar v_F |\mathbf{q}|)^2 / \mathcal{E}_{1D})$, as well as $\mathcal{O}(E^2)$ and $\mathcal{O}(E \hbar v_F |\mathbf{q}|)$ terms (equivalently, higher-order momentum/energy corrections beyond the linear Dirac theory); and (iii) the effect of a 1D potential on layer 2, which influences the layer-1 projected Hamiltonian only via mixed processes involving both moiré tunnelling and additional layer-2 sidebands (e.g., intermediate states $|\mathbf{q} + \mathbf{q}_j^\xi \pm \mathbf{G}_{1D}, 2\rangle$), so that its leading contribution is of higher order (schematically $\mathcal{O}(u_0^2|u_2|^2)$ and beyond) and is neglected in the present minimal second-order treatment.

Validity conditions. The results in Eqs. (S98)–(S100) are controlled under $|E|$, $\hbar v_F |\mathbf{q}| \ll \mathcal{E}_\theta$, \mathcal{E}_{1D} , $|u_0| \ll 1$, $|u_1| \ll 1$ for the second-order expansion in u_0 and u_1 . Additionally, the configuration must be off-resonant in the sense that no integer harmonic bridges the Dirac mismatch at the low-energy scale.

Supplementary Note S8 Feasibility estimates

This note provides order-of-magnitude experimental feasibility estimates for realizing the hybrid moiré-1D band engineering studied in this work in an electrostatically patterned device. We focus on the same-chirality case $\chi_{\text{rel}} = +1$, whereas the corresponding case $\chi_{\text{rel}} = -1$ can be treated by the same steps and is not discussed further. For $\chi_{1D} = +1$, odd n_{1D} is the leading gapping class.

We further focus on the experimentally common single-sided electrostatic patterning, where the induced layer potentials are nearly equal and phase-aligned, $|u_1| \approx |u_2|$ and $\phi_1 \approx \phi_2$, so that $|u_-| (\approx 0) \ll |u_+| (\approx 2|u_1|, 2|u_2|)$ (Eq. (S31)). Achieving independent control of the amplitude and phase on the two layers at the relevant length scale, i.e., $|u_1| \neq |u_2|$ and $\phi_1 \neq \phi_2$, requires more elaborate device engineering and is currently challenging; therefore we do not evaluate the feasibility of that general case here and only comment on its qualitative impact on the gap opening in Sec. S4.7 for reference. In fact, $|u_1| \approx |u_2|$ and $\phi_1 \approx \phi_2$ are not only favorable for fabrication but also helpful for the gap-opening at resonant configurations; the mass term is controlled by the in-phase combination u_+ , while the node-shifting term is controlled by the out-of-phase combination u_- (Sec. S4.5). Therefore single-sided gating that yields $|u_-| \ll |u_+|$ suppresses node-shifting terms and tends to maximize the intended gap within the minimal-wave description.

- **Period of the unidirectional scalar potential for gap opening at charge neutrality point.**

We assess the experimental feasibility of the period of the 1D potential to open a gap by exact Dirac–Dirac resonance, $\Delta \mathbf{K}_\xi = \xi n_{1D} \mathbf{G}_{1D}$ with odd n_{1D} , in Sec. S8.2.

- **Two practical resonant routes and the key trade-off.**

One may target resonance either with $n_{1D} = 1$ (short L_{1D}) or with odd $n_{1D} \geq 3$ (longer L_{1D}). Larger n_{1D} makes lithographic fabrication more forgiving by enlarging L_{1D} (Sec. S8.2) and reduces the attenuation of the potential strength at the graphene plane (Sec. S8.3).

The trade-off is that the resonant mass amplitude is controlled by a higher-order (n_{1D} -th) Bessel coefficient. Thus, higher-order n_{1D} channels remain parametrically suppressed at weak-to-moderate modulation, so $n_{1D} = 1$ is preferred unless the induced modulation get sufficiently large (Sec. S8.3).

- **Higher harmonics in realistic waveforms: factors for maintaining the selection rules.**

A realistic patterned gate typically produces a non-sinusoidal waveform containing higher spatial harmonics at $m \mathbf{G}_{1D}$ ($m \geq 2$) (Sec. S8.3). The higher ($m \geq 2$) harmonics are partially suppressed by dielectric layers, where the suppression is weak for very thin spacers (1–2 nm) or a long L_{1D} but can become significant for thicker dielectrics (10 nm) or a short L_{1D} .

The parity selection rule becomes clear when the even- m harmonics of the potential are suppressed, e.g., by ensuring the potential to have half-translation antisymmetry, which suppresses even harmonics in the waveform.

- **Feasibility metric, geometric errors and tolerances**

In globally periodic (rank-2) resonant/near-resonant configurations, our primary interest is a direct gap at or near the CNP Δ_{dir} ; we discuss the feasibility in Secs. S8.2 and S8.3. Section S8.4 estimates tolerance requirements of twist angle, 1D modulation period and alignment for resonant/near-resonant configurations, and compare them with the realistic windows achieved with the current fabrication capabilities.

In quasiperiodic (rank-3) settings, where no rBZ exists, our interest lies in the resolvable anisotropic renormalization of Dirac velocities; we discuss the feasibility in Sec. S8.5.

Supplementary Note S8.1 Experimental knobs

Continuum-model parameters and experimental knobs. In the symmetric geometry used in this paper, the Dirac-point mismatch is $\Delta\mathbf{K}_\xi = \xi k_\theta \hat{\mathbf{y}}$ where its magnitude is $k_\theta \equiv |\Delta\mathbf{K}_\xi| = (8\pi/3a) \sin(\theta/2)$ for a given twist angle θ . The reciprocal lattice vector of the unidirectional potential is

$$\mathbf{G}_{1D} = G_{1D}(\sin \varphi_{1D}, \cos \varphi_{1D}), \quad (\text{S102})$$

where φ_{1D} denotes the in-plane orientation of the 1D modulation ($\varphi_{1D} = 0$ corresponds to $\mathbf{G}_{1D} \parallel \Delta\mathbf{K}_\xi$).

We view a device configuration as specified by

$$(\theta, L_{1D}, \varphi_{1D}, d_{\text{diel}}), \quad (\text{S103})$$

where $L_{1D} = 2\pi/G_{1D}$ is the period of the 1D modulation, d_{diel} is the effective separation between graphene and the patterned dielectric.

Supplementary Note S8.2 Resonant and near-resonant geometric design and mass channel magnitude

This section summarizes practical geometric targets for approaching Dirac–Dirac resonance and discuss how these targets relate to demonstrated nanofabrication scales.

Exact resonance and target periods. Momentum (Dirac) resonance is defined by Eq. (S4), $\Delta\mathbf{K}_\xi = \xi n_{1D} \mathbf{G}_{1D}$. Choosing $\mathbf{G}_{1D} \parallel \Delta\mathbf{K}_\xi$ reduces the resonant condition to a scalar matching,

$$k_\theta = n_{1D} G_{1D} \iff L_{1D}^{(n_{1D})}(\theta) = \frac{2\pi n_{1D}}{k_\theta} = \frac{3a}{4} \frac{n_{1D}}{\sin(\theta/2)} \approx \frac{3a}{2} \frac{n_{1D}}{\theta}, \quad (\text{S104})$$

where the final expression holds for $\theta \ll 1$ with θ in radians. In the same-chirality case $\chi_{\text{rel}} = +1$ relevant for our numerics, odd n_{1D} is the leading gapping class at charge neutrality (Sec. S4); hence we focus on odd n_{1D} in the targets below.

Fabrication scales. Experimentally, electrostatically defined superlattice potentials with sub-100 nm pitch have been realized using several complementary patterning strategies, including arrays of metallic gates down to 100 nm¹⁶, block-copolymer templating down to 38 nm¹⁷, and dielectric patterning with sub-40 nm pitch^{10;18}. Related nanofabrication approaches also demonstrate periodic patterning at even smaller length scales, such as 16 nm by focused ion beam milling¹⁹ and ~ 5 nm by electron-beam induced deposition²⁰. Taken together, these benchmarks suggest that the odd- n_{1D} target periods in Table S1 are challenging yet broadly compatible with current nanofabrication capabilities; in particular, odd $n_{1D} \geq 3$ places the required L_{1D} in the 20–100 nm range for $\theta \sim 1^\circ\text{--}3^\circ$.

θ	\bar{u}_l for $v_l = 0.26$ eV	$L_{1D}^{(1)}$	$t_0 J_1(\bar{u}_l)$	$L_{1D}^{(3)}$	$t_0 J_3(3\bar{u}_l)$	$L_{1D}^{(5)}$	$t_0 J_5(5\bar{u}_l)$
1°	1.33	21.1	58.1	63.4	47.3	105.7	40.7
2°	0.665	10.6	34.7	31.7	14.1	52.9	7.24
3°	0.443	7.05	23.8	21.1	4.81	35.2	1.24

Table S1: Target 1D periods $L_{1D}^{(n_{1D})}$ (nm) for exact resonance (Eq. (S104)) (Sec. S8.2), effective modulation strength $\bar{u}_l = |v_l|/(\hbar v_F k_\theta)$, and the magnitude of the mass channel $t_0 J_{n_{1D}}(|u_l|) = t_0 J_{n_{1D}}(n_{1D}\bar{u}_l)$ (meV) under the commensurate condition and for $u_1 = u_2 \equiv u_l$, $\phi_1 = \phi_2$. We evaluated \bar{u}_l and $J_{n_{1D}}(\bar{u}_l)$ for modulation strength $v_l = 0.26$ eV with $t_0 \approx 0.110$ eV. We list odd $n_{1D} = 1, 3, 5$, which are the leading gapping class for $\chi_{\text{rel}} = +1$ (Sec. S4).

Mass channel magnitude and choosing odd n_{1D} given an achievable $|v_l|$. In our framework (Secs. S3–S5), the experimentally controlled modulation is taken to be dominated by the fundamental Fourier component at \mathbf{G}_{1D} , while the resonant coupling itself arises from the $p_0 = -\xi n_{1D}$ Fourier harmonic of the dressed interlayer tunnelling (Sec. S4). For the experimentally common case of single-sided patterning with nearly equal and in-phase layer potentials, $u_1 = u_2 \equiv u_l$ and $|u_+|/2 = |u_l|$. Under the commensurate condition $k_\theta = n_{1D}G_{1D}$, $|u_l| = |v_l|/(\hbar v_F G_{1D}) = n_{1D}|v_l|/(\hbar v_F k_\theta)$, so the odd- n_{1D} resonant mass weight scales as $J_{n_{1D}}(|u_l|) = J_{n_{1D}}(n_{1D}\bar{u}_l)$ with

$$\bar{u}_l \equiv |v_l|/(\hbar v_F k_\theta). \quad (\text{S105})$$

Here \bar{u}_l is a dimensionless measure of the effective modulation strength set by the induced potential amplitude $|v_l|$ at a given twist angle (fixed $k_\theta = |\Delta\mathbf{K}_\xi|$). In the weak-modulation regime $\bar{u}_l \ll 1$ (equivalently $|v_l| \ll \hbar v_F k_\theta$),

$$J_{n_{1D}}(n_{1D}\bar{u}_l) \approx \frac{1}{n_{1D}!} \left(\frac{n_{1D}\bar{u}_l}{2} \right)^{n_{1D}}, \quad (\text{S106})$$

so higher-order odd- n_{1D} channels are parametrically suppressed and $n_{1D} = 1$ is favored. As \bar{u}_l approaches order unity, the argument grows proportionally to n_{1D} and the $n_{1D} = 3, 5, \dots$ harmonics can become appreciable. For example, patterned-dielectric 1D superlattices report dimensionless strengths up to $u = vL/(\hbar v_F) \sim 7\pi$ for $L \sim 55$ nm, corresponding to screened modulation amplitudes v on the order of 0.26 eV¹⁰. We emphasize that $|v_l| \approx 0.26$ eV is not a structural upper bound of patterned-dielectric platforms, but merely a representative value demonstrated in existing devices and used here as a conservative reference scale. Taking this value as a reference scale, Table S1 summarizes \bar{u}_l and representative odd- n_{1D} weights for $\theta = 1^\circ, 2^\circ, 3^\circ$. In this range, odd $n_{1D} \geq 3$ channels are already comparable to $n_{1D} = 1$ at $\theta \approx 1^\circ$, remain non-negligible at $\theta \approx 2^\circ$ (with $n_{1D} = 3$ favored over $n_{1D} = 5$), but are strongly suppressed at $\theta \approx 3^\circ$. Finally, the longer period associated with odd $n_{1D} \geq 3$ can be advantageous both for fabrication and for reducing finite-distance attenuation of the fundamental component at $G_{1D} = k_\theta/n_{1D}$ (Sec. S8.3).

Equation (S106) captures an important design trade-off when one targets resonance either with $n_{1D} = 1$ (short L_{1D}) or with odd $n_{1D} \geq 3$ (longer L_{1D}). While larger n_{1D} makes lithographic fabrication more forgiving by enlarging L_{1D} , its mass channels remain parametrically suppressed at weak-to-moderate modulation. Thus, $n_{1D} = 1$ is preferred unless the induced modulation get sufficiently large.

Near-resonant window. Exact resonance points are measure zero in the \mathbf{G}_{1D} configuration map; experimentally, it is sufficient to approach a resonant point so that the momentum mismatch $\delta\mathbf{q}_\xi^{(n_{1D})}$ (Eq. (S6)) lies within the gapped region derived in Sec. S5. In Sec. S8.4 we translate the corresponding $\delta\mathbf{q}$ window into tolerances in $(\theta, \lambda_{1D}, \varphi_{1D})$.

Supplementary Note S8.3 Electrostatics: finite-distance attenuation of a periodic gate potential and parity leakage from higher (even) harmonics

Realistic potential waveforms and higher harmonics The continuum model in this work assumes that the 1D modulation entering each layer is well approximated by a single cosine, $V_l(y) = |v_l| \cos(G_{1D}y + \phi_l)/2$ (Eq. (S3)). A patterned gate, however, may produce a non-sinusoidal potential profile, i.e. a superposition of multiple harmonics at the same reciprocal vector \mathbf{G}_{1D} . Because the resonant selection rules and minimal models in Secs. S3–S5 are derived for a single harmonic, it is useful to parameterize and estimate the harmonic content of a realistic gate-induced potential.

Finite-distance attenuation of the 1D modulation The 1D modulation, containing higher spatial harmonics m , is generated at a patterned dielectric plane ($z = 0$) separated from the graphene plane ($z = d_{\text{diel}}$) by a finite distance d_{diel} and forms the 1D potential at the graphene plane (for each layer l)

$$V_l(y) = \frac{1}{4} \sum_{m=1}^{\infty} (v_{l,m} e^{imG_{1D}y} + v_{l,m}^* e^{-imG_{1D}y}), \quad (v_{l,1} \equiv v_l), \quad (\text{S107})$$

where $v_{l,m}$ are complex Fourier amplitudes of the m -th harmonic. In the absence of electronic screening, the electrostatic transfer from the patterned plane to the graphene plane obeys Laplace attenuation,

$$v_{l,m} \equiv v_{l,m}(z = d_{\text{diel}}) \approx v_{l,m}(z = 0) e^{-mG_{1D}d_{\text{diel}}}, \quad (\text{S108})$$

where $v_{l,m}(0)$ denotes the amplitude of m -th harmonic at the patterned plane. The z -direction decay of the m -th in-plane harmonic is

$$mG_{1D}d_{\text{diel}} = 2\pi m d_{\text{diel}}/L_{1D} = mk_{\theta} d_{\text{diel}}/n_{1D}. \quad (\text{S109})$$

Consequently, the higher ($m \geq 2$) in-plane harmonics decays to the graphene plane faster than the fundamental ($m = 1$) harmonic. Electronic screening further reduces all $|v_{l,m}|$, but the relative harmonic weights are largely set by the waveform at the patterned plane together with the exponential attenuation factor Eq. (S109).

Beyond the trade-off discussed in Sec. S8.2, Eqs. (S108) and (S109) highlight an additional practical consideration in choosing n_{1D} : for a fixed spacer thickness, shorter periods L_{1D} (corresponding to smaller n_{1D} at fixed k_{θ}) suffer stronger finite-distance attenuation, whereas this effect becomes much less pronounced for very thin spacers. For instance, the factor $e^{-2\pi d_{\text{diel}}/L_{1D}}$ for the fundamental harmonic is ≈ 0.04 for $L_{1D} = 20$ nm and ≈ 0.35 for $L_{1D} = 60$ nm when $d_{\text{diel}} = 10$ nm, while it is ≈ 0.73 and ≈ 0.90 , respectively, when $d_{\text{diel}} = 1$ nm.

Parity leakage from even-harmonic contamination. With a single harmonic ($m = 1$), $\cos \alpha_l(y)$ contains only even multiples of G_{1D} while $\sin \alpha_l(y)$ contains only odd multiples. This property is the origin of the clear even/odd n_{1D} selection rule for gap opening at leading order in small θ . If, however, even harmonics are present ($v_{l,2}, v_{l,4}, \dots \neq 0$), $\cos \alpha_l$ and $\sin \alpha_l$ generally contain both even and odd Fourier components. In the resonant two-cone description (Sec. S4), this appears as small leakage terms that admix the Pauli-matrix subspace associated with the opposite parity of p . A sufficient condition to suppress even harmonics is to make sure the potential flips sign under a half-period translation,

$$V_l(y + L_{1D}/2) - \bar{V}_l = -[V_l(y) - \bar{V}_l], \quad (\text{S110})$$

where \bar{V}_l is the spatial average over one period.

Supplementary Note S8.4 Geometric errors and tolerances

Section S5 shows that, near a target resonance, the gapped region in mismatch coordinates $(\delta q_{\perp}, \delta q_{\parallel})$ is approximately the filled ellipse Eq. (S80), with semiaxes Q_{\perp} and Q_{\parallel} defined in Eq. (S85). Here we translate this condition into practical tolerances on $(\theta, L_{1D}, \varphi_{1D})$ and discuss additional requirements from disorder and temperature.

From geometric errors to mismatch components. For a fixed integer n_{1D} , the mismatch vector is $\delta \mathbf{q}_{\xi}^{(n_{1D})} = \Delta \mathbf{K}_{\xi} - \xi n_{1D} \mathbf{G}_{1D}$ (Eq. (S6)). Linearizing around an ideal design point $(\theta, L_{1D}, \varphi_{1D} = 0)$ satisfying $k_{\theta} = n_{1D} G_{1D}$ (Eq. (S104)), we obtain, to leading order,

$$\delta q_{\perp} \approx k_{\theta} \delta \varphi_{1D}, \quad \delta q_{\parallel} \approx \delta k_{\theta} + k_{\theta} \frac{\delta L_{1D}}{L_{1D}} + \frac{k_{\theta}}{2} (\delta \varphi_{1D})^2, \quad (\text{S111})$$

where $\delta k_{\theta} = (\partial k_{\theta} / \partial \theta)_{\theta_0} \delta \theta$ and we used $\delta G_{1D} / G_{1D} = -\delta L_{1D} / L_{1D}$. Equation (S111) shows that a small orientation error generates a linear transverse mismatch δq_{\perp} , while its contribution to δq_{\parallel} is only quadratic in $\delta \varphi_{1D}$.

Tolerance formulas. A conservative sufficient condition for remaining in the gapped region is $|\delta q_{\parallel}| < Q_{\parallel}$ and $|\delta q_{\perp}| < Q_{\perp}$, with $Q_{\parallel, \perp}$ defined in Eq. (S85). Using Eq. (S111), we obtain the tolerance for each parameter

$$|\delta \theta| \lesssim \frac{Q_{\parallel}}{(\partial k_{\theta} / \partial \theta)_{\theta_0}}, \quad \left| \frac{\delta L_{1D}}{L_{1D}} \right| \lesssim \frac{Q_{\parallel}}{k_{\theta}}, \quad |\delta \varphi_{1D}| \lesssim \frac{Q_{\perp}}{k_{\theta}}, \quad (\text{S112})$$

evaluated at the target twist angle. Here $(\partial k_{\theta} / \partial \theta)_{\theta_0} = (4\pi/3a) \cos(\theta/2)$, which is nearly constant in the small-angle regime. In the two-cone estimate of Sec. S5, the detuning-dependent gap obeys Eq. (S79). From Eq. (S85), $Q_{\perp} \approx \Delta_{\text{dir}} / (\hbar v_{\perp}^{\text{eff}})$ and $Q_{\parallel} \approx \Delta_{\text{dir}} / (\hbar v_{\parallel}^{\text{eff}})$, where Δ_{dir} is the estimate of the direct gap size.

Below, as an illustrative estimate, we take $v_{\perp, \parallel}^{\text{eff}} \sim v_F(1 - 3u_0^2)/(1 + 6u_0^2)$, i.e., we use the pristine-TBG velocity renormalization.

We do not quote tolerance for $\theta = 1^\circ$ below, because the velocity renormalization becomes nonperturbatively strong in this range, a simple analytic baseline is not quantitatively reliable for assigning a single number to the tolerance criteria. However, the strongly reduced velocity would in fact relax the geometric tolerance.

Twist-angle tolerance For $\Delta_{\text{dir}} = 10$ meV, the twist-angle tolerance $|\delta \theta|$ for a fixed \mathbf{G}_{1D} is $\approx 0.10^\circ$ for $\theta = 2^\circ$ and $\approx 0.069^\circ$ for $\theta = 3^\circ$.

Large-area mapping at $\theta \approx 2^\circ$ reports variations of order 0.08° over hundreds of nm²¹. Protocols targeting improved homogeneity have reported micrometer-scale regions with twist-angle variations as small as $\sim 0.02^\circ$ ²². Thus, although achieving $|\delta \theta| \approx 0.10^\circ$ is experimentally demanding, it appears attainable with state-of-the-art device fabrication and characterization.

1D-period tolerance For $\Delta_{\text{dir}} = 10$ meV, the pattern-period tolerance $|\delta L_{1D} / L_{1D}|$ for fixed θ and φ_{1D} is $\approx 4.9\%$ for $\theta = 2^\circ$ and $\approx 2.3\%$ for $\theta = 3^\circ$.

Fourier analysis reports less-than-3% period variations at a 16 nm-period lattice in Ref.¹⁹ and around-0.1 nm period variations at a 38.1 nm-period lattice in Ref.¹⁷. Thus, such percent-level nonuniformity of $\delta L_{1D} / L_{1D}$ may be achievable with current advanced fabrication capabilities.

1D-axis alignment tolerance For $\Delta_{\text{dir}} = 10$ meV, the pattern-orientation tolerance $|\delta\varphi_{1\text{D}}|$ for fixed θ and $L_{1\text{D}}$ is $\approx 2.8^\circ$ for $\theta = 2^\circ$ and $\approx 1.3^\circ$ for $\theta = 3^\circ$.

Direct experimental reports of the angular misalignment $\delta\varphi_{1\text{D}}$ are scarce in gate-defined 1D-superlattice devices, where the superlattice axis is typically set lithographically and used as a reference. A practical estimate for angular misalignment during graphene transfer is $\delta\varphi_{1\text{D}} \sim \delta x/L_{\text{align}}$, where δx is the overlay/placement error over an alignment length L_{align} (often a few microns), suggesting that sub-degree misalignment is readily achievable in modern lithography.

Supplementary Note S8.5 Off-resonant feasibility and one-directional velocity renormalization

The off-resonant regime derived in Sec. S7 does not rely on global commensurability between $\Delta\mathbf{K}_\xi$ and $\mathbf{G}_{1\text{D}}$. Therefore it is not constrained by the strict tolerance requirements of Sec. S8.4. Instead, feasibility is governed mainly by whether a sufficiently large fundamental 1D coupling $|u_l|$ can be generated while keeping disorder and inhomogeneity small enough to resolve an anisotropic Dirac dispersion.

Design target from the perturbative velocity renormalization. For 1D modulation on layer 1, the downfolded Dirac Hamiltonian takes the anisotropic form Eq. (S99), with renormalized velocities given by Eq. (S100). The key control knob is the 1D potential strength which suppresses the velocity perpendicular to the modulation, in addition to the inherent velocity normalization by the pristine-TBG. The flattening condition $v_x^* = 0$ (Eq. (S101)) occurs at

$$|u_l| = \sqrt{8(1 - 3u_0^2)}, \quad (\text{S113})$$

This condition is most transparent for twist angles above the first magic angle (roughly $\theta \sim 1^\circ$), where $u_0 < 1/\sqrt{3}$ and the perturbative velocity renormalization provides a reliable baseline. For smaller twist angles, pristine TBG is known to exhibit a sequence of higher-order magic angles at which band flattening re-emerges², and monolayer graphene under a 1D modulation can likewise show repeated flattening at a series of potential strengths beyond the first threshold^{7;8;10}. It is therefore plausible that, when moiré coupling and a 1D modulation coexist, additional flattening conditions may also arise for θ below the first magic angle. In that regime, however, the spectrum is expected to involve stronger multi-wave mixing and becomes less amenable to a simple low-order description, so we do not pursue a detailed characterization here.

The red dashed line in Fig. 4b and the zeros in Fig. S3 show the values of u_l required to achieve a nearly flat dispersion along the direction perpendicular to $\mathbf{G}_{1\text{D}}$. In contrast to the resonant case, $L_{1\text{D}}$ is not fixed by momentum matching in the off-resonant regime and can be treated as a design parameter. Using $u_l = v_l/(\hbar v_F G_{1\text{D}}) = v_l L_{1\text{D}}/(2\pi\hbar v_F)$, one can in principle reach larger u_l by increasing $L_{1\text{D}}$, even if the experimentally attainable amplitude v_l is bounded. This comes with an important trade-off: the momentum-space extent of the 1D-induced reconstruction scales with $G_{1\text{D}}$, so choosing a longer period (smaller $G_{1\text{D}}$) reduces the range over which the bands appear flat. Overall, the flattening line (Eq. (S101)) is best regarded as a practical design guideline rather than a strict requirement.

References

- [1] J. M. B. Lopes dos Santos, N. M. R. Peres, and A. H. Castro Neto. Graphene bilayer with a twist: Electronic structure. *Phys. Rev. Lett.*, 99:256802, 2007.

- [2] Rafi Bistritzer and Allan H. MacDonald. Moiré bands in twisted double-layer graphene. *Proc. Natl Acad. Sci. USA*, 108:12233–12237, 2011.
- [3] Pilkyung Moon and Mikito Koshino. Optical absorption in twisted bilayer graphene. *Phys. Rev. B*, 87:205404, 2013.
- [4] Mikito Koshino. Interlayer interaction in general incommensurate atomic layers. *New J. Phys.*, 87:205404, 2013.
- [5] Nguyen N. T. Nam and Mikito Koshino. Lattice relaxation and energy band modulation in twisted bilayer graphene. *Phys. Rev. B*, 96:075311, 2017.
- [6] Pilkyung Moon, Mikito Koshino, and Young-Woo Son. Quasicrystalline electronic states in 30° rotated twisted bilayer graphene. *Phys. Rev. B*, 99:165430, 2019.
- [7] Cheol-Hwan Park, Li Yang, Young-Woo Son, Marvin L. Cohen, and Steven G. Louie. Anisotropic behaviours of massless dirac fermions in graphene under periodic potentials. *Nat. Phys.*, 4:213–217, 2008.
- [8] Luis Brey and Harold A. Fertig. Emerging zero modes for graphene in a periodic potential. *Phys. Rev. Lett.*, 103:046809, 2009.
- [9] Ching-Kai Chiu, Jeffrey C. Y. Teo, Andreas P. Schnyder, and Shinsei Ryu. Classification of topological quantum matter with symmetries. *Rev. Mod. Phys.*, 88:035005, 2016.
- [10] Yutao Li, Scott Dietrich, Carlos Forsythe, Takashi Taniguchi, Kenji Watanabe, Pilkyung Moon, and Cory R. Dean. Anisotropic band flattening in graphene with one-dimensional superlattices. *Nat. Nanotechnol.*, 16:525–530, 2021.
- [11] Mikito Koshino, Pilkyung Moon, and Young-Woo Son. Incommensurate double-walled carbon nanotubes as one-dimensional moiré crystals. *Phys. Rev. B*, 91:035405, 2015.
- [12] Hoi Chun Po, Liujun Zou, Ashvin Vishwanath, and T Senthil. Origin of mott insulating behavior and superconductivity in twisted bilayer graphene. *Phys. Rev. X*, 8(3):031089, 2018.
- [13] Liujun Zou, Hoi Chun Po, Ashvin Vishwanath, and T. Senthil. Band structure of twisted bilayer graphene: Emergent symmetries, commensurate approximants, and wannier obstructions. *Phys. Rev. B*, 98:085435, 2018.
- [14] Ya-Hui Zhang and T. Senthil. Bridging hubbard model physics and quantum hall physics in trilayer graphene/h-bn moiré superlattice. *Phys. Rev. B*, 99:205150, 2019.
- [15] T. Fukui, Y. Hatsugai, and H. Suzuki. Chern numbers in discretized brillouin zone: Efficient method of computing (spin) hall conductances. *J. Phys. Soc. Jpn.*, 74:1674–1677, 2005.
- [16] Manabendra Kuri, Gaurav Kumar Gupta, Yuval Ronen, Tanmoy Das, and Anindya Das. Large landau-level splitting in a tunable one-dimensional graphene superlattice probed by magnetocapacitance measurements. *Phys. Rev. B*, 98:035418, 2018.
- [17] Moeid Jamalzadeh, Zihan Zhang, Zhujun Huang, Miguel Manzo-Perez, Kim Kisslinger, Takashi Taniguchi, Kenji Watanabe, Pilkyung Moon, Gregory S. Doerk, and Davood Shahrjerdi. Synthetic band structure engineering of graphene using block copolymer-templated dielectric superlattices. *ACS Nano*, 19:9885–9895, 2025.

- [18] Carlos Forsythe, Xiaodong Zhou, Kenji Watanabe, Takashi Taniguchi, Abhay Pasupathy, Pilkyung Moon, Mikito Koshino, Philip Kim, and Cory R. Dean. Band structure engineering of 2d materials using patterned dielectric superlattices. *Nat. Nanotechnol.*, 13:566–571, 2018.
- [19] David Barcons Ruiz, Hanan Herzig Sheinflux, Rebecca Hoffmann, Iacopo Torre, Hitesh Agarwal, Roshan Krishna Kumar, Lorenzo Vistoli, Takashi Taniguchi, Kenji Watanabe, Adrian Bachtold, and Frank H. L. Koppens. Engineering high quality graphene superlattices via ion milled ultra-thin etching masks. *Nat. Commun.*, 13:6926, 2022.
- [20] Jannik C. Meyer, C. O. Girit, M. F. Crommie, and A. Zettl. Hydrocarbon lithography on graphene membranes. *Appl. Phys. Lett.*, 92:123110, 2008.
- [21] Tjerk Benschop, Tobias A. de Jong, Petr Stepanov, Xiaobo Lu, Vincent Stalman, Sense Jan van der Molen, Dmitri K. Efetov, and Milan P. Allan. Measuring local moiré lattice heterogeneity of twisted bilayer graphene. *Phys. Rev. Res.*, 3:013153, 2021.
- [22] J. Díez-Mérida, I. Das, G. Di Battista, A. Díez-Carlón, M. Lee, L. Zeng, K. Watanabe, T. Taniguchi, E. Olsson, and D. K. Efeto. High-yield fabrication of bubble-free magic-angle twisted bilayer graphene devices with high twist-angle homogeneity. *arXiv*, 2024. Preprint at arXiv:2405.11323.